Plastic UV Radiation Protection Operating by Stokes Emission

A thesis submitted for the degree of Doctor of Philosophy

by

Rui Li

Wolfson Centre for Materials Processing

Brunel University

October 2013

Abstract

A range of inorganic nanoparticles/nanophosphors that act as ultraviolet radiation absorbers were characterised and assessed in this thesis. Iron doped lithium aluminate phosphor was synthesised using a solid state reaction and also by flame spray pyrolysis. The phosphors prepared by different synthesis methods were characterised to identify their crystal structures and morphologies. Downconverting photoluminescent properties of the phosphors both as pure powders and embedded in polypropylene by co-rotating twin screw extrusion are reported.

Zinc oxide nanoparticles made by flame spray pyrolysis were also investigated. They were incorporated into polymers by means of three different approaches including co-rotating twin screw extrusion, spin coating and solvent casting. The resulted composite films were explored to understand the distribution of the zinc oxide nanoparticles. The transmittance and ultraviolet absorption of the nanocomposites were studied and are reported herein.

Another set of nanophosphors studied were zinc rich luminescent zinc oxides. They were prepared from the zinc oxide nanoparticles by firing them in a reducing atmosphere. The as-prepared nanophosphors manifested good downconverting photoluminescent properties and maintained their functions when embedded into polystyrene by solvent casting.

In this thesis a new route of synthesising aluminium doped zinc oxide nanoparticles was also established. This new approach was based on a series of unexpected results within some trials that were attempting to coat a layer of alumina on the zinc oxide nanoparticles. The concentration of the Al^{3+} in the final product could be adjusted by tailoring the amount of the Al^{3+} in the reactants during the synthesis procedures. It was also possible to coat various zinc oxide nanostructures with the aluminium doped zinc oxide.

Table of Contents

List of Figures

List of Tables

List of Abbreviations

BCZ	-	Basic zinc carbonate
EVA	-	Ethylene vinyl acetate
LED	-	Light Emitting Diode
LS	-	Layered silicate
MMT	-	Montmorillonite
PEO	-	Poly(ethylene oxide)
PET	-	Poly(ethylene phthalate)
PLA	-	Poly(lactic acid)
PMMA	-	Poly(methyl methacrylate)
PP	-	Polypropylene
PS	-	Polystyrene
SEM	-	Scanning electron microscope
TEM	-	Transmission electron microscope
UV	-	Ultraviolet
XRD	-	X-ray diffraction

List of Publications

R. Li, G. R. Fern, J. Silver, P. Bishop and B. Thiebaut, *Surprises Encounted in coating Zinc Oxide Nanoparticles with Alumina*, to be published in *'Nanoscale' (RSC publishing)*.

R. Li, G. R. Fern, R. Withnall, J. Silver, P. Bishop and B. Thiebaut, *MRS Proceedings*, 1509, (2013).

J. Silver, R. Withnall, R. Li, A. Lipman, P. J. Marsh, G. R. Fern, K. Tarverdi, P. Bishop and B. Thiebaut, *Proceddings of the International Display Workshops*, 2, (2011), 1409.

J. Silver, R. Withnall, G. R. Fern, R. Li, A. Lipman, C. Catherall, A. Salimian, P. G. Harris, K. Tarverdi, P. Bishop, B. Thiebaut, P. W. Reip and S. Subbiah, *Proceedings of the 16th International Workshop on Inorganic and Organic Electroluminescence 2012 Conference*, Hong Kong, 10-14 December (2012).

J. Silver, R. Withnall, G. R. Fern, R. Li, A. Lipman, C. Catherall, A. Salimian, P. G. Harris, K. Tarverdi, P. Bishop, B. Thiebaut , P. W. Reip and S. Subbiah, *Proceedings of the 5th International conference on Optical, Optoelectronic and Photonic Materials and Applications*, Nara, Japan, 3-7 June, p 44 (2012).

J. Silver, R. Withnall, R. Li, A. Lipman, P. J. Marsh, G. R. Fern, K. Tarverdi, P. Bishop, B. Thiebaut, R. Dixon, P. W. Reip and S. Subbiah, *Proceedings of the 3rd International Conference on luminescence and its Applications*, Hyderabad, India (2012).

R. Withnall, J. Silver, R. Stone, R. Li, A. Lipman, K. Tarverdi, B. Thiebaut, P. Bishop, S. Subbiah, D. Johnson and P. Reip, *Proceedings of the 3rd International Conference on Nanopolymers*, Düsseldorf, 13-14 September, p 1-6 (2011).

Acknowledgements

There are many people I need to give my sincere thanks to and acknowledge. Firstly, my primary supervisor Professor Jack Silver, who is the executive director of the Wolfson Centre at Brunel University, provided me with continuous help, support and guidance throughout all my PhD studies and treated me as kindly as his son. I would also like to thank my second supervisor Professor Robert Withnall (the late) for his patient guidance on experimental designs, and for explaining the use of Fluorolog spectroscopy and Raman spectroscopy.

I wish to thank many other researchers at the Wolfson Centre:- Dr. Colin Catherall, for helping me start my PhD work and advising me whenever I needed it; Dr. George Fern, for guiding me on XRPD analysis and TEM; Dr. Terry Ireland, who helped me with the Bentham spectrometers and SEM; Dr. Paul Marsh, for help with my publications and ordering chemicals; and Dr Paolo Coppo, who introduced this PhD opportunity to me.

I wish also to thank the staff at the Experimental Techniques Centre (ETC) at Brunel University including Dr. Lorna Anguilano, Mrs Nita Verma and Mr Ashley Howkins who provided huge helps for materials characterisation.

I am also in debt to the EPSRC and TSB for funding my position and the work. Through this work, the Wolfson Centre established good collaborations with our industrial partners which facilitated my work.

Finally, I would like to thank my family and girlfriend without whom I could not have focussed on my work and without whose support this thesis would not have been achieved.

Chapter 1 Introduction

1.1 Thesis introduction

The Wolfson Centre is a distinguished international research centre for materials processing under the current Director, Professor Jack Silver. The centre has a staff of around 50 including academics along with associates, fellows and PhD students. My material research commences here.

This thesis is an output of a research project entitled ‘Plastic UV Radiation Protection Operating by Stokes Emission’ (PURPOSE project) funded by EPSRC/TSB. The project was based at the Wolfson Centre and the industrial consortium was made up of many partners:-

1) Bayer, a world leading chemical and pharmaceutical company with a history of more than 150 years;
2) Intinsiq Materials, which manufactures highly functional electronic inks and Lighting & Display materials;
3) Johnson Matthey, a leading speciality chemicals company mainly producing catalysts, precious metal products and nanoparticles;
4) Innovia Films, a leading global producer of speciality high performance Biaxially Oriented Polypropylene and Cellulose films for food packaging, tobacco overwrap and labels;
5) Altro, a leading UK, family-owned manufacturer and supplier of safety flooring and wall cladding;
6) Niftylift, one of the largest manufacturer of cherry picker, boom lift, access platform, lift platform, aerial platform and work platforms;
7) Teal and Mackrill, a manufacturer of marine coatings and specialised paints.

Almost all polymers suffer degradation accompanied by deterioration of properties during their outdoor use/exposure. Ultraviolet light is the major reason for this. The location/situation of the polymeric material can vastly affect its life out of doors, and a general rule is that the closer to the equator the location the shorter the period before degradation begins.

Currently the preferred way of defending the polymers is by including conventional organic UV radiation stabilisers (such as benzophenones and hindered amine light stabilisers) in the plastics to reduce or prevent degradation by UV light. However there are two drawbacks to this approach:- 1) such stabilisers are expensive, and 2) they are sacrificial molecules that can only be used once each with the result that when the amount present in any location in the polymer is used then the degradation begins.

It is obvious that what is really needed is an included material which will protect as long as required so long as it is not degraded. To achieve this, the PURPOSE project was therefore established to develop a range of nanoparticles/nanophosphors that act as inorganic UV stabilisers and are incorporated into polymers. Such inorganic UV stabilisers have excellent UV absorption properties and are able to offer more benefits in polymer protection than the commercial organic ones. These benefits arise from their inherent properties:- they are non-volatile, non-migrating once encapsulated and non-consumable on exposure to UV light [1].

The PURPOSE project aimed to develop a new generation of novel polymer composites which could downconvert the ultraviolet radiation into daylight or infrared not only to protect the polymers from degradation (due to the ultraviolet radiation) but also to provide the polymers with the functionality of emitting light (if emission is in the visible range) or stimulating plant growth (if emission is in the infrared range).

I was fully involved in this project as one of the main researchers. The results and potential applications are reported in the following chapters.

This chapter introduces a number of topics that are relevant to the work covered in this thesis. Firstly the electromagnetic spectrum is introduced then the phenomena of luminescence and materials (phosphors) that manifest this property. Polymer ultraviolet degradation is also introduced and current ideas on its origins. In addition at the end of this chapter, the concept of polymer nanocomposites is explained as well as their development and applications.

1.2 Electromagnetic spectrum and ultraviolet radiation

The electromagnetic spectrum is presented in Figure 1.1. It is made up of an almost continuous range of radiations with all possible frequencies/energies from 30 Hz produced by certain stellar nebulae [2] to 2.9 x 10^{27} Hz detected from astrophysical sources [3]. Electromagnetic radiation was first formally described by Maxwell and subsequently confirmed by Hertz. It consists of electric and magnetic field components which are perpendicular to each other both in phase and in direction of wave propagation. The electromagnetic radiation propagates through space at the speed of light in a vacuum condition, however in the case that the radiation travels in a medium (non-vacuum condition) the speed is also determined by velocity factor and refractive index. [4]

In the electromagnetic spectrum, there is a small but (as far as humans are concerned) the most important region of optical radiation which is also called visible light with a wavelength range between 380 and 760 nm. A human eye is sensitive to this light and has its greatest sensitivity to the wavelength of 555 nm if the incident light reaches the eyeball through the cornea [5]. It is therefore of importance to study materials that can manifest these optical characteristics (in the visible region) due to both their commercial and civic significance.

Ultraviolet (UV) radiation is a region within the electromagnetic spectrum in the wavelength range from 100 to 400 nm, which corresponds to photon energies from 12.4 to 3 eV. Its wavelength is shorter than that of visible light but longer than X-rays' so it cannot be seen by human eyes. There are three sub regions of the UV depending on their wavelengths (and energies):- UVA with a wavelength ranging from 315 to 400 nm, UVB ranging from 280 to 315 nm, and UVC with the highest energy ranging from 100 to 280 nm. However, UVC and most of UVB radiations are absorbed and blocked by ordinary air and ozone in stratosphere. Only UVA and some of UVB radiations are able to reach

the earth. Even though most of UV is blocked, the rest of the radiation can still cause severe sunburn to human skin. UV radiation is also able to degrade polymers leading to considerable loss of their functionalities and the mechanism behind will be introduced later in this chapter. Figure 1.1 presents the electromagnetic spectrum and in it the region of visible light is enlarged.

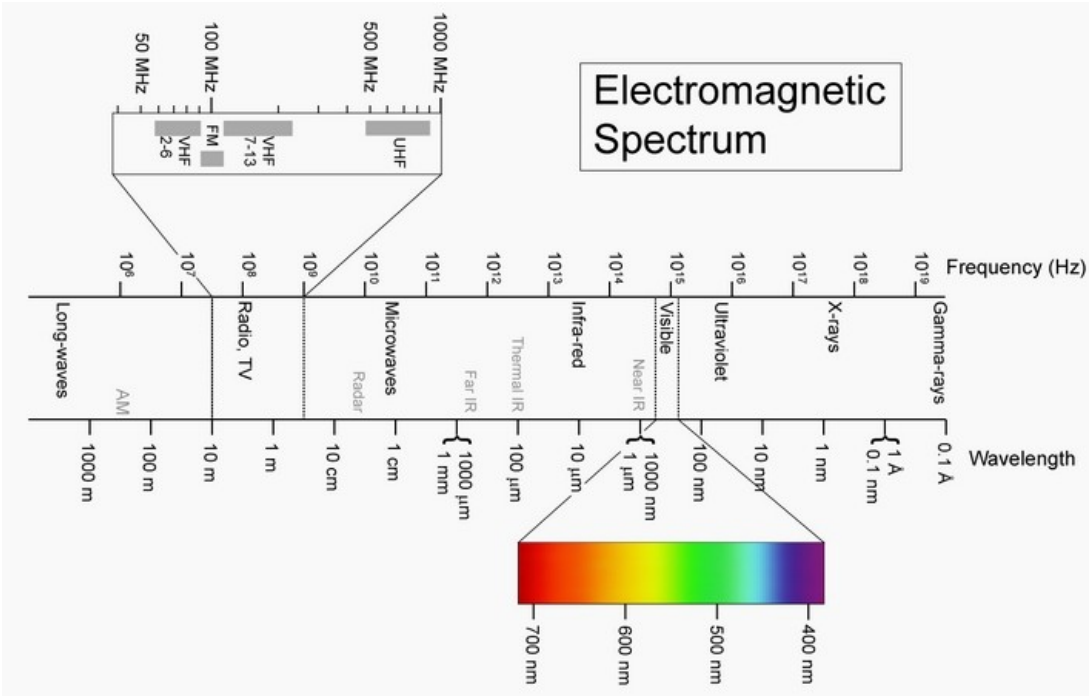

Figure 1.1 The electromagnetic spectrum **[6]**

1.3 Luminescence and phosphors

Luminescence, first introduced by Wiedemann in 1888, is the conversion of a certain type of energy into electromagnetic radiation rather than thermal radiation [7]. Luminescence can be defined as a phenomenon in which the electronic state of a substance is excited by some kind of external energy and some or all the excitation energy is given out as light. Luminescent materials, also named phosphors, are solids that have this (luminescence) ability. Those materials normally emit visible light but in some cases they can also emit infrared [8] [9] [10] [11] [12] or ultraviolet light [13] [14] [15]. Contrary to incandescence which is black body radiation and originates from thermal energy (heating), luminescence can occur by means of different excitation mechanisms shown in Table 1.1 [16].

Table 1.1 Luminescence excitation mechanisms **[16]**

Luminescence types	**Excitation sources**	**Applications**
photoluminescence	(UV) photons	fluorescent lamps, plasma displays
electroluminescence	electric field	LEDs, EL displays
cathodoluminescence	electrons	TV sets, monitors
X-ray luminescence	X-rays	X-ray amplifiers, scintillators
chemoluminescence	chemical reaction energy	analytical chemistry
bioluminescence	biochemical reaction energy	analytical chemistry
solvatoluminescence	photons	detectors, analytical devices
sonoluminescence	ultrasound	/
triboluminescence	mechanical energy	/
fractoluminescence	fracture energy	/
piezoluminescence	pressure	/
radioluminescence	ionizing radiation	/

The above (Table 1.1) illustrates that various forms of luminescence, photo- (PL), electro- (EL), cathode- (CL) and X-ray (XL) luminescence have found uses in a broad range of current industrial applications. These include cathode ray tubes (CRT) [17] [18], fluorescent tubes [19] [20], projection televisions (PTV) [21] [22] [23] [24], X-ray detectors [25] [26] [27] and scintillators [28] [29] [30] [31]. However with ongoing increasing interest and rapid research progress on phosphors, they have been significantly developed to have high energy efficiency and hence are finding uses in a series of modern applications such as plasma displays [32] [33] [34] [35] [36] [37] [38] [39], white LEDs [40] [41] [42] [43] and solar cells [44] [45] [46].

There are two other terms which are also used to describe luminescence depending on the decay time of the materials. One is fluorescence arising from the excited electron at a singlet state and having a decay time normally below 10 ns. The other one is phosphorescence and this is because the excited electron is trapped in a triplet state and forbidden to return to the lower energy state. In this case the decay time can last more than 0.1 s or even several hours. [47]

Phosphors can be either inorganic or organic. The former normally consists of various solid compounds that have particle sizes ranging from 1 to 10 μm [16]. But in some special applications [44] [48] nanosized inorganic phosphors are also of great importance due to their transparency to visible light. Although there is sacrifice of quantum efficiency when the size of inorganic phosphors decreases down to a nano scale, the problem can be significantly overcome by improved synthesis methods [49] [50]. On the other hand, molecular based phosphors have much shorter lifetimes and lower light yields compared to inorganic ones, and in addition they do not have reliable stability to radiation so currently the industrial applications of organic phosphors are still limited and are in the stage of new product development [51] [52].

In this thesis nanosized solid inorganic phosphors are the main focus as in the form of nanometre sized particles they do not scatter visible light when they are well distributed into polymers giving rise to luminescent transparent composite films.

1.4 Excitation and emission of phosphors

Inorganic phosphors usually consist of a host lattice and activators which are in fact impurity ions intentionally doped into the host lattice in a very small concentration (a few mole percentages or less). The activator ions, also known as dopants or luminescent centres, are responsible for the luminescence by direct or indirect energy absorption and subsequent energy release.

Figure 1.2 illustrates different mechanisms of the luminescent process. In the case of Figure 1.2(a), the activator can directly absorb the exciting energy which originates from any of the excitation source listed in Table 1.1, leading to an electron within the activator being promoted to a higher excited state. The excited electron undergoes a relaxation process and then returns to the lower ground state accompanied by an emission of a photon, i.e. a light emission. An $Y_2O_3:Eu^{3+}$ phosphor is a typical example of this situation. [20]

However in a more complicated case, the activator does not absorb the exciting energy by itself. Instead, there is another ion absorbing this energy and immediately transferring it to the activator (see Figure 1.2(b)). This ion is referred to as a sensitiser. An example is the lamp phosphor $Ca_5(PO_4)_3F:Sb^{3+},Mn^{2+}$. Here Mn^{2+} is the activator and does not absorb ultraviolet radiation directly. It only receives the energy from the sensitiser Sb^{3+} and emits yellow light. In addition, sometimes the excitation energy can also be absorbed by the host lattice and subsequently transferred to the activator. In this case the host lattice acts as the sensitiser and examples are $YVO_4:Eu^{3+}$ and $ZnS:Ag^{+}$. [20]

Luminescence of semiconductors is another special mechanism which is slightly different from what was explained in the above (see Figure 1.2(c)). Each semiconductor has its fixed band gap energy due to its intrinsic properties. The semiconductor can be excited by absorbing

exciting energy that is larger than the band gap. This absorption raises an electron of the semiconductor from the valance band to the conduction band and thus creates an electron-hole pair (also known as a donor and an acceptor). The recombination of these will therefore result in a radiative (light) emission.

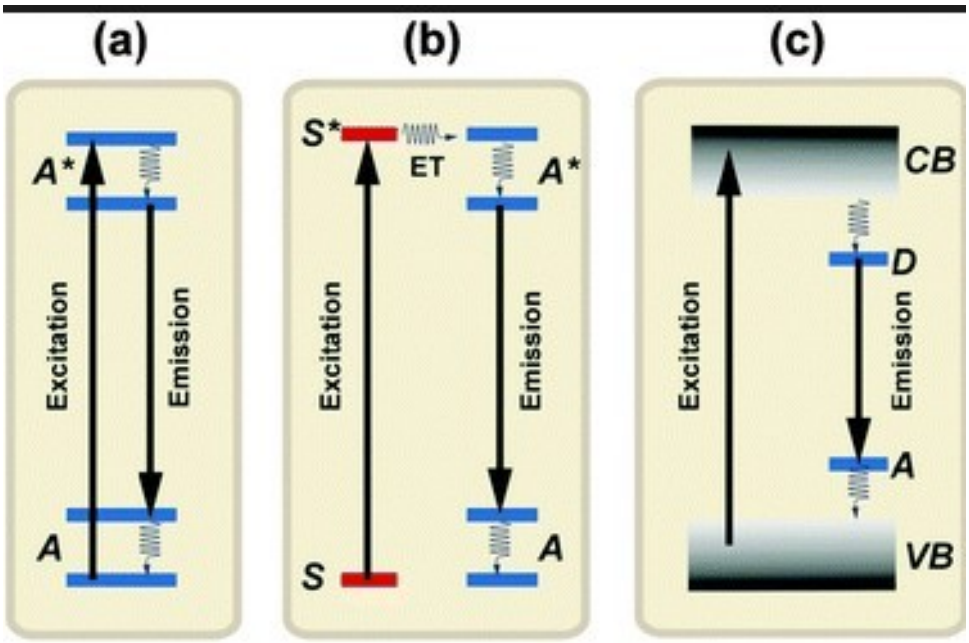

Figure 1.2 Schematic illustrations of luminescent processes in the case of (a) activator excitation, (b) sensitiser and activator excitation, and (c) semiconductors. **[53]**

.

It can be generally concluded that the luminescent process taking place in phosphors includes several stages and these are energy absorption, energy transfer and energy release (emission). Energy absorption does not have to occur at the activator ions but can take place at the sensitiser or simply within the host lattice. The absorbed energy then is able to migrate through the following methods:- 1) migration of electric charge (electrons and holes); 2) migration of excitons; 3) reabsorption of photons emitted by another activator or sensitiser; and 4) resonance between atoms with sufficient overlap integrals. These allow

the energy to be transferred to the activator and in turn to conduct the emission process. [16]

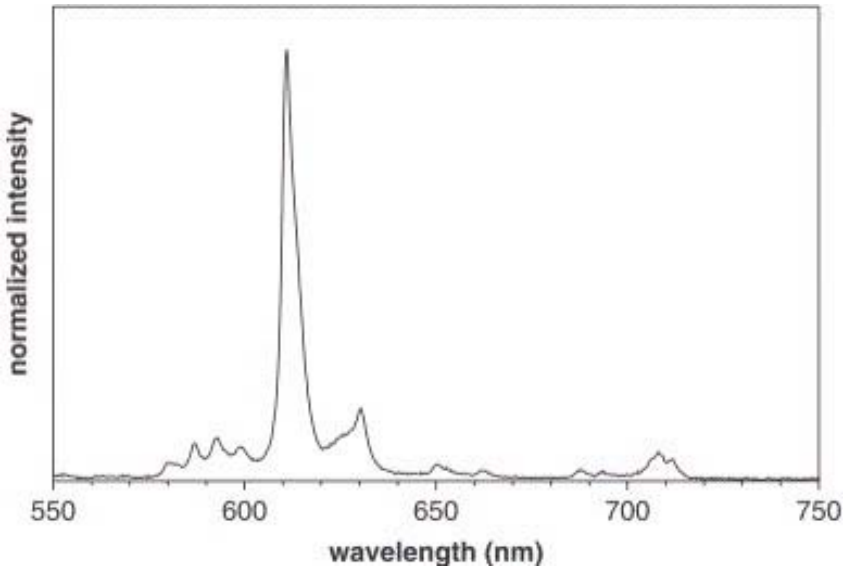

(a)

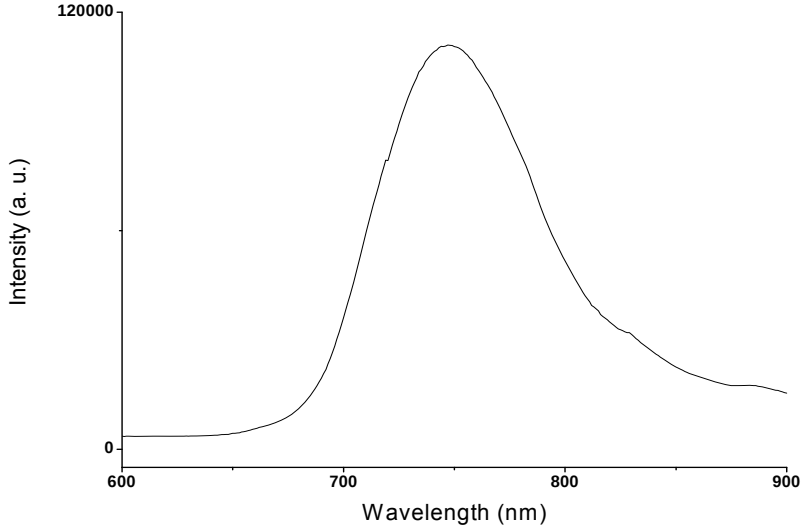

(b)

Figure 1.3 Typical emission spectrum of (a) Y_2O_3:Eu **[54]** and (b) $LiAlO_2$:Fe phosphors.

Figure 1.3 shows a typical emission spectrum of Y_2O_3:Eu (see Figure 1.3(a) [54]) and $LiAlO_2$:Fe (see Figure 1.3(b)) phosphors respectively. The spectrum is determined by the nature of the activator and host lattice. It can be seen that in Figure 1.3(a) the Y_2O_3:Eu gives a line emission. This is because the Eu^{3+} activator has a weak interaction with the host lattice and the excited electron is well shielded by the outer electrons of the Eu^{3+} cation. On the other hand in Figure 1.3(b), the $LiAlO_2$:Fe manifest a broad emission band which is due to the opposite reason, i.e. a strong interaction between the activator and host lattice. [16]

However, it is not always the case that after absorbing the energy the excited electron returns to its ground state by emitting photons. In fact the electron also can return in a nonradiative/radiationless way by emitting phonons which is a main competitor during the luminescent process and vibrates the host lattice thus the energy is released in the form of heat. The reason is due to the existence of crystal surfaces and structural defects within the host lattice. To achieve high quantum efficiency (QE) of photoluminescence, which is defined in the equation 1.1, it is therefore essential to produce phosphors that have a highly crystalline structure that has minimized lattice defects and in addition the surface of the crystals should be sufficiently clean and smooth and this may lead to the surface area to volume ratio being close to ideal. [16] [20]

$$\mathrm{QE} = \frac{number\ of\ emitted\ photons}{number\ of\ absorbed\ photons} \qquad (eq\ 1.1)$$

The reason behind the radiative and nonradiative emission can be explained by a configurational coordinate diagram presented in Figure 1.4, where the total energy (E) of the luminescent centre in its ground or excited state is plotted as a function of the distance (R) between the luminescent centre and its nearest ion. In the diagram it can be assumed that the emitting ion stays nearly at the same position during the optical process and the optical transition occurs in the vertical axis. This assumption is reasonable because an atom is much heavier (10^3 to 10^5 times) than an electron and the transition occurs electronically [55].

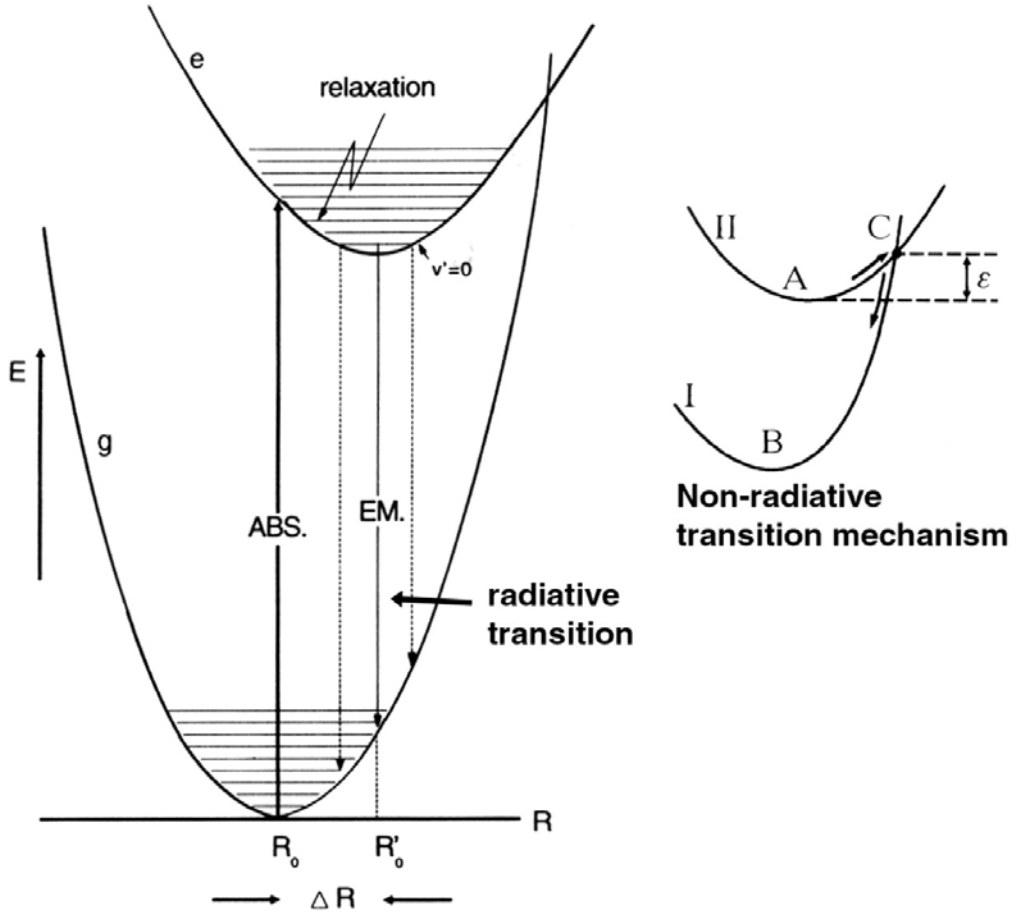

Figure 1.4 Configurational coordinate diagram. The ground state (g) has the equilibrium distance R_0 and the vibrational level v, while the excited state (e) has the equilibrium distance R_0' and the vibrational states v'. ΔR is the parabola offset. **[20]**

In the case where the radiative emission takes place, the energy absorption first leads to the ion being promoted to a high vibrational level of the excited state (see Figure 1.4). The ion is unstable and tends to adjust its new position with neighbouring ions to achieve a new equilibrium distance by releasing its excess energy to the host lattice. This is the relaxation process and afterwards the ion can be much more stable with a minimum vibrational level of the excited state. The relaxation process always occurs before the emission as the rate of lattice vibration is 10^{13} s^{-1} whereas the rate of emission is 10^{8} s^{-1}. The excited ion then

returns to its ground state by emitting photons but it still has a high vibrational level of the ground state. Again, this is followed by another relaxation which eventually completes the cycle.

However, if two parabolas (one with the excited state and the other one with the ground state) are across and there is sufficient thermal energy, the excited ion can cross the intersection (C) and return to the ground state in a nonradiative method. In this case the excitation energy is completely transferred to the host lattice as vibration and heat. This causes the nonradiative emission.

Due to the relaxation processes, the emission usually has a lower energy than the excitation during the optical transition. But there are certain phosphors that can emit higher energy and these are referred to as upconversion phosphors. In these phosphors activator atoms are able to absorb more than one photon at one time and they convert them into a photon having higher energy. A schematic diagram to illustrate the upconversion is shown in Figure 1.5. [51]

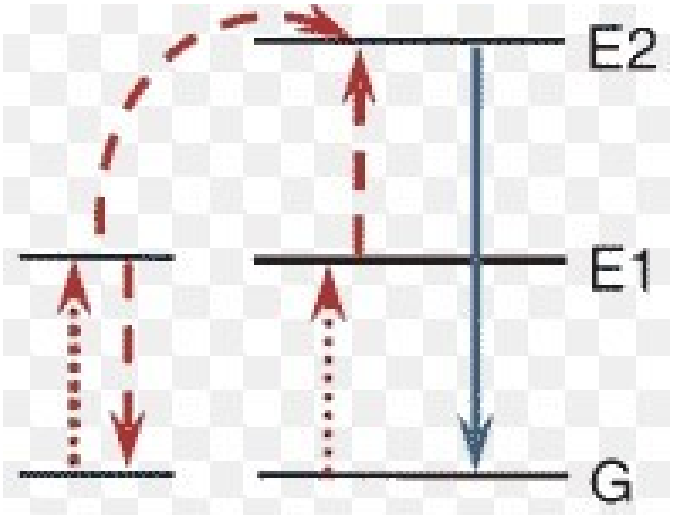

Figure 1.5 Schematic diagram of upconversion

1.5 Polymer ultraviolet degradation

Many polymers degrade irreversibly in outdoor applications due to direct exposure to the ultraviolet (UV) radiation in the solar spectrum. As a result of the UV degradation, the polymer severely suffers from a colour shift on its appearance as well as a concomitant loss of toughness and strength. Clothes drying clips (clothes pegs), for instance, gradually become faded and brittle after outdoor use for a couple of weeks/years dependent on the location on the earth, and are easily broken up when there is a force applied. Another example of the polymer UV degradation is displayed in Figure 1.6.

(a) (b)

Figure 1.6 An example of the polymer UV degradation: (a) polypropylene rope exposed to the UV radiation; (b) brand new polypropylene rope.

The rate of the UV degradation strongly depends not only on the shape, thickness, type and microstructure of the polymer, but also on a number of other factors including different environmental conditions, nature of the item, location on exposure, temperature, humidity,

surrounding oxygen concentration, atmosphere contamination and the intensity of the sunlight [56] [57] [58].

Among these factors, the oxygen concentration in the atmosphere is of great importance [59]. Normally, high oxygen permeability through the polymer matrix leads to a relatively high rate of the UV degradation [60]. Depending on the microstructure of the polymer, it has been established that an increase in the degree of crystallinity and molecular orientation can restrict the diffusion of oxygen, thus resulting in a reduction in the rate of degradation [61] [62] [63] [64]. However, it also has been argued that the UV degradation happens due to free radicals, which can further propagate and react with polymer chains causing scission and cleavage, the mechanism of which will be discussed later in more details. High polymer crystallinity [65] [66] and orientation [67] [68] [69] can also restrict the mobility of the free radicals, hence reducing their rate of termination and allowing more possibility of propagation. This effect interestingly leads to an increase in the rate of polymer UV degradation, opposite to that explained by reducing the mobility of oxygen. Even now it is difficult to predict and persuade whether the mobility restriction of oxygen or free radical is predominating [59]. They probably compete and affect each other and result in the overall rate of degradation.

Although the explanations of the rate of polymer UV degradation are still controversial, it is accepted that the degradation only happens when chromophores exist in the polymer [70] [71] [72] [73] [74]. The chromophore, which is an included molecule or segment in the polymer structure where the energy difference between its ground state and excited state is less than that of the UV light/visible(blue) light, possibly consists of external impurities (such as pigments, dyes, antioxidants and polymerisation catalyst residues), internal impurities (such as hydroperoxides and carbonyls formed during storage and processing) and special parts in the polymer chains (such as unsaturated carbon bonds, lone pair electrons and charge transfer complexes reacted with

oxygen) [56]. The sunlight therefore has adequate energy to excite the chromophore which in turn generates free radicals to cause polymer chain cleavage and degradation.

Different polymers have different abilities to absorb sunlight and thereby generate differing extents of degradation. The absorbance of the polymer is linear with the absorption coefficient of the polymer (α), the length of the light travels through the polymer (L) and the concentration of the chromophores in the polymer (C). These factors can be expressed in the light of the Beer-Lambert Law which is shown in the following equation:

$$A = \alpha LC$$

The derivation of this equation can be found in many physics books [75] [76] [77].

Photolysis and oxidative process are the two major mechanisms of the polymer UV degradation. In an inert atmosphere the photolysis reaction predominates, while in the presence of air (oxygen) the degradation is based on the combined effects of photolysis and oxidative reactions. It is called photooxidative degradation, the degradation rate of which is faster than that in the photolysis alone. [78]

It is believed that the photooxidative degradation is conducted through a free radical based auto-oxidative process, which can be explained in several stages as shown in the Figure 1.7. Theoretically, the degradation is initiated through the formation of the free radicals due to the photolysis reaction of chromophores (structural defects or impurities) in the polymer chains. Oxygen then is involved to commence the oxidative reaction with alkyl radicals, leading to a propagation step. The oxidative (peroxy) radicals can react with hydrogen atoms which are most labile in the polymer chains to allow the further propagation to proceed. It has been shown that the rate of the propagation mainly depends on the abstraction speed of the labile hydrogen atoms rather than that of the

oxygen as the latter is much faster than the former [79]. In the case of polyethylene (PE), these liable hydrogen atoms are the secondary ones. For polypropylene (PP), the tertiary hydrogen is the most liable, whereas for polystyrene (PS) the carbon-hydrogen bond in the vicinity of benzene ring is easiest to attack.

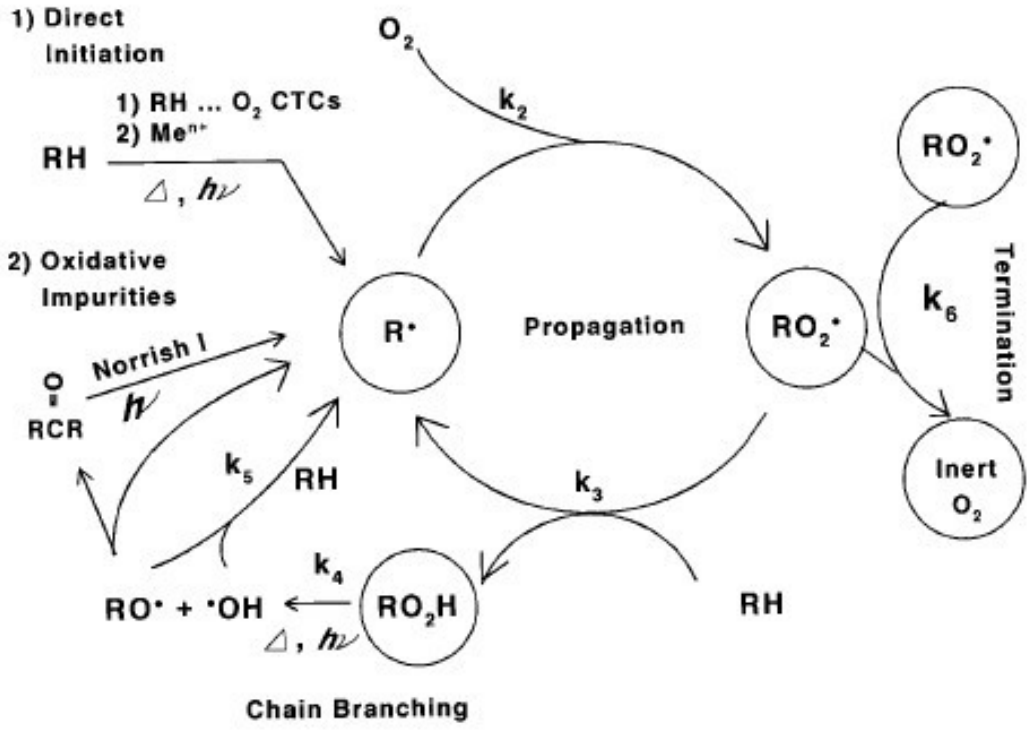

Figure 1.7 A schematic diagram of the polymer UV degradation (R = polymer chain, H = most labile hydrogen, K_i = reaction rate) **[56]**

In the next stage, the formed hydroperoxides can absorb energy (i.e. bond dissociation energy) from solar radiation and automatically decompose to alkoxy and hydroxy radicals under the homolysis process, which then can initiate another propagation cycle, causing polymer chain branching and scission [70] [80] [81]. However, not all the radicals can contribute to the propagation of the free radicals; some radicals repeat the propagation cycle, the number of which is determined by temperature and presence of oxygen [72] [73] [82] [83] [84] [85]; while some radicals,

normally peroxy radicals, form bi-molecules to cause immediate chain termination [82] [86]. For examples, the secondary peroxy radicals formed in PE can terminate in alcohols and ketones, while the tertiary peroxy radicals formed in PP and PS terminate as dialkylperoxides [87].

For most of polymers, formation of CO and CO_2 always happens during the UV degradation in an air (oxygen) atmosphere, so it is usually considered to be evidence of the polymer UV degradation. By tracking the amount of CO and CO_2, the extent of degradation can be estimated. The formation of CO and CO_2 obeys different mechanisms. Both photolysis and oxidative degradation can produce the CO and CO_2, but the oxidative mechanism (see Figure 1.8) is more significant. Additionally, the charge transfer complex between polymer and oxygen also can play an important role in the formation of the CO and CO_2, especially in the case of polyolefins (see Figure 1.9).

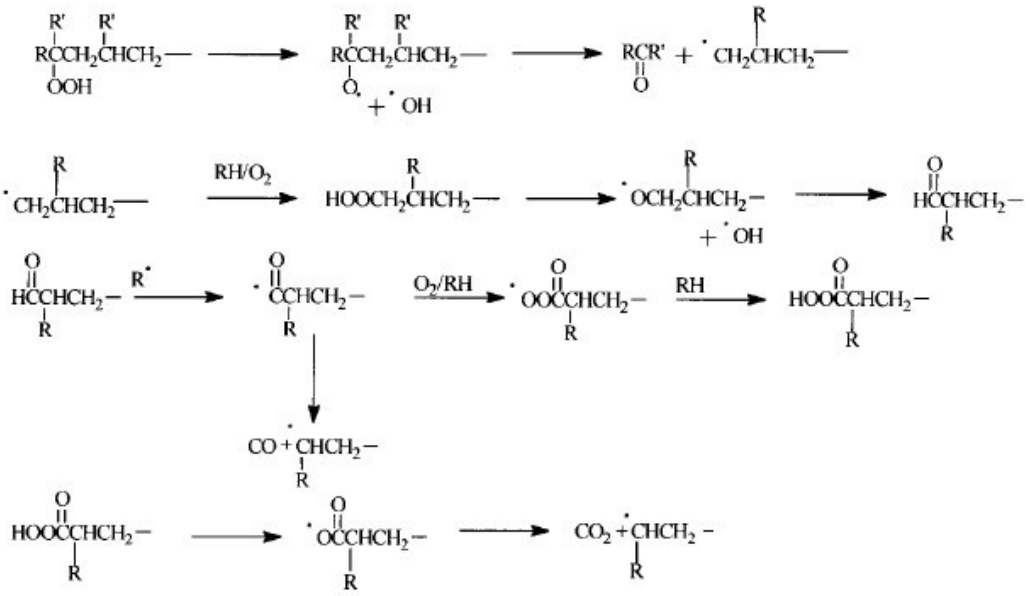

Figure 1.8 Formation of CO and CO_2 by oxidative mechanism **[56]**

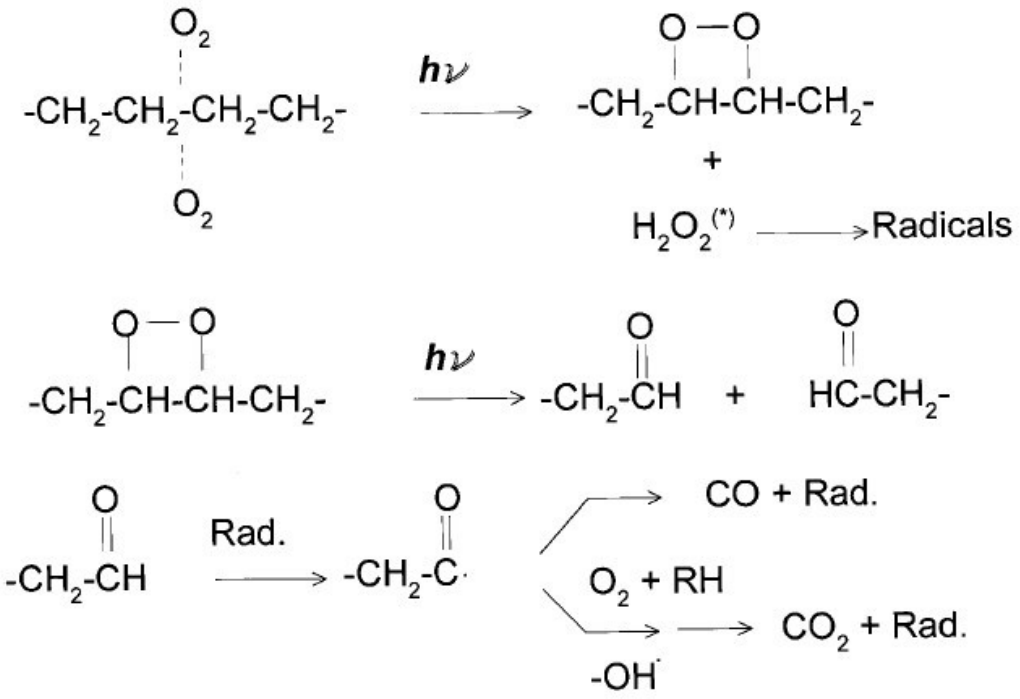

Figure 1.9 Formation of CO and CO_2 by charge transfer complex mechanism **[56]**

1.6 Polypropylene ultraviolet degradation

It can be understood that under solar radiation (outdoors), polymers (in an oxygen atmosphere) which contain chromophores will be subjected to photooxidative degradation. It is now useful to discuss the UV degradation mechanism of polypropylene because it is used as the polymer base matrix in this project.

The study of the polypropylene UV degradation has received considerable interest [57] [88] [89] due to its widespread use in outdoor applications. Polypropylene is a thermoplastic with reasonable mechanical properties (strong, tough and flexible). It also can be easily manufactured at low cost. The degradation of polypropylene automatically occurs when it is irradiated by the UV radiation. In particular the chromophores in polypropylene preferably absorb radiation in the wavelength range between 310 and 350 nm, which is almost in the UVA region of the electromagnetic spectrum [90].

According to works from A. Tidjani [57] and J. Lacoste et al [89], photooxidative degradation products of polypropylene have been identified and quantified by infrared analysis. In Tidjani's work [57], polypropylene was exposed outdoors during the summer time in Tsukuba City in Japan (140° E longitude and 36° N latitude). The intensity of the UV radiation was collected from the national meteorological station with a unit of kJ/(m^2h). A plot of photooxidation products against the UV light intensity during the outdoor photodegradation of polypropylene is presented in Figure 1.10. It can be observed that, with the increase of the intensity of the UV light, the amount of the photodegradation products increases with an induction period which is ascribed to the number of free radicals generated in the polymer during the UV degradation process. Ketones are observed to be the main oxidative products, followed by esters, acids and peresters, while tertiary hydroperoxides are the dominant photolysis products along with secondary hydroperoxides. The

amount of tertiary alcohols and γ-lactones are the lowest and can to some extent be ignored. Tidjani [57] also pointed out that there were no unsaturated products, no free and primary hydroperoxides produced in polypropylene after exposure to the UV radiation.

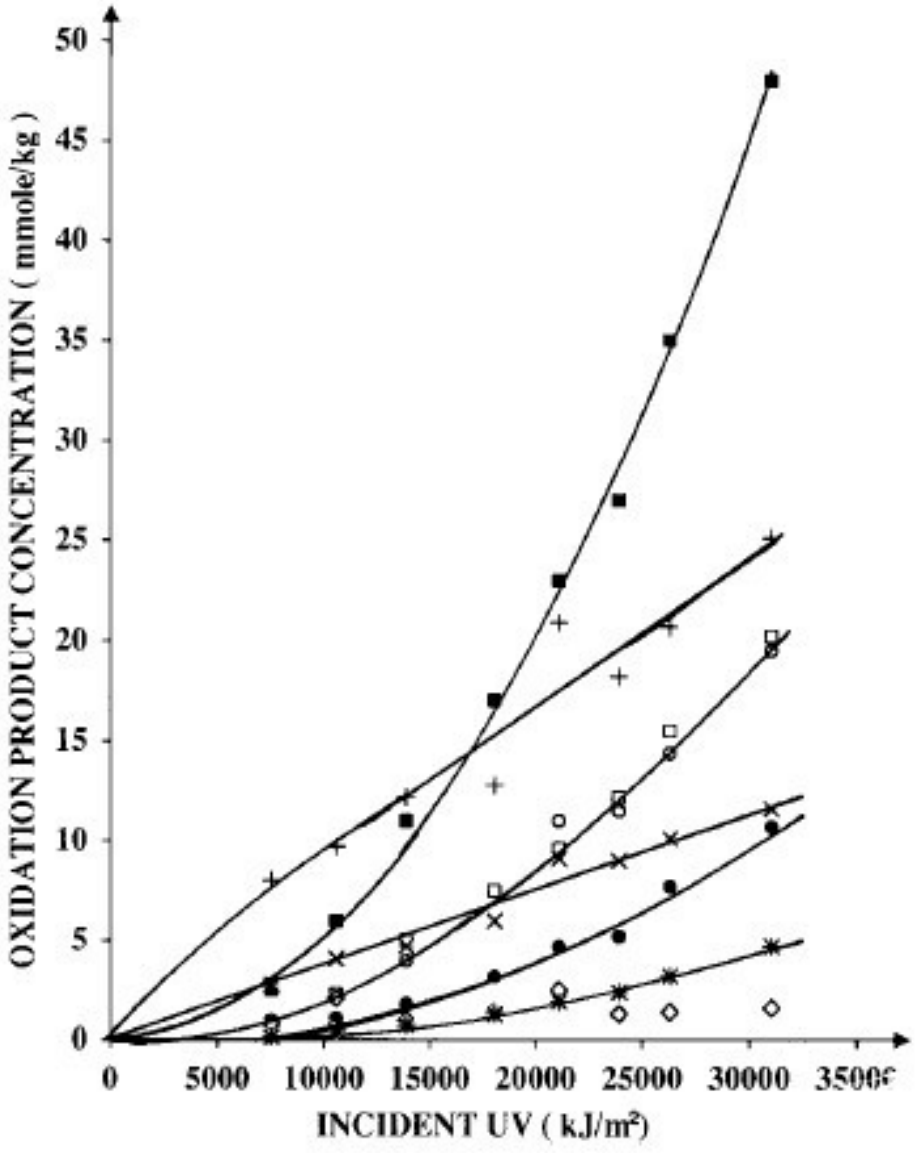

Figure 1.10 Photodegradation products of polypropylene against the intensity of the UV radiation: (■) ketone, (+) tertiary hydroperoxide, (□) ester, (○) acid, (x) secondary hydroperoxide, (●) perester, (*) γ-lactone, (◊) tertiary alcohol. **[57]**

The mechanism of polypropylene UV degradation is similar to the mechanism expressed in Figure 1.7. In the initiation stage, the carbon hydrogen bond dissociates to form secondary and tertiary alkyl radicals. After a chemical reaction with oxygen, the radicals undergo a hydrogen abstraction from the polymer matrix, resulting in secondary and tertiary hydroperoxides, amongst these the tertiary ones are predominant. Alternatively, the as-formed peroxy radicals can interact with themselves, producing alkoxy radicals or inactive terminating products [91] [92]. In theory this reaction is more likely to occur as the dissociation energy of the peroxygen bond is 154.8 kJ/mol in the peroxy radical, lower than that in the hydroperoxide (175.7 kJ/mol) [57]. The reaction of peroxygen dissociation follows the scheme displayed in Figure 1.11, and then the generated alkoxy radicals can induce propagation to form various further photodegradation products through several possible pathways shown in Figure 1.12.

Figure 1.11 A schematic diagram of the peroxygen bond dissociation in the peroxy radicals. **[57]**

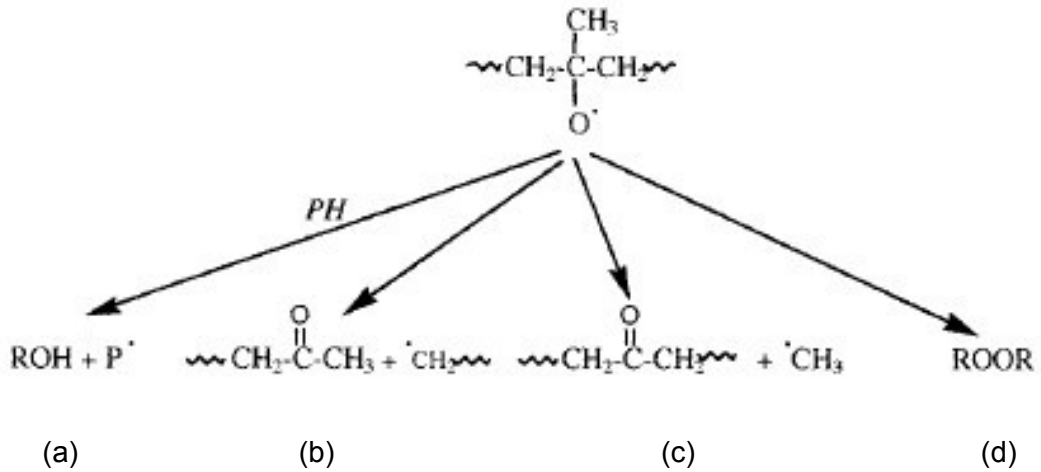

Figure 1.12 Possible pathways of the alkoxy radicals propagation: (a) tertiary alcohols; (b) methyl ketones; (c) chain ketones; (d) inactive products. **[57]**

As there are no free and primary hydroperoxides observed in the final photodegradation products of polypropylene, the ones formed as shown in Figure 12(b) and (c) will recombine in the polymer matrix and initiate another propagation cycle. The ketones then possibly react to produce acids and esters following the scheme in Figure 1.13.

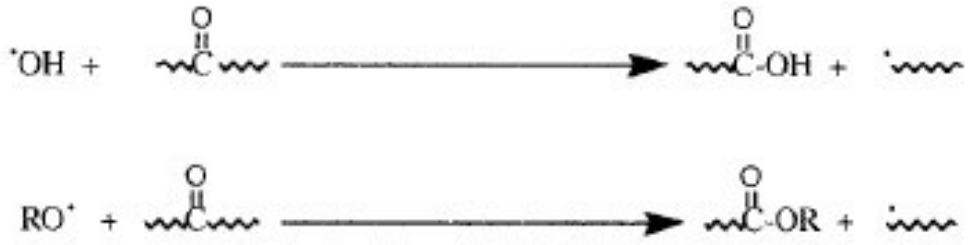

Figure 1.13 Formation of acids and esters in polypropylene matrix. **[57]**

1.7 Polystyrene ultraviolet degradation

Polystyrene is another matrix material used in this work. It is a thermoplastic which is very transparent in the visible spectral range. It is light but it is hard and rigid. In addition it has good dielectric properties. Due to these unique characteristics, polystyrene is one of the most commonly used polymers occupying 20-22% of the current plastic consumption market [93]. It is especially used in the market place for optical instruments such as optical glasses [94], optical lenses [95] and plastic scintillators [96] [97].

In common with other polymers polystyrene obviously starts to degrade if it is irradiated by the UV light due to its structural defects and encapsulated impurities which act as chromophores to absorb energy in the spectral region between 290 and 400 nm [98] [99] [100].

During the UV degradation of polystyrene, alkyl radicals shown in Figure 1.14 are initially generated. They can subsequently transform into allyl radicals (see Figure 1.15) on prolonged photolysis at room temperature. The as-formed allyl radicals are thermally stable and propagate to form a polyene structure (see Figure 1.16) which is the main photolysis product of polystyrene [101] [102].

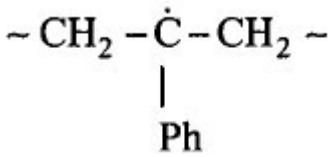

Figure 1.14 Alkyl radicals formed by photolysis in polystyrene **[103]**

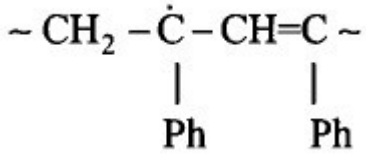

Figure 1.15 Allyl radicals formed by photolysis in polystyrene **[103]**

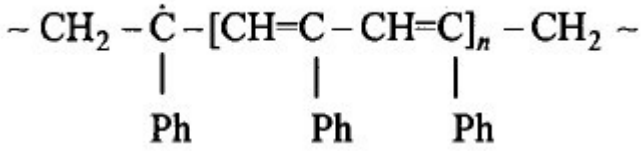

Figure 1.16 Polyene radicals formed by photolysis in polystyrene **[103]**

In the case that where an oxygen atmosphere is present, an oxidation process of the alkyl and allyl radicals occurs, leading to the formation of peroxide radicals (possible formulae for the peroxide radicals are presented in Figure 1.17) which are not thermally stable and most of which eventually dissociate and convert into the allyl radicals again, accompanied with by-products of CO_2 and H_2O [104].

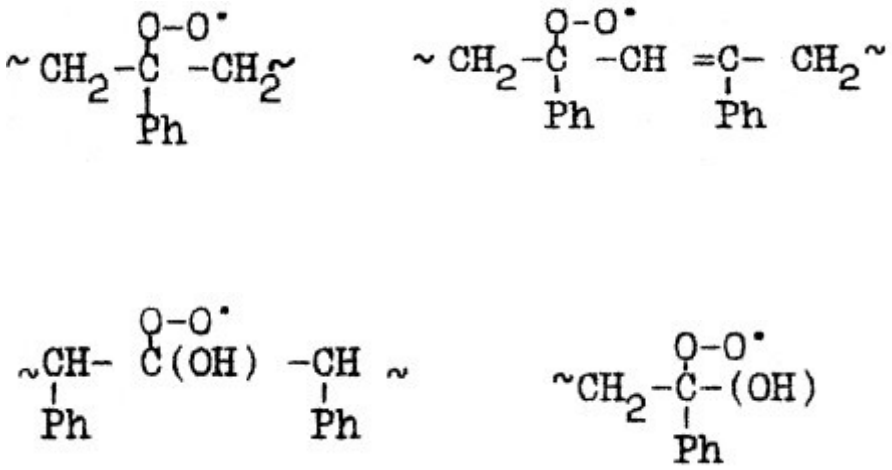

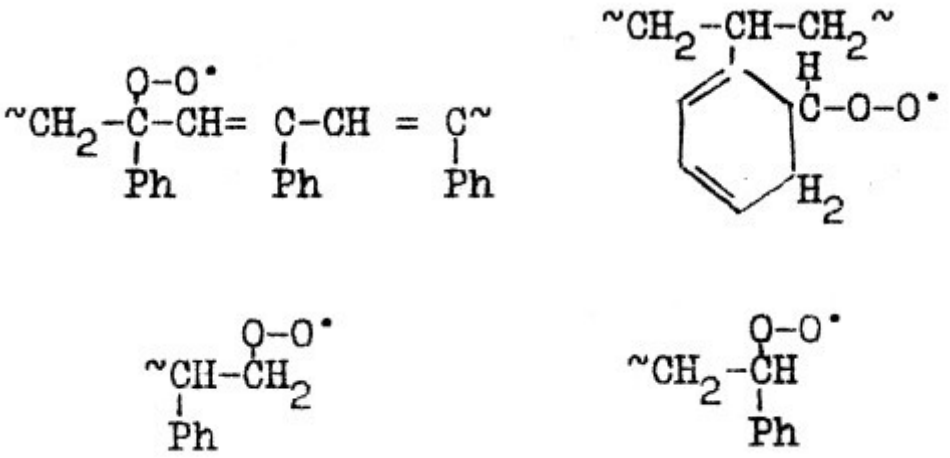

Figure 1.17 Possible formulae of peroxide radicals formed by the oxidative process in polystyrene **[104]**

The allyl radicals, as the primary photooxidation product of polystyrene UV degradation, lead to the formation of conjugated double bond fragments in a radical termination step. The conjugated polyene most likely presents in the following three structures (see Figure 1.18) where structure A absorbs energy at the wavelength of 310 nm while structure B absorbs at 330 nm and structure C preferably absorbs at 350 nm [103] [105].

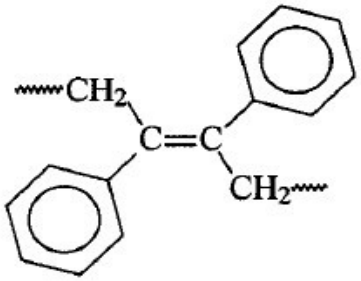

Structure A

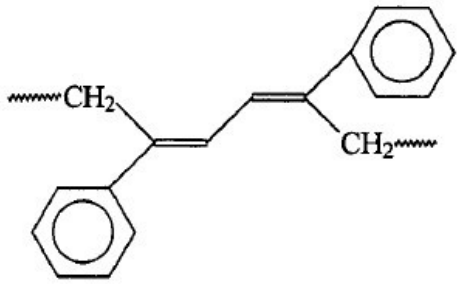

Structure B

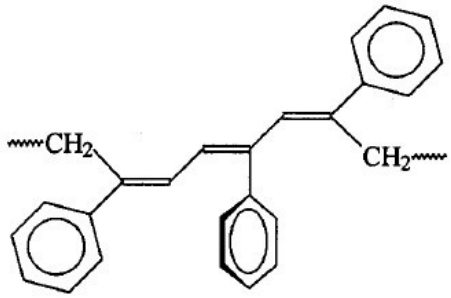

Structure C

Figure 1.18 The conjugated polyene formed by polystyrene UV degradation **[103]**

1.8 Depth profile analysis of polymer photodegradation

The mechanisms of polymer photodegradation have been discussed (see section 1.5). Two examples polypropylene and polystyrene which are used as matrix materials to make polymer nanocomposites in this work were covered in sections 1.6 and 1.7, respectively.

It has been established that the polymer photodegradation is significantly determined by the oxygen diffusion. The deeper the oxygen can diffuse into the polymer, the more the degradation products will be generated. However, according to depth profile analysis of polymer photodegradation by Nagai et al [106] [107] [108] [109] [110] [111], not all parts of the polymer are equally degraded. There is actually an extreme photo-degraded layer which is near the surface of the polymer with a depth around several microns and under this there is a degraded layer containing gradually decreased amounts of photodegradation products in the inner part of the polymer.

In fact when polymer is exposed to the UV radiation, the photo-degraded products such as carboxylic groups, hydroperoxides, carbonyl species and double bounds, will most likely accumulate near the surface of the polymer forming the extreme degradation layer. The accumulated degraded products can absorb the UV radiation more easily than the neighbouring polymer chain, thus impeding the penetration of the UV light into the inside of the polymer. Hence the photo-degraded region normally occupies the surface of the polymer and decreases exponentially in the inside. This self-barrier mechanism to some extent protects the polymer itself as the inner part cannot be irradiated by the UV radiation. [111]

The depth profile analysis including photodegradation species and the depth of the degradation layer have been studied on different polymers through a variety of methods [111] [112] [113] [114] [115] [116] [117] [118] [119] [120] [121]. By using an angle resolved attenuated total

reflection (ATR) technique, Nagai et al [111] reported that the photo-degraded products of polypropylene accumulated in a surface layer with a depth of 0.8 μm after 96 hours UV exposure. A plot of the fraction volume of the degradation products against depth is shown in Figure 1.19. The fraction volume is constant up to 0.8 μm and decreases exponentially afterwards.

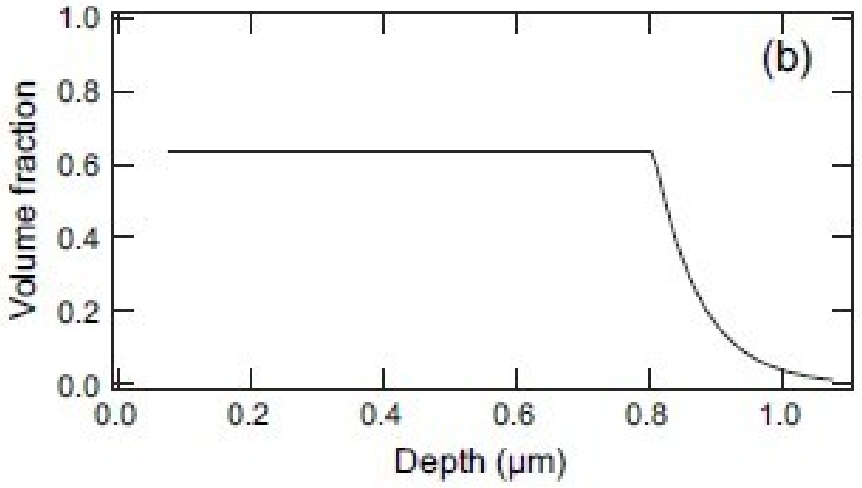

Figure 1.19 Depth profile analysis of polypropylene UV degradation (96 hours exposure time) **[111]**

It was also reported [111] that after exposure to the UV light for the same time as polypropylene (96 hours), polystyrene turned out to have a thinner extreme photo-degraded layer of 0.6 μm in depth, and the plot of the fraction volume against depth is presented in Figure 1.20. This shows a different behaviour compared to polypropylene. In this case the fraction volume keeps constant to 0.6 μm depth and then decreases gradually, which means the degradation region expands to the inner area of the polystyrene.

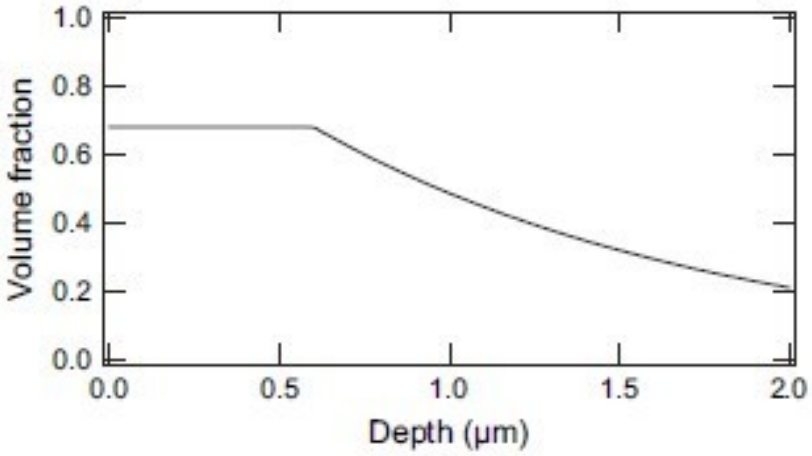

Figure 1.20 Depth profile analysis of polystyrene UV degradation (96 hours exposure time) **[111]**

1.9 Polymer nanocomposites

Nanocomposites are materials that have multi-phases and one of the phases is nanosized [122]. Due to the significant development of nanomaterials, nanocomposites become widely used with an anticipation of their outstanding properties deriving from the combination of each phase.

There are several types of nanocomposites in terms of their matrix materials and these include ceramic matrix nanocomposites (CMNC), metal matrix nanocomposites (MMNC), and polymer matrix nanocomposites (PMNC) [123]. In this thesis, the polymer matrix nanocomposites incorporating inorganic nanoparticles are the main focus of study.

PMNCs have the most widespread uses in the current market compared to CMNCs and MMNCs. This is because they can benefit from both organic and inorganic materials and simultaneously combine their properties. In general polymer nanocomposites are easy to manufacture and process. They have low cost and consume low energy during the fabrication. By incorporating nanofillers, polymer nanocomposites can display good mechanical properties such as high modulus, high strength, good toughness and be lightweight. In addition the nanofillers can also provide other characteristics including thermal stability, magnetic properties, optical properties, flame retardation, electrical conductivity, chemical resistance and UV resistance [124] [125] [126]. In this work the most important properties are the optical properties and the UV resistance.

The effect of nanofillers on properties of polymer nanocomposites is determined by the shape, volume fraction, distribution and orientation of the nanofiller [127] [128]. As the nanofillers preferentially tend to form clusters or agglomerates, it is always an issue to evenly distribute the nanosized additives into the polymer matrix [129]. To achieve this, one

method is to improve the processing techniques and this will be further discussed in chapter 5. Alternatively there is another possible method which is to apply a modification on the surface of the nanofiller by coating it with a thin layer of polymer thus the compatibility between the nanofiller and host matrix is improved [123] [130]. Moreover as outlined in section 1.8 as it is the surface of the polymeric material that is first to undergo degradation, it therefore makes sense to protect the surface, because if the surface is protected then so will the bulk be protected. This is one of the approaches that are taken in this thesis.

Many works have been published on the preparation of polymer matrix nanocomposites [131] [132]. The major preparation methods can be summarised as:- 1) melt intercalation [133] [134] [135] [136] [137]; 2) intercalation of polymer or prepolymer from solution [138] [139] [140] [141] [142]; 3) in-situ intercalative polymerization [143] [144] [145]; and 4) template synthesis [146] [147].

Therefore based on the unique properties of the nanofillers and the various methods of incorporating them into polymers, the uses of polymer matrix nanocomposites has expanded and they are now found in a wide variety of industrial applications (see list in Table 1.2) [123] [126] [148].

Table 1.2 Potential applications of polymer matrix nanocomposites **[123] [126] [148]**

Nanocomposites	**Applications**
Epoxy/MMT	Materials for electronics
EVA/clay	Wires and cables – Kabelwerk Eupen of Belgium
Nylon-6/clay	Barrier films – Bayer AG
Nylon-6/clay	Films and bottles – Honeywell
Nylon-6,12,66/clay	Auto fuel systems – Ube
Nylon-6/PP/clay	Electrically conductive
Nylon-6/LS	Automotive timing belt – TOYOYA
PEO/LS	Airplane interiors, fuel tanks, brakes and tires
PET/clay	Food packaging application
PLA/LS	Lithium battery development
Polycarbonate/SiO_2	Abrasion resistant coating
Polycarprolactone/SiO_2	Bone-bioerodible for skeletal tissue repair
Polyethylacrylate/SiO_2	Catalysis support
Polyimide/SiO_2	Microelectronics
Polyimide/clay	Automotive step assists – GM Safari and Astra Vans
Polypropylene/clay	Packaging – Clariant
Poly(amide-imide)/TiO_2	Composite membranes for gas separation
PMMA/SiO_2	Dental application, optical devices
Thermoplastic olefin/clay	Beverage containers
Unsaturated polyester/clay	Marine, transportation – Polymeric Supply

1.10 Objective and layout of the thesis

The objective of this thesis is explaining the details of the work carried out in my research. There were two focuses:- one was developing a range of nanoparticles/nanophosphors that have down converting luminescent properties, i.e. they are able to transfer the UV radiation to visible light or infrared; the other one was aiming to achieve an even distribution of the nanoparticles/nanophosphors in various polymer matrices.

This chapter has introduced the general background behind the work that appears in the following chapters. The next two chapters introduce the experimental work and techniques used to prepare and characterise the nanocomposites produced in this work and the following report and discuss the results. Finally in the last chapter ideas for future work are presented.

Chapter 2 Experimental

2.1 Introduction

This chapter reports the synthesis of the inorganic nanoparticles/nanophosphors used in this work. The methods of incorporating these nano-fillers into/onto polymers are also explored and their details are given here.

From Section 2.2 to section 2.8, experiments regarding the inorganic chemistry are discussed. Synthesis of nanoparticles such as iron doped lithium aluminate ($LiAlO_2$:Fe), zinc oxide (ZnO), zinc rich luminescent zinc oxide (ZnO:Zn) and coated ZnO were investigated either on a laboratory scale through calcining or on an industrial scale using flame spray pyrolysis. Their synthesis and processing parameters were varied to optimise the excitation and emission characteristics of the as-prepared final products. Synthesis of aluminium oxide (Al_2O_3) coating on ZnO nanoparticles and preparation of aluminium doped zinc oxide ($ZnO:Al^{3+}$) nanoparticles were also studied by means of a wet chemical method.

Following the work on the inorganic materials, the later part of this chapter (section 2.9 to 2.12) discusses their incorporation into organic materials. Three different techniques including co-rotating twin screw extrusion, spin coating and solvent casting were used and compared to make polymer nanocomposite films by using polypropylene or polystyrene as a matrix polymer material.

2.2 Synthesis of iron doped lithium aluminate phosphors

An iron doped lithium aluminate ($LiAlO_2$:Fe) phosphor was synthesised via a solid state reaction method [149], which conventionally is a simple technique with low costs used to produce phosphors. Raw chemicals for this method were all purchased from Sigma-Aldrich at laboratory reagent grade with purity of 99.9%.

Stoichiometric amounts of lithium carbonate (Li_2CO_3), aluminium oxide (Al_2O_3) and ferrous-ferric oxide (Fe_3O_4) were finely mixed and ground in a mortar and pestle. The doping concentration of iron was 1mol%. The mixture was initially fired at 500 °C for 1 hour. After being re-ground, the mixture was allowed to be further fired for 3 hours at an elevated temperature of 1050 °C. Then, the mixture was again ground and re-fired for another 3 hours at 1050 °C to achieve a better growth of the lithium aluminate lattice and a more sufficient diffusion of iron. The final product was the $LiAlO_2$:Fe as white powders.

There are some drawbacks in using this synthesis method. One is the relatively long firing time required to achieve good crystal structure and high luminescence. On the other hand, due to the mechanical grind which was applied before each firing process, surface damages (e.g. surface defects) were simultaneously induced that could cause a reduction of luminescence. This latter reduction was offset by the firing to some extent as this caused a smoother surface.

2.3 Synthesis by flame spray pyrolysis

When synthesising inorganic metal oxide particles whose sizes go down to a nanometre level, a special combustion technique that is able to manufacture them in an industry scale with a high purity and a uniform size distribution was employed. This technique is flame spray pyrolysis.

The flame spray pyrolysis was first developed by Pratsinis and his research group [150] [151]. Since then it has received considerably increasing interest [152] [153] [154] [155] [156] [157] [158] in both the academic and industrial fields due to the possibility of high production rate. The technique has developed rapidly and now it has matured to synthesise up to 200 g h^{-1} of either single metal oxide nanoparticles or complex mixed oxide nanoparticles. Johnson Matthey (JM), one of our research partners has this equipment and has provided the iron doped lithium aluminate ($LiAlO_2$:Fe) and the zinc oxide (ZnO) nanoparticles used in this work.

Figure 2.1 shows a schematic of the flame spray pyrolysis set-up. A series of liquid precursors containing target metals (lithium, aluminium and iron for $LiAlO_2$:Fe or zinc for ZnO) were dissolved in a solvent system (normally using alcohol such as methanol or ethanol) and sprayed as droplets at a controlled rate through a nozzle into a flame in an oxygen inlet. The size of the droplets was determined by the liquid and oxygen flow rate in order to avoid excessively large droplets which could stay a long time in the flame resulting in a non-uniform particle size. The droplets were then evaporated and the precursors underwent combustion in the flame, followed by particle nucleation, growth, possible collision and agglomeration as illustrated in Figure 2.2 [158]. In the beginning steps, the solvent must have good volatility, otherwise hollow particles will be formed in an eggshell like structure where the only surface of the droplets is solidified and in the inside remains residual solvent which easily causes particle explosion [159] [160] [161]. After the nucleation step, the particles

can undergo possible coalescence and sintering to form the final nanosized products.

Pure and uniform nanoparticles of the $LiAlO_2$:Fe and the ZnO were synthesised by Johnson Matthey by this method and sent to Brunel University for further characterisation and incorporation into polymers.

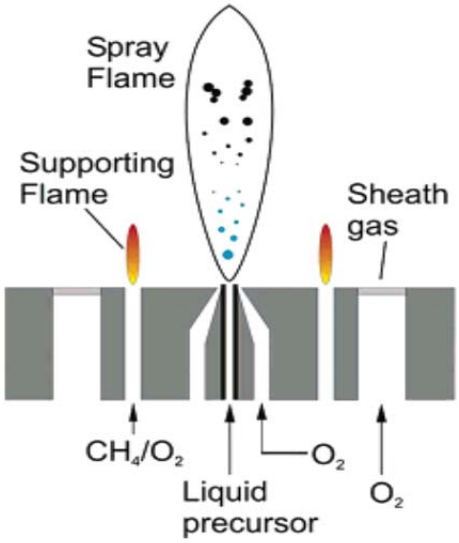

Figure 2.1 Schematic of the flame spray pyrolysis set-up showing the liquid precursor and fuel feeds.

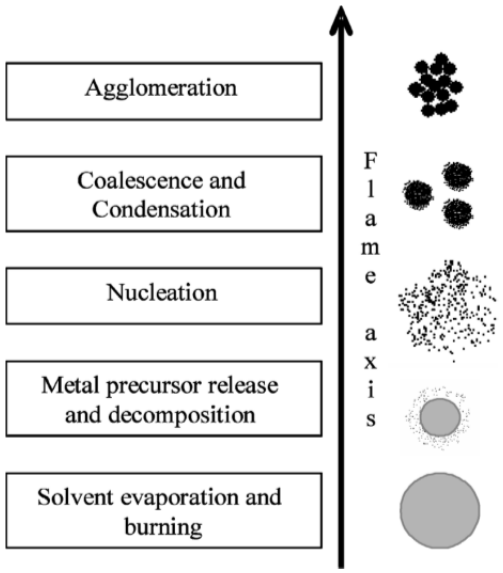

Figure 2.2 Schematic of the nanoparticle formation in the flame **[158]**

2.4 Synthesis of zinc-rich luminescent zinc oxide nanophosphors

The ZnO nanoparticles made from the flame spray pyrolysis were the starting materials to synthesise zinc-rich luminescent zinc oxide (ZnO:Zn) nanophosphors. The ZnO was calcined in an alumina crucible in a reducing atmosphere of carbon monoxide (CO) to be transformed to the ZnO:Zn.

As the synthesis commenced with the nano-sized particles, it was found that they were sensitive to various firing conditions. Subtle variations in the parameters of firing process could lead to drastic variations in the luminescence of the final products. Therefore, for optimization of the luminescence of the ZnO:Zn nanophosphors, the process was tried with different firing time including 15, 30, 45 and 60 minutes as well as two different firing temperatures (700 °C and 800 °C). The greatest luminescence was found for the samples heated for 45 minutes at 800 °C.

This nanophosphor was fully characterised (see section 6.2) and was further incorporated into a polystyrene matrix to make a luminescent composite (see section 6.3).

Another reducing atmosphere, H_2/N_2 (1:100), was also used to produce a batch of ZnO:Zn. However the nanophosphors prepared by this method showed poor luminescence compared with that prepared by using the carbon monoxide atmosphere, so there was no further investigation on this batch.

2.5 Aluminium oxide coating on zinc oxide nanoparticles

A series of ZnO derivatives in Chapter 7 was synthesised via a similar chemical process. Their preparation methods are reported from this section to section 2.8. All the samples were further characterised and they are discussed in Chapter 7. Table 2.1 (in section 2.8) summarises the preparations of those samples and reactants used in the chemical process.

A batch of the ZnO nanoparticles (120 g) with a reference number of AC1268etc was synthesised by Johnson Matthey using the flame spray pyrolysis as described in section 2.3. This batch is referred to as sample 1 in Chapter 7.

The aluminium oxide (Al_2O_3) coating method was based on that previously reported [162] except that we used the method to coat our already formed ZnO nanoparticles directly rather than to prepare the ZnO particles at the same time from a zinc sulphate solution. Hence we affectively joined the previous experiment at the point where they re-disperse their precipitate of basic zinc carbonate (BCZ) [162].

Preparation 1:- 2.71 g ZnO nanoparticles were dispersed in 100 ml deionised water. 10 ml NH_4HCO_3 solution (1.25 M) was then added to the ZnO slurry (the pH of the solution at this point was around 7.8). After ultrasonication for 15 minutes, 50 ml $Al_2(SO_4)_3$ solution (0.03 M) (the pH of this solution was between 2.9 to 3.1) was slowly dropped onto the surface of the slurry which, in the meantime, was continuously stirred at a constant speed. Another 30 minutes stirring was required after the addition of the $Al_2(SO_4)_3$ solution (the pH of this final solution containing the precipitates was always between 7.3 to 8.3). The slurry was filtered to obtain precipitates, which were then washed and dried at 80 °C overnight. The final product was obtained by calcining the precipitates at 600 °C for 1 hour.

In the above method the ratio of Al_2O_3 to ZnO was 5wt% (equivalent to 7.9mol% Al^{3+}). Where this is in the dilute solution the samples are referred to as 2A (before firing) and 2B (after firing).

Preparation 2:- In other runs this ratio was kept the same but the dilutions were halved so the concentrations were enhanced (i.e. 2.5 M NH_4HCO_3 solution and 0.1 M $Al_2(SO_4)_3$ solution). Where this is in the concentrated solution the samples are referred to as 3A (before firing) and 3B (after firing).

Sample 1 was also annealed for 1 hour in air at 600 °C without going through the chemical procedures as above. Much larger nanoparticles grew (sample 1L).

2.6 Aluminium oxide coating on zinc-rich luminescent zinc oxide nanophosphors

Another batch of JM sample of ZnO nanoparticles (100 g) with a reference number of AD3177 prepared from the flame spray pyrolysis is referred to as sample 4 in Chapter 7.

To form larger particles of ZnO:Zn, sample 4 was heat treated using the method described in section 2.4. It was fired at 800 °C for 45 minutes in a reducing atmosphere (made by placing the crucible containing the nanoparticles in a larger crucible containing carbon) to transform the ZnO to the ZnO:Zn. This caused carbon monoxide to be formed from all the oxygen present as well as that released by the ZnO. These larger nanoparticles will be referred to as sample 5. The resulting carbon monoxide kept the atmosphere reducing by occupying the space around the crucibles.

The nanocrystals from sample 5 of the ZnO:Zn were then treated as in preparation 1 (dilute condition) in section 2.5. The ZnO:Zn (2.71 g) nanophosphors were used to start the coating procedures instead of using the ZnO nanoparticles. The precipitated material is referred to as sample 6A. Sample 6A was calcined at 600 °C for 1 hour to form sample 6B.

2.7 Zinc oxide coating on zinc-rich luminescent zinc oxide nanophosphors

A further batch of large ZnO:Zn nanocrystals was prepared from JM sample 1 using the same preparation of sample 5 (see section 2.6) and is referred to as sample 7. Sample 7 was then treated as follows to achieve a zinc oxide coating.

Preparation 3:- 2.71 g of ZnO:Zn nanophosphors (sample 7) were dispersed in 100 ml deionised water. 10 ml NH_4HCO_3 solution (1.25 M) was then added to the ZnO:Zn slurry. After ultrasonication for 75 minutes, the solution was stirred for another 35 minutes and allowed to stand. The slurry was filtered to obtain precipitates, which were then washed and dried at 80 °C overnight. This sample is referred to as sample 8A. The final product was obtained by calcining the precipitates at 600 °C for 1 hour and termed sample 8B.

2.8 Synthesis of aluminium doped zinc oxide

The JM ZnO nanoparticles of sample 4 were the starting material to make zinc oxide doped with aluminium ($ZnO:Al^{3+}$). The preparation was similar to the preparation 2 in section 2.5, but here Al:Zn ratio of 10wt% was used and the procedures were as follows.

Preparation 4:- 2.71 g ZnO nanoparticles (sample 4) were dispersed in 100 ml deionised water to which 10 ml NH_4HCO_3 solution (2.5 M) was then added. The mixture was ultrasonicated for 15 minutes, during which it was constantly (magnetic) stirred. 30 ml $Al_2(SO_4)_3$ solution (0.1 M) was slowly dropped onto the surface of the slurry . Another 30 minutes stirring was required after the addition of the $Al_2(SO_4)_3$ solution. The slurry was filtered to obtain precipitates, which were then washed and dried at 80 °C overnight. The final product was obtained by calcining the precipitates at 600 °C for 1 hour.

In this case the samples are referred to as 9A (before firing) and 9B (after firing).

Table 2.1 Summary of preparation methods of samples discussed in Chapter 7

Sample number	Sample description	Chemicals	
		NH_4HCO_3	$Al_2(SO_4)_3$
Sample 1	JM ZnO nanoparticles AC1268etc	N/A	N/A
Sample 1L	Nanoparticles prepared by firing sample 1	N/A	N/A
Sample 2A	Precipitates from chemical preparation 1	10 ml, 1.25 M	50 ml, 0.03 M
Sample 2B	Nanoparticles prepared by firing sample 2A	N/A	N/A
Sample 3A	Precipitates from chemical preparation 2	10 ml, 2.5 M	15 ml, 0.1 M
Sample 3B	Nanoparticles prepared by firing sample 3A	N/A	N/A
Sample 4	JM ZnO nanoparticles AD3177		
Sample 5	ZnO:Zn nanoparticles prepared by reducing sample 4	N/A	N/A
Sample 6A	Precipitates from chemical preparation similar to preparation 1	10 ml, 1.25M	50 ml, 0.03 M
Sample 6B	Nanoparticles prepared by firing sample 6A	N/A	N/A
Sample 7	ZnO:Zn nanoparticles prepared by reducing sample 1	N/A	N/A
Sample 8A	Precipitates from chemical preparation 3	10 ml, 1.25 M	N/A
Sample 8B	Nanoparticles prepared by firing sample 8A	N/A	N/A
Sample 9A	Precipitates from chemical preparation 4	10 ml, 2.5 M	30 ml, 0.1 M
Sample 9B	Nanoparticles prepared by firing sample 9A	N/A	N/A

2.9 Incorporation of iron doped lithium aluminate nanoparticles into polypropylene

170 g of the $LiAlO_2$:Fe nanophosphors (reference number: AC9225) were produced by Johnson Matthey and used as sent. Polypropylene (PP) pellets were provided by another project partner, Innovia.

The incorporation of the $LiAlO_2$:Fe nanophosphors into PP was conducted by using a HAAKE Rheomex OS PTW 24 co-rotating twin screw extruder (see Figure 2.3). The nanophosphors and pellets were dried and physically mixed prior to being gravitationally fed into the screw from a hopper which is top mounted on the extruder. The polymer was then heated until fully molten by a heating barrel which is the main part of the extruder. In addition the rotating screw which forces and pushes the polymer forward through a die can also provide shear heating to the polymer. After being fully mixed by the screw, the molten polymer was forced to pass through the die to form the desired shape. The extrudate was cooled by a water tank.

The polymer extrusion was conducted under a processing temperature of 200 °C and a screw speed of 150 min^{-1} [163] [164]. These processing conditions allowed the nanoparticles to become well dispersed in the polymer matrix. This was verified in an SEM image (see Figure 4.15). The $LiAlO_2$:Fe nanophosphors were mixed with the PP pellets at the concentration of 2wt% and extruded to obtain polypropylene composite sheets.

(a)

(b)

Figure 2.3 The HAAKE Rheomex OS PTW 24 co-rotating twin screw extruder: (a) front view; (b) back view.

2.10 Incorporation of zinc oxide nanoparticles into polypropylene

300 g of the zinc oxide nanoparticles with reference number of AC7747 were also provided by Johnson Matthey again synthesised via the flame spray pyrolysis technique. The nanoparticles were embedded in polypropylene at three weights (2%, 5% and 10%) again through the co-rotating twin screw extrusion method (see Figure 2.3).

In the case of the low loading percentage (2%), the extrusion parameters were similar to that of the PP – 2% $LiAlO_2$:Fe nanocomposite (i.e. 200 °C and 150 min^{-1}). However, with the increasing loading amount, the extrusion temperature was set to 210 °C for either 5% or 10%, whereas the screw speed was adjusted to 180 min^{-1} for 5% and 220 min^{-1} for 10%. High sheer stress is significantly required to achieve a better distribution of the nanoparticles if there is a vast amount of nano-fillers, such as 10wt%, dispersed in the polymer matrix. [165] [166]

2.11 Incorporation of zinc oxide nanoparticles into polystyrene

Polystyrene (PS) raw pellets were provided by a project partner, Bayer. To investigate the effect of the way of composite processing on the distribution of nanoparticles, two new methods were employed to incorporate the ZnO nanoparticles into the PS matrix. One was a spin coating technique, which is an effective method to produce thin or ultra-thin films. The other one was a solvent casting technique providing relatively large and thick films. Many works have been reported to receive huge benefits from using these techniques [167] [168] [169] [170] [171] [172].

The procedures of the spin coating normally include depositing a small amount of coating material on the centre of a flat substrate, which is then rotated at a high speed. So the coating material is spread to/off the substrate by the applied centrifugal force. During the rotation, the solvent simultaneously evaporates in order to form a thin film as the final product which is solidified on the substrate. The thickness of the film is dependent on both the parameters of the spin process and the nature of the coating material, such as rotation speed, rotation time and substrate to be coated as well as viscosity and concentration of the solution. In general, the spin coating is adopted to provide thin films in nanoscale. [173] [174]

In the case of producing films with a higher thickness (larger than microns and even millimetres), the solvent casting is highly preferable. This technique is one of the oldest technologies in manufacturing polymer films. It has been developed more than hundred years due to high demand of photographic industry. [175] During the solvent casting process, the polymer is fully dissolved in a volatile solvent or water. The nanofillers are then added and thoroughly mixed with the dissolved polymer in the solution in order to achieve a stable mixture with certain viscosity. The mixture is cast on a substrate to allow the solvent to

evaporate. The homogeneous films are eventually formed and they should be easily released from the substrate. Nowadays the solvent casting is still highly competitive to the extrusion technique if extremely high quality of the film is required. This is because the solvent casting can provide the film with uniform dispersion of nanofillers, highly optical purity of the film and low haze. It also can produce the film with uniform thickness distribution, excellent flatness and dimensional stability. [175]

In this section, the methods of making PS – ZnO nanocomposite films are described in detail. The films were achieved by using the spin coating and solvent casting explained as above. However, none of them could succeed unless a well dispersed polystyrene emulsion was obtained after an ultrasonication process, whose advantages will be further discussed in section 5.4.

A solvent which has good capabilities to both dissolve the polystyrene pellets and disperse the nanoparticles is the key factor to produce a good PS – ZnO nanocomposite film. Several common organic solvents were investigated to best dissolve the polystyrene:-

1) Acetone:- It was found that acetone did not dissolve the polystyrene pellets even in 8 hours. Only surface corrosion on the pellets could be observed.
2) Chloroform:- This solvent could dissolve the polystyrene quickly, leading to a very transparent and clear solution. But as a result of the spin coating or the solvent casting, the film showed poor transmittance accompanied with many tiny bubbles that formed inside it as seen under a microscope.
3) Ethyl acetate:- This solvent showed a similar performance to the chloroform, again with bubble formation.
4) Toluene:- This solvent appeared to be the ideal one to dissolve the polystyrene and give a transparent solution. The resulting film was ultra-clear and ultra-flat without any defect.

It can be concluded that although the chloroform and ethyl acetate solvents dissolved the polystyrene pellets fast, they could not provide a transparent polystyrene film. In contrast toluene was proven to have the ability to produce clear and transparent films.

The most probable reason for the differences in performance as above is due to different evaporation speeds of the solvents. As the chloroform and ethyl acetate have low boiling points (61 °C and 77 °C, respectively), they evaporate too fast to allow the bubbles to escape from the polystyrene matrix. The first solidified layer therefore encapsulates the air bubbles, causing a significant loss of transparency of the film as well as a poor surface roughness. However, when using a solvent with a high boiling point, such as toluene (it has a boiling point of 111°C), the internal air has enough time to move out from the polystyrene, leading to a much more transparent film. In addition, the low evaporation speed also allows the solution to have a good fluidity, thus keeping the surface flat and smooth during the evaporation.

To produce the PS – ZnO nanocomposite, a homogeneous polystyrene solution mixed with the ZnO nanoparticles was firstly prepared. The polystyrene pellets were dissolved in toluene at the concentration of 10% w/v. The ZnO nanoparticles, at the weight of 1%, then were added into the solution before it was sonicated in an ultrasonication bath for 1 hour.

A drop of liquid from a homogenized suspension of the PS – ZnO nanocomposite made up in a solution containing polystyrene dissolved in toluene was deposited on a very smooth ultra-sonicated cleaned glass square, which was mounted on a motorized axle rotator, to conduct a spin coating process. A CHEMAT Technology KW-4A spin coater (see Figure 2.4) was adopted in this experiment. The rotation speed was 300 rpm initially for 6 seconds in order to dispense and spread the solution over the substrate. The speed was then raised to 1500 rpm for 45 seconds to obtain a thin and flat composite film.

Figure 2.4 The CHEMAT Techonology KW-4A spin coater.

Alternatively, the as-prepared suspension was transferred into a petri dish to undergo a solvent casting process. After being cast in a fume cupboard at room temperature (overnight), a large and thick composite film (15 x 15 cm) was successfully obtained.

2.12 Incorporation of zinc-rich luminescent zinc oxide nanophosphors into polystyrene

The ZnO:Zn nanophosphors made as in section 2.4 were incorporated into a polystyrene matrix through the solvent casting technique. The casting procedures were similar to that described in the last section.

A polystyrene solution was made by dissolving it in toluene at the weight/volume ratio of 1:10. The 1wt% of ZnO:Zn nanophosphors were then weighed and added into the solution. After an ultrasonication for 1 hour, the uniform dispersed mixture was transferred into a petri dish in a fume cupboard, allowing the toluene to evaporate (overnight). The residual film was the PS – 1% ZnO:Zn nanocomposite.

Chapter 3 Characterisation of Nanoparticles and Their composites

3.1 Introduction

To investigate the nanoparticles/nanophosphors synthesized in the last chapter, a wide range of measurements were carried out to characterise their properties. These methods can be conveniently divided into two different areas of interest each of which aids in the characterisation of the nanomaterials. The first one being the techniques that characterise the structure of the materials, in the case of the current work the structural techniques used, were X-ray powder diffraction (XPRD), scanning electron microscopy (SEM) and transmission electron microscopy (TEM). The first of these techniques gives information on the crystal structures and size of the nano crystalline particles and their cell parameters. Whereas the second and third give information on the morphology and sizes of the nanoparticles. Light scattering was also used to give information on average particle size distribution in the nanoparticle phosphors.

The second area of interest is the spectral techniques in the current work these include laser Raman spectroscopy, UV-Visble spectroscopy and photoluminescent spectroscopy.

When the inorganic materials were embedded in a polymer matrix the excitation/absorption and emission properties were again used to both characterise them and to determine their performance.

For the polymer nanocomposites produced by incorporating the nanoparticles/nanophosphors, the properties of transmittance and the distribution of the nanocrystals are also important. Further properties that

need to be investigated include the UV screening performance of the nanoparticles and also the emission performance of the material achieved by incorporating the nanophosphors.

A UV lamp that can provide an excitation light of 254 nm or 366 nm was also used to examine the nanophosphors and the nanocomposites for a quick view by eye.

In addition as some of the materials were doped or coated, elemental mapping was used to give information into the nature of the coating and its distribution. An energy-dispersive X-Ray spectroscopy (EDS or EDX) was used for this purpose.

Details of the equipment are explained in this chapter.

3.2 X-Ray powder diffraction

X-rays, first discovered by Rontgen in 1885, are defined as an electromagnetic radiation that has a wavelength range from 0.01 to 100 Å, corresponding to a frequency range of 30 PHz – 300 EHz. However, only a small energy range of the x-rays usually with a wavelength between 0.5 and 2.5 Å are used to explore crystal lattices by recording and analysing diffraction patterns generated by the X-rays, as these wavelengths are close to an atomic distance in a crystal. [176]

The method of X-ray powder diffraction (XRPD) used in this work can determine the crystal structure and lattice parameters of the nanoparticles and nanophosphors produced by methods discussed in Chapter 2 according to Bragg's law:

$$2\,d\sin\theta = n\,\lambda$$

Where d, θ and λ are interplanar spacing, incident wave angle and incident wavelength, respectively.

The lattice parameters here are expressed as three vectors, **a**, **b** and **c**, which mean a, b and c in magnitude and α, β and γ in direction. An illustration of the parameters is shown in Figure 3.1 in a unit cell. Based on these parameters Bravais has proved that all crystal structures must fit to one of 14 unique lattices. These unique lattices, named Bravais Lattices, from the most symmetric structure to the least one include cubic, tetragonal, orthorhombic, rhombohedral, hexagonal, monoclinic and triclinic in which $a \neq b \neq c$ and $\alpha \neq \beta \neq \gamma \neq 90°$ [176].

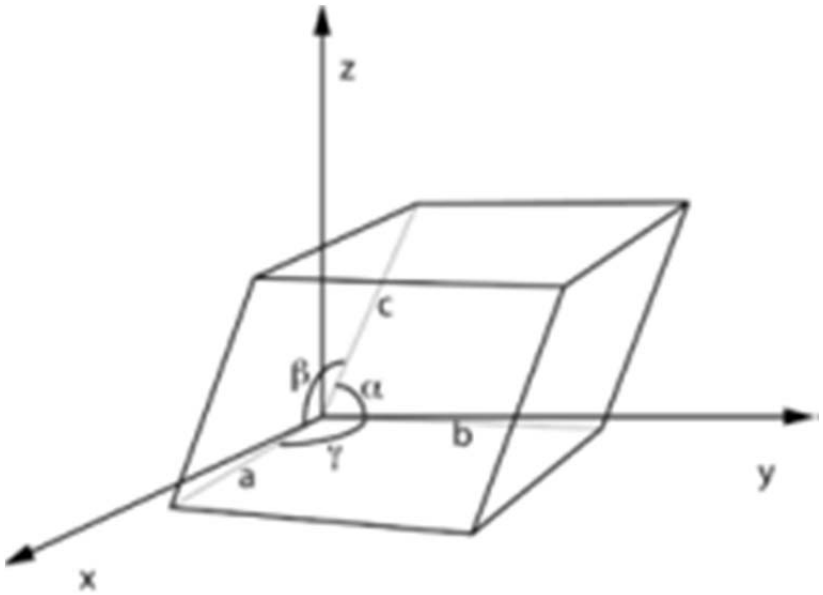

Figure 3.1 A unit cell showing parameters of both magnitude (a, b, c) and direction (α, β, γ)

Figure 3.2 Bruker X-ray powder diffractometer

X-ray powder diffraction patterns in this work were recorded using a Bruker D8 ADVANCE X-ray powder diffractometer (see Figure 3.2) that contains a copper tube emitting a strong X-ray with a wavelength of 1.54 Å and a position sensitive LynxEye^{TM} silicon strip detector. Further crystal information regarding crystal structures and cell parameters were analysed by fitting and refining the XRPD patterns through EVA and TOPAS computer programs.

For all the nanoparticles and nanophosphors in this work, the powders were placed, pressed and smoothed in the centre of a sample holder (see Figure 3.3) in order to achieve a flat surface of the XRPD sample before an X-ray scanning process. This sample preparation produced uniform fine powders with all possible crystallite orientations, hence eliminated specific orientations in the crystals which bring more difficulty to identify the phases of the powders. The well prepared XRPD samples were then loaded into a scanning chamber (see Figure 3.4) which is able to accommodate up to 9 samples and in addition automatically change and rotate them during the scanning.

Figure 3.3 XRPD sample holder

All XRPD data were collected from measurements of a step scan mode from 5° to 100° (2θ) for 35 minutes with a sample rotation. The rotation also could reduce the preferential orientations possibly existing in the powder samples. On some occasions, longer scanning time such as 2.5 hours was applied in order to reduce the background noise, especially for very fine nanoparticles whose XRPD patterns are not that intensive.

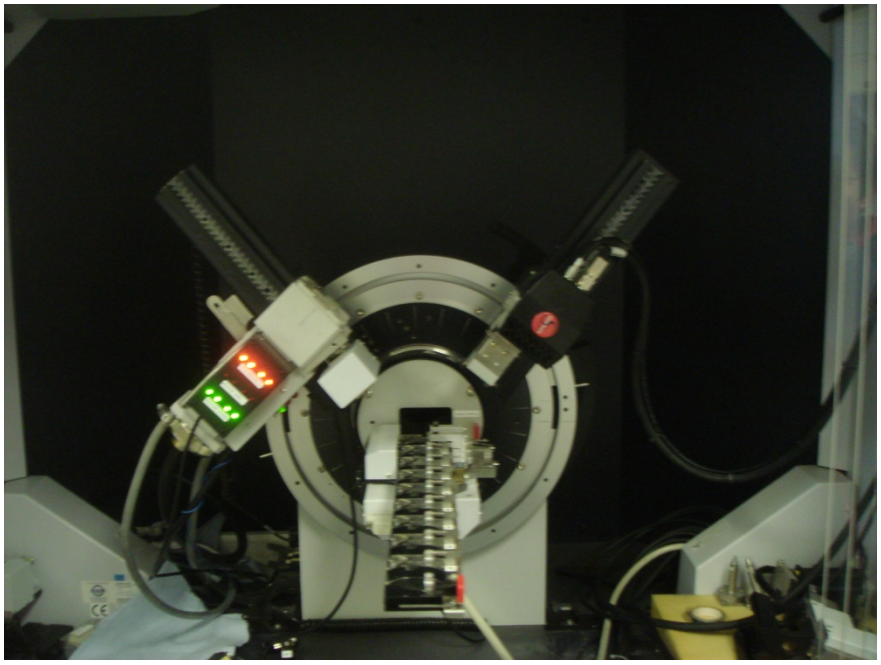

Figure 3.4 The scanning chamber on the Bruker X-ray powder diffractometer

3.3 Scanning electron microscopy

Scanning electron microscopy (SEM) is used for imaging purposes to investigate surface topography and composition of samples. It is based on an electron column providing an illuminating system and a specimen chamber where samples can be placed and there are a range of detectors for different types of analysis.

In the SEM system, there is an electron gun emitting an electron beam with very high energy. The electrons travel through a series of electric and magnetic fields also called condenser lenses and get focused to an extremely tiny spot at the sample surface, where an interaction between the electrons and the sample surface occurs to provide various signals such as secondary electrons, backscattered electrons, Auger electrons, characteristic X-ray and cathodoluminescence radiation. These radiations can be detected and used to visualise the detecting area resulting in SEM images. The entire system must be in a vacuum condition in order to prevent the electrons generated by the electron gun from colliding with gas (air) molecules. [176]

A ZEISS SUPRA 35VP field emission scanning electron microscope (see Figure 3.5) was employed to observe particle sizes and morphology of the $LiAlO_2$:Fe, ZnO, ZnO:Zn and coated ZnO samples as well as their distribution in the nanocomposites. The microscope can be operated in a high vacuum condition and also in variable operating pressures for exploring samples in their natural states, especially if samples are insulating such as polymer composites. The microscope is equipped with a GEMINI column which can provide very high resolution both in high vacuum condition and in a certain operating pressure.

In some cases, the samples were coated with a layer of gold using a POLARON SPUTTER coater (see Figure 3.6) before being located in the specimen chamber to avoid charging under the electron beam.

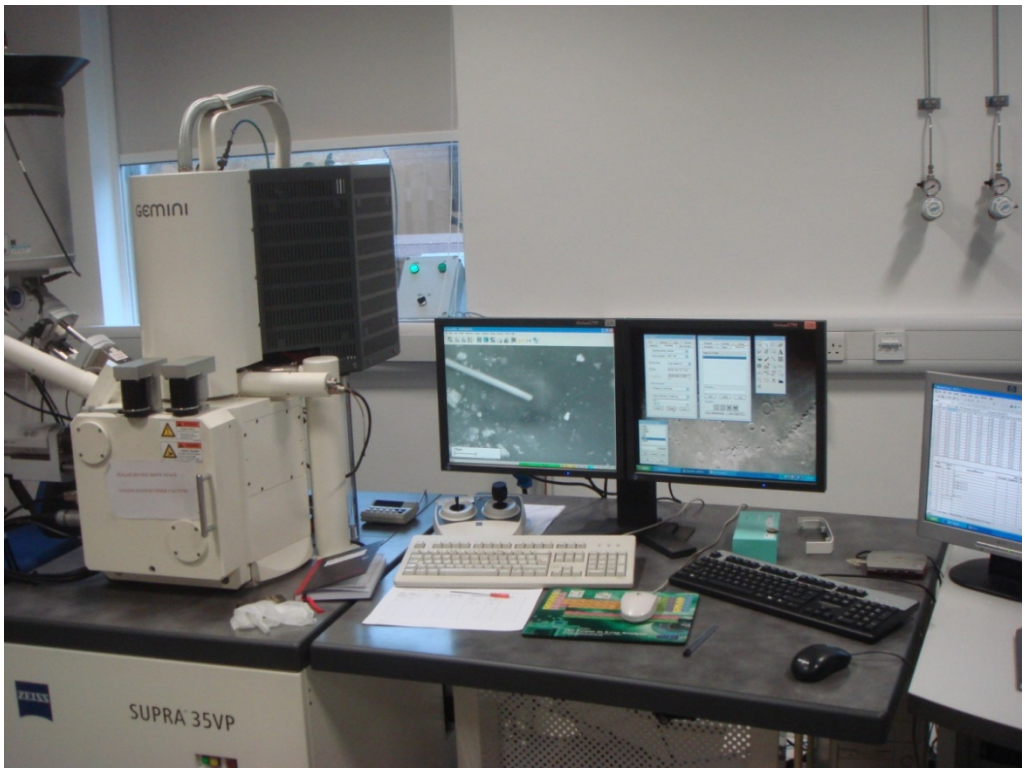

Figure 3.5 ZEISS SUPRA 35VP scanning electron microscope

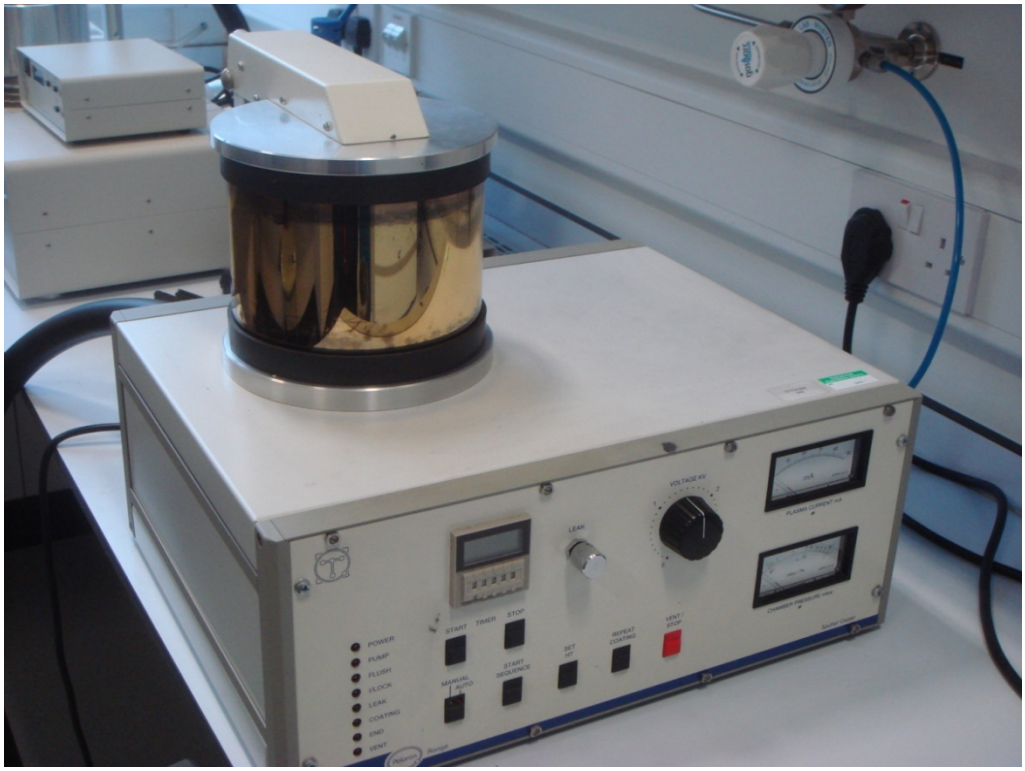

Figure 3.6 POLARAN SPUTTER gold coater

3.4 Transmission electron microscopy

Transmission electron microscopy (TEM) is an imaging technique used to observe fine objects (normally below 100 nm) with a similar working principle as that of a light microscope. However in this case high energy electrons emitted from an electron gun are used as a source rather than using a source of visible light. A minimum size can be detected by an ordinary light microscope is approximately 0.2 μm due to the diffraction limit of visible light [176]. If an electron beam is set up as the source for the microscope, objects can be detected in much lower sizes, so the TEM is developed.

In the TEM system, the electron gun generates electrons which travel downward through a series of lenses including a condenser lens, an objective lens and a projective lens. Specimens can be mounted between the condenser lens and the objective lens. The electrons eventually arrive at a phosphor screen and herein provide a TEM image. Like the SEM system, the TEM chamber must be in a high vacuum condition to allow the free movement of the electrons.

For this work, a JEOL JEM-2000FX transmission electron microscope equipped with a CCD camera (see Figure 3.7) was used to investigate the ZnO nanoparticles and their derivatives. The microscope has a LaB_6 electron gun and is able to provide an accelerating voltage up to 200 kV.

To prepare samples for the TEM analysis, a very tiny amount of the nanoparticles (the ZnO and its derivatives) were dispersed in methanol (roughly 2 ml) by an ultrasonication process. A small drop of the solution was placed on a carbon coated TEM copper grid which was then allowed to be dried completely. The dried carbon coated grid was placed in the sample arm stage of the microscope and this was then inserted into the microscope for study.

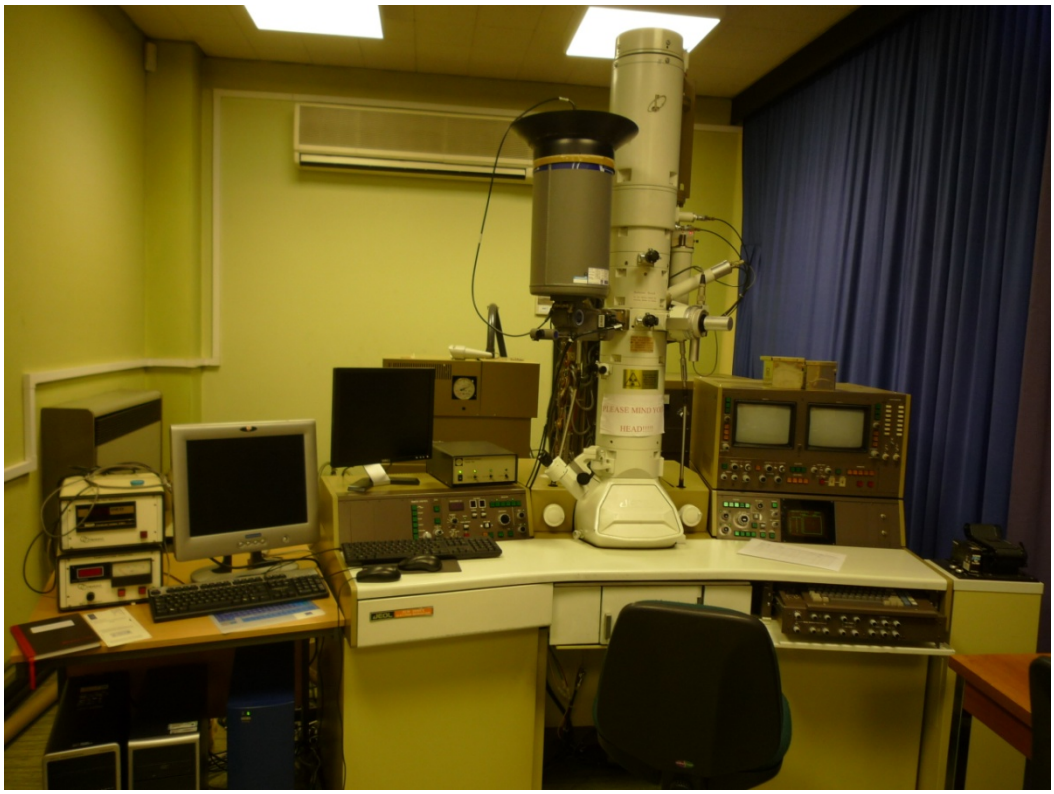

Figure 3.7 JEOL JEM-2000FX transmission electron microscope

3.5 Raman spectroscopy

Raman spectroscopy is a technique based on Raman scattering to detect vibrations within molecules/crystals in order to aid in the identification of chemical structures and physical forms of substances from a Raman spectral pattern. The substances that can be examined by Raman spectroscopy include all physical states such as solids, liquids and vapours. [177]

The Raman scattering mentioned above is a process of an inelastic light scattering where there is an energy transform between incident photons and scattered ones. So Raman spectroscopy detects this Raman scattering by using a very strong single frequency of light (laser) to target samples. The incident light interacts with molecules or the lattice (if it is a solid) and distorts the cloud of electrons to be excited to a much high 'virtual state', which is not stable and where the excited electrons return to the low energy level soon by quickly re-radiating photons. These photons can lead to Raleigh scattering which is elastic and dominant, and Raman scattering including Stokes scattering and anti-Stokes scattering (see Figure 3.8). [177]

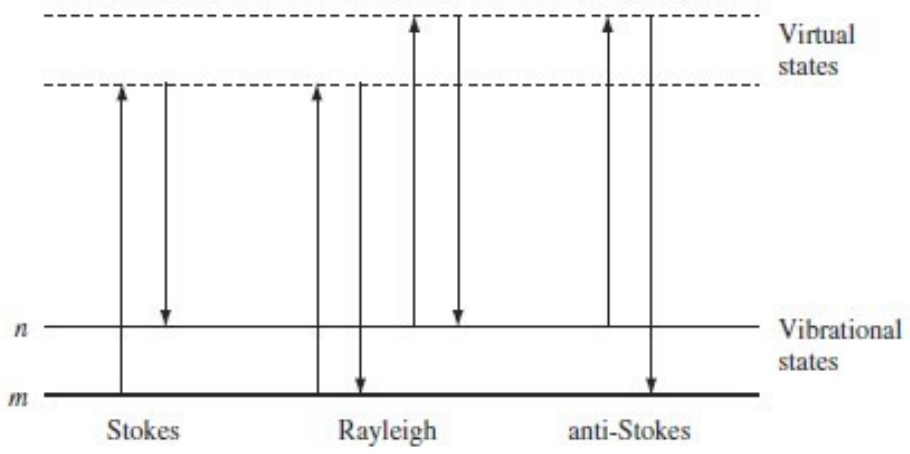

Figure 3.8 Diagram of the Raleigh and Raman scattering.

In this work, Raman spectral patterns were obtained by means of a HORIBA JOBIN YVON LabRAM HR800 spectrometer (see Figure 3.9). This instrument contains three different incident sources:- a green laser of 532 nm wavelength, a red laser of 633 nm and an infrared laser of 1064 nm. Apart from these, an air cooled CCD detector is equipped to detect signals in the visible region, and another CCD detector cooled by liquid nitrogen is also employed to detect infrared signals.

To investigate the nanoparticles and nanophosphors in Chapter 2, the green laser (532 nm) was used on the samples as this high energy source can provide better signals thus leading to an intensive Raman spectrum. After the instrument was calibrated on a standard silicon sample, the data were collected in the range of 100 – 1500 cm^{-1} and the obtained Raman spectra were analysed by a LabSPEC computer program.

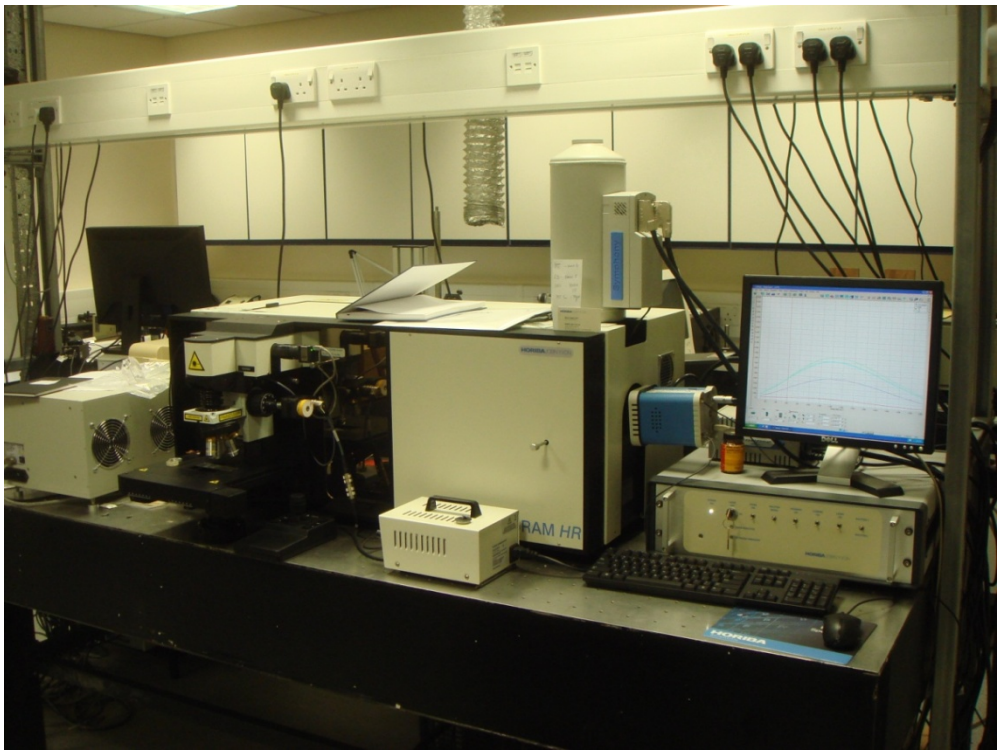

(a)

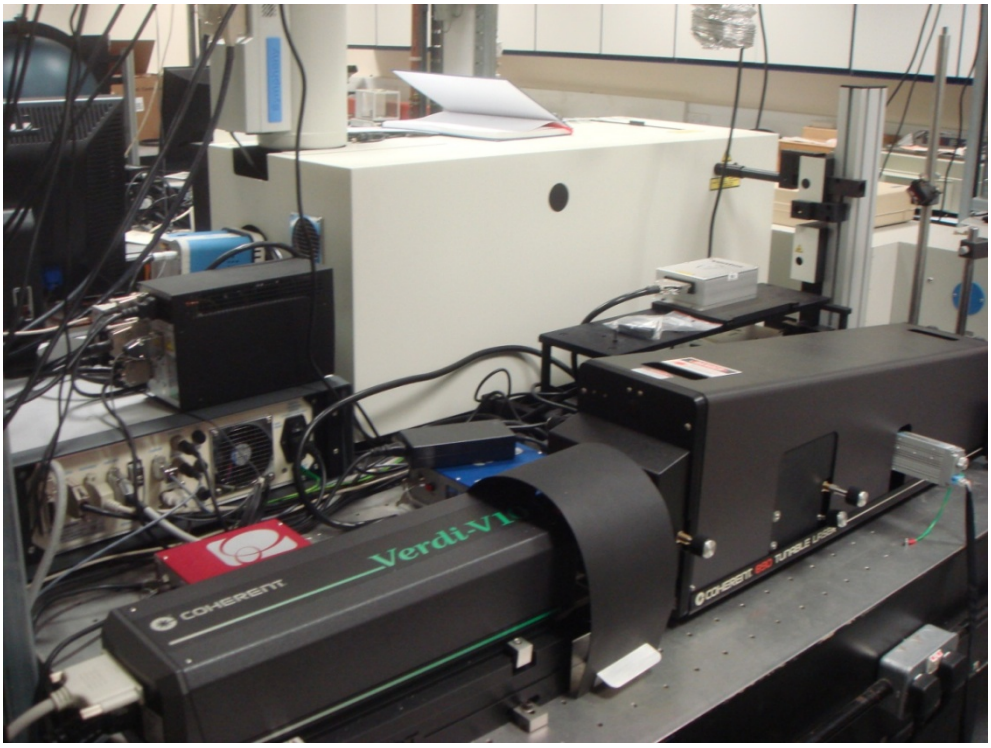

(b)

Figure 3.9 HORIBA JOBIN YVON LabRAM HR800 spectrometer: (a) front view; (b) back view showing external green and infrared sources.

3.6 UV-Visible spectroscopy

When a substance is exposed to ultraviolet light or visible light, it may have a capability to absorb light at a certain wavelength as the energy of the light matches an electronic transition within its molecules and/or lattice (if it is a solid). This light is absorbed to excite an electron to another orbital with a higher energy level (i.e. the electron is promoted from a ground state to an excited state). UV-Visible spectroscopy is used to detect and record this absorbance at any wavelength normally in a region from 200 to 800 nm. Based on this, absorption spectra, transmission spectra and reflection spectra can be obtained. [176]

A typical UV-Visible spectrometer (see Figure 3.10) contains a light source (UV lamp), a diffraction grating unit, a filter, a half mirror, four normal mirrors and two detectors (one is for the sample and the other one is for the reference). There is a light slit (slit 1) used to determine the amount of light entering the diffraction grating unit. The half mirror here is employed to split the incident beam (from the light source) equally into two beams with exactly same intensities. This therefore ensures that both the sample and the reference receive the same monochromatic beam. The intensities of the beams passing through the sample or the reference then are measured and compared by the detectors to provide the spectra. [176]

A PerkinElmer Lambda 650 S UV-Visible spectrometer (see Figure 3.11) was used to obtain absorption spectra, transmission spectra and reflectance spectra of the nanoparticle powders of the ZnO and its derivatives. Transmittance and absorption of PP nanocomposite and PS nanocomposite films were also investigated. A quartz cuvette was employed to contain the powder samples in solution as it is transparent in the UV region.

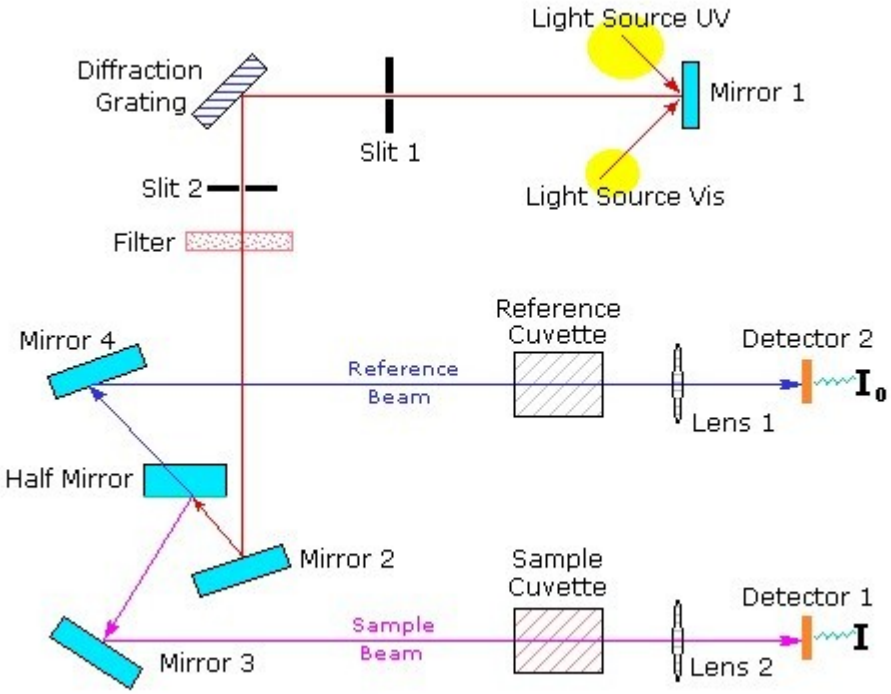

Figure 3.10 Schematic of an UV-Visible spectrometer

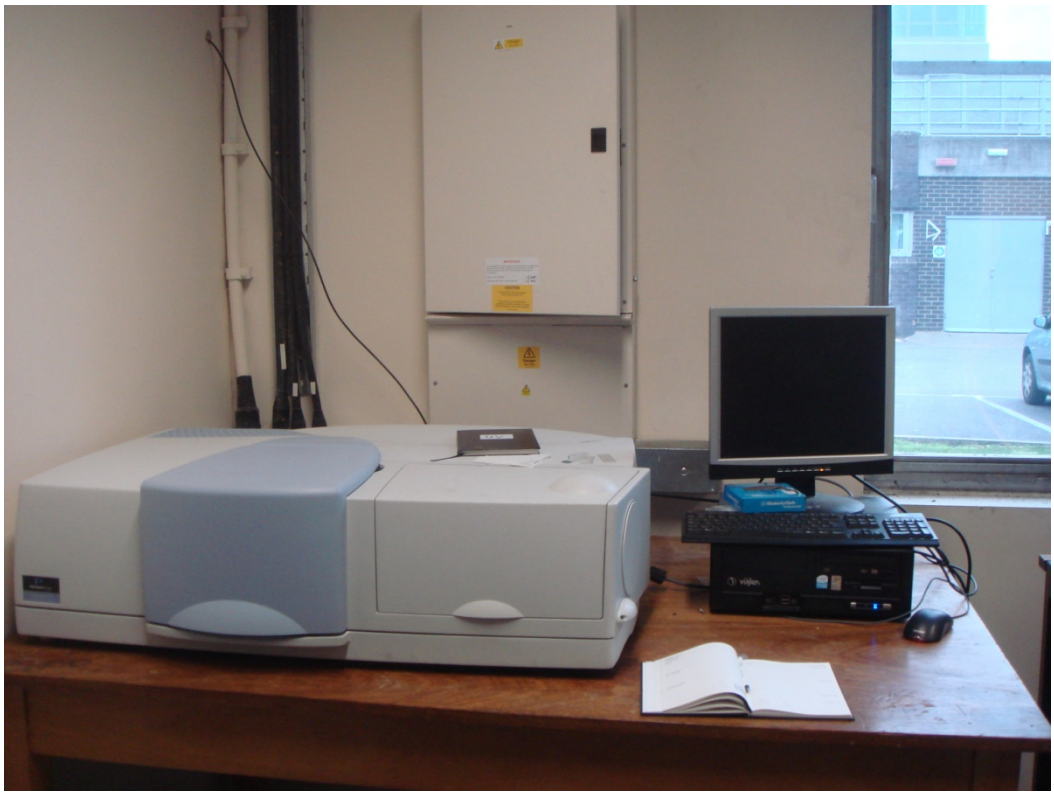

Figure 3.11 PerkinElmer Lambda 650 S UV-Visible spectrometer

3.7 Photoluminescence spectroscopy

Photoluminescence spectroscopy is an effective technique to investigate excitation and emission characteristics of photoluminescent substances. It is also widely used to determine the lifetimes of the excited states of phosphor materials.

A Bentham photoluminescence spectrometer (see Figure 3.12) was used to study the excitation and emission spectra of the $LiAlO_2$:Fe and the ZnO:Zn nanophosphors. The spectrometer was equipped with a xenon lamp source that can emit a range of wavelengths to excite the samples, and with an M300 programmable grating monochromater photometer system. The obtained results were studied using a $BenWin^+$ software.

Another photoluminescence spectrometer, HORIBA Jobin Yvon Fluorolog 3 (see Figure 3.13), was employed to compare the excitation and emission results of the nanophosphors with the results obtained from the Bentham. It was also used to investigate the luminescent characteristics of the PP – $LiAlO_2$:Fe and the PS – ZnO:Zn nanocomposite films. The resulting spectra were obtained and studied by a FluroEssence software.

Figure 3.12 Bentham photoluminescence spectrometer

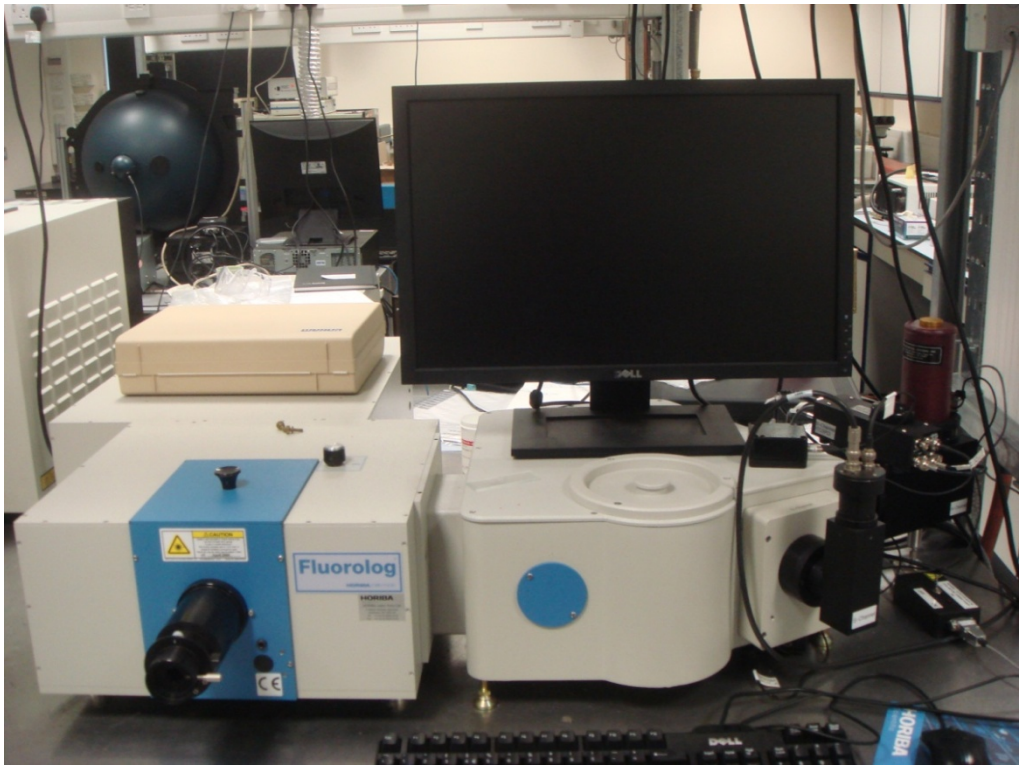

Figure 3.13 HORIBA Jobin Yvon Fluorolog 3 photoluminescence spectrometer

Chapter 4 Investigation of Iron Doped Lithium Aluminate Phosphor and Its Behaviour in Composites

4.1 Introduction

Inorganic phosphors are widely used in lighting and displays. Examples of uses are in:- lamps, lighting panels, light engines and display screens for home and mobile platforms. In section 1.3 the characteristics of a phosphor were summarised as that a phosphor consists of a host lattice and a doped activator present in small concentrations.

Conventional red phosphors including $CaAlSiN_3:Eu^{2+}$ [178], $Y_2O_2S:Eu^{3+}$ [179] and $CaTiO_3:Pr^{3+},Bi^{3+}$ [180], $Y_2O_3:Eu^{3+}$ [181] have been developed for a variety of uses in the current market. These phosphors are dependent on very expensive dopant activators which are the rare earth elements. These are costly due to restricted supplies in the market place. In addition those phosphors often involve complicated synthesis which are time consuming and therefore costly.

To avoid the use of expensive rare earth based phosphors for applications where large amounts are necessary for relatively low cost products a cheap alternative is therefore a prerequisite. To meet this challenge it is necessary to design phosphors containing a very small amount of rare earth dopants or preferentially none at all.

One such phosphor that has been investigated by Aoyama et al [182] is lithium aluminate doped with iron ($LiAlO_2:Fe$). This phosphor is easily synthesised and its raw materials are cheap and abundant on the

earth. Aoyama et al [182] reported that the $LiAlO_2$:Fe was made from a wet chemical reaction method; it manifests a strong red light with the main emission peaking around 670 nm when it is excited by a wavelength at 270 nm. Others reported that the $LiAlO_2$:Fe was also excited by broad ultraviolet and blue light resulting in an emission of infrared [183]. These unique properties lead to the $LiAlO_2$:Fe phosphor being a very promising red emitter for certain uses in industry as a cheap alternative to rare earth doped phosphors.

Lithium aluminate is the host lattice for the $LiAlO_2$:Fe phosphor. There are three different compositions according to different Li/Al ratios:- Li_5AlO_4, $LiAlO_2$ and $LiAl_5O_8$ [182], among which, the last two have been well studied [184] [185] [186]. Many papers have been focussed on doping the lithium aluminate matrix with various dopants such as Fe^{3+} [187] [188], Tb^{3+} [189], Cr^{3+} [190], Cr^{4+} [191] [192] [193] and Mn^{2+} [194] [195]. Several synthetic techniques have been used to synthesise the lithium aluminates, including sol-gel [182], flame spray pyrolysis [183], hydrothermal synthesis [196], solid state synthesis and a combustion synthesis method [149]. A phase equilibrium diagram of the Li_2O – Al_2O_3 system is displayed in Figure 4.1, revealing the range of Li/Al compounds on the basis of temperature.

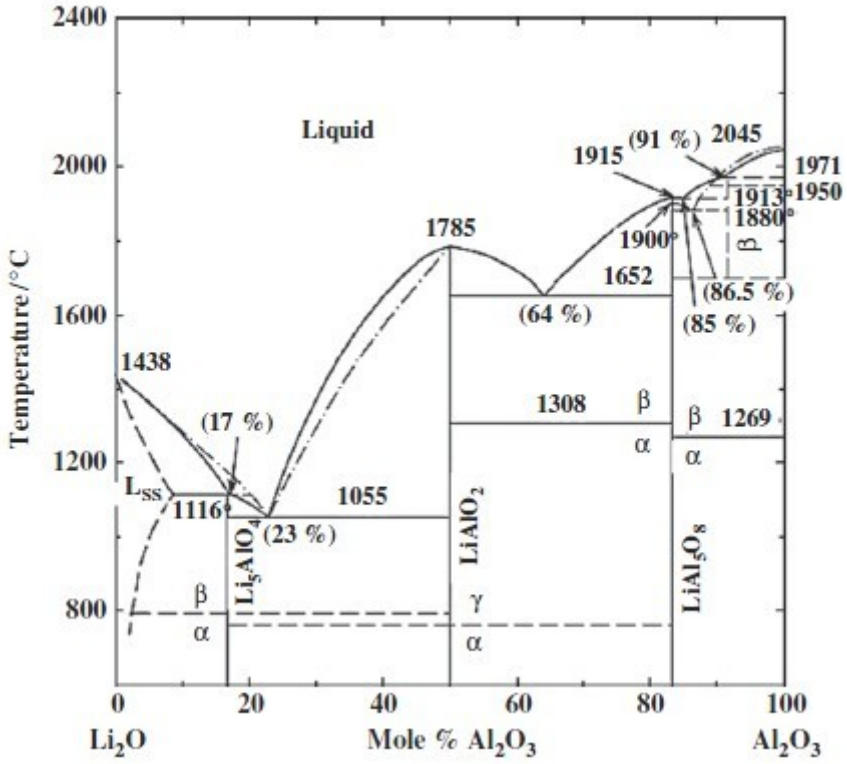

Figure 4.1 Phase equilibrium diagram of Li_2O – Al_2O_3 system **[182]**

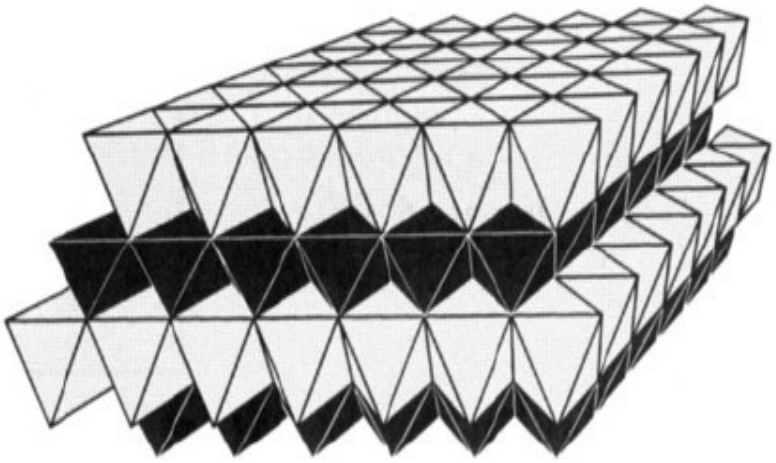

Figure 4.2 Illustration of trigonal α-$LiAlO_2$. LiO_6 and AlO_6 units are represented with shaded and black octahedra, respectively. **[197]**

The $LiAlO_2$ lattice that was the choice for iron doping to make the $LiAlO_2$:Fe phosphor in this work was first synthesized by Weyberg in 1906 [198]. It exists in three well known allotropes:- 1) α-$LiAlO_2$ [199], normally formed in the low temperature range (blow 400 °C) with a trigonal structure (see Figure 4.2); 2) β-$LiAlO_2$ [200], formed in the moderate temperature range (from 400 °C to 800 °C) with an orthorhombic structure (see Figure 4.3); and 3) γ-$LiAlO_2$ [197] [201], formed in the high temperature range (above 1000 °C) with a tetragonal structure (see Figure 4.4). The γ allotropic form is the most stable one and is the only one available for the doping of activators [195]. It has therefore attracted both theoretical and practical attention leading to γ-$LiAlO_2$ being widely used in industrial applications. For instance, γ-$LiAlO_2$ can be used as an insulating inert matrix to contain the carbonate electrolyte between electrodes for application in molten carbonate fuel cells [202]; it also can be used as an irradiation blanket for nuclear fusion reactors due to its low susceptibility to thermal and chemical variation as well as high radiation resistance properties [203]. Marezio reported the γ-$LiAlO_2$ crystallized in space group $P4_12_12$ or its enantiomorph $P4_32_12_1$ [185], with one unit cell containing four formula units where both Al^{3+} and Li^+ cations are coordinated by four oxygen ions (see Figure 4.5).

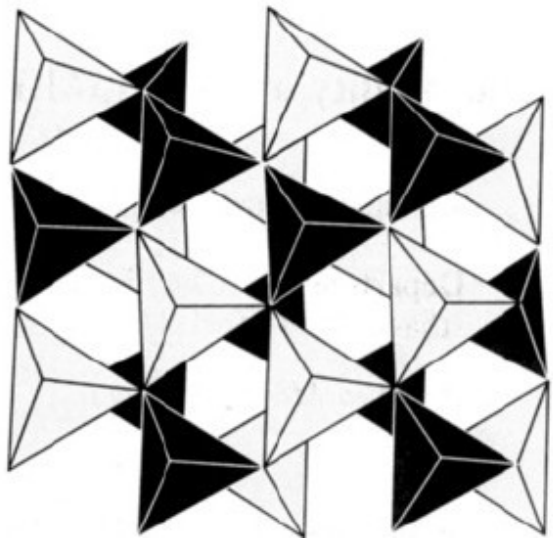

Figure 4.3 Illustration of orthorhombic β-$LiAlO_2$. LiO_4 and AlO_4 units are represented with shaded and black tetrahedral, respectrively. **[197]**

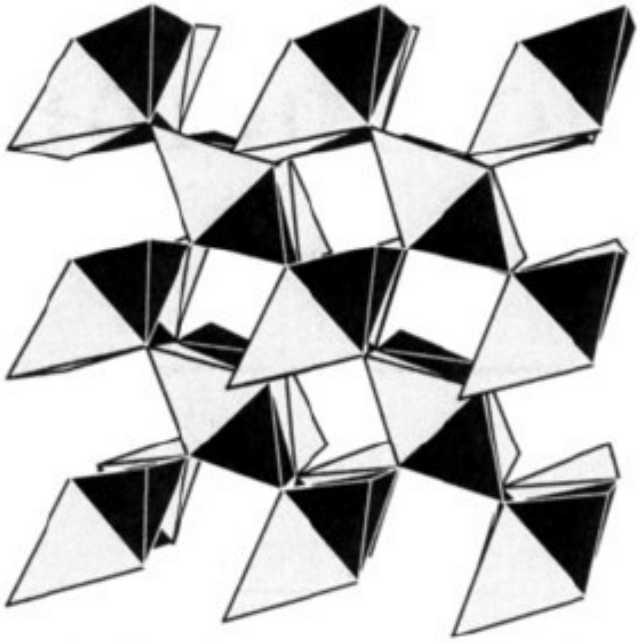

Figure 4.4 Illustration of tetragonal γ-$LiAlO_2$. LiO_4 and AlO_4 units are represented with shaded and black tetrahedral, respectively. **[197]**

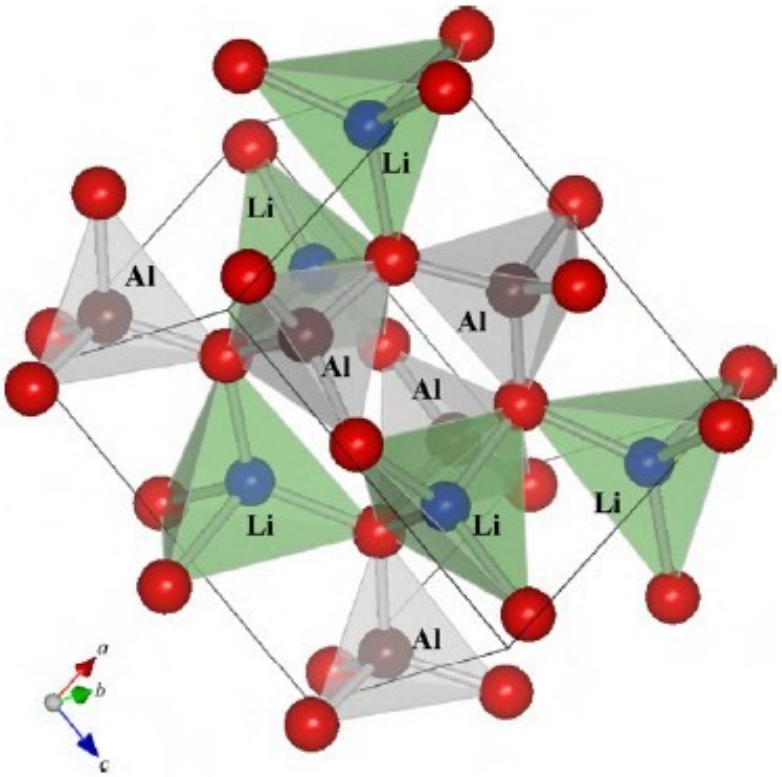

Figure 4.5 Illustration of one unit cell of γ-$LiAlO_2$ crstal. **[195]**

In this chapter, the iron doped lithium aluminate ($LiAlO_2$:Fe) phosphors are fully discussed on the basis of two synthetic techniques, firstly a solid state reaction (see section 2.2) and then a flame spray pyrolysis preparation (see section 2.3), which respectively result in bulk phosphor particles and nano-phosphor particles. Their crystal structures and morphology were also studied. The photoluminescent spectra of the phosphors are presented, indicating that the $LiAlO_2$:Fe absorbs and is excited by a broad wavelength range of ultraviolet light and re-emits the energy in the form of light in the red and infrared regions of the electromagnetic spectrum. These absorption/excitation and emission characteristics make this phosphor an ideal candidate material to prevent or reduce damage by UV radiation to polymers when present as either a surface coating for the polymer or as a filler within the polymer. In addition this phosphor facilitates considerable benefit if it is used for plant growth illumination and in green house covers. This work has been published at the International Displays Workshop (IDW) 2011 and its proceeding [183].

4.2 Bulk $LiAlO_2$:Fe characterisation and properties

A $LiAlO_2$:Fe bulk phosphor was synthesised using the solid state reaction technique (see section 2.2). From the XRPD pattern shown in Figure 4.6, the pure tetragonal phase of γ-$LiAlO_2$ was clearly identified without the presence of any impurity phases. In the literature, it has been reported that the cell dimensions of pure γ-$LiAlO_2$ are between a = 5.1687 Å, c = 6.2679 Å and a = 5.1698 Å, c = 6.2779 Å [185] [204]. However the strong and sharp lines shown in the diffractogram (see Figure 4.6) indicate that good crystallinity of the as-prepared $LiAlO_2$:Fe phosphor was achieved during the firing process with cell parameters of a = 5.1730(80) Å and c = 6.2806(13) Å. The cell size here showed values similar to those in the literature, implying that the 1mol% of the iron doping fitted in the γ-$LiAlO_2$ lattice and hardly affected the cell parameters.

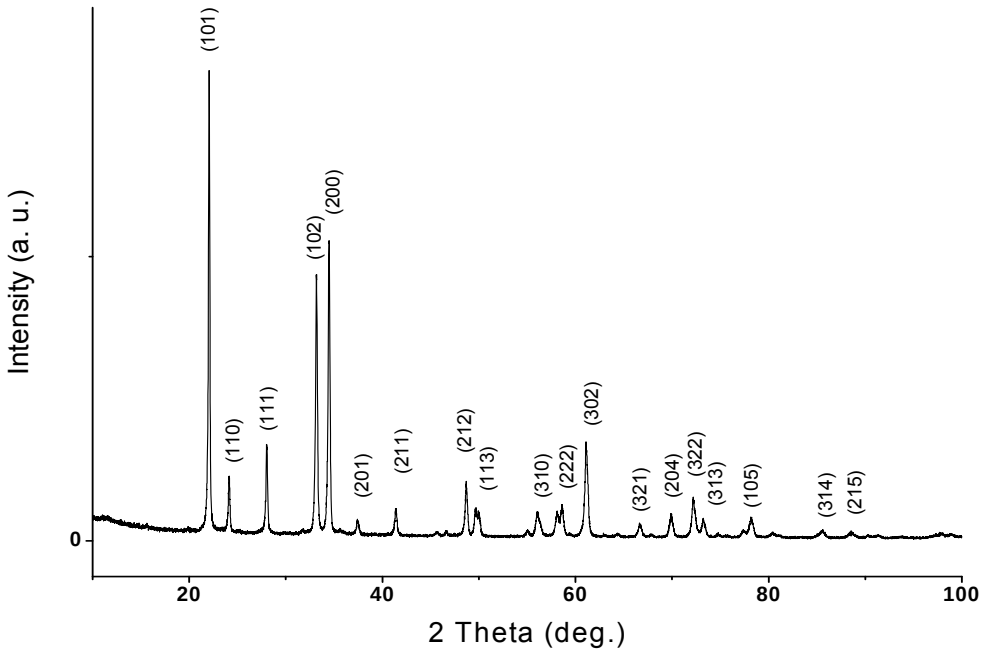

Figure 4.6 X-ray diffractogram of the bulk $LiAlO_2$:Fe phosphor

The morphology of the bulk $LiAlO_2$:Fe phosphor was examined and a SEM micrograph is displayed in Figure 4.7. It is apparent that uniform particles were synthesised and were around half a micron in size with sphere- and pillar-like shapes. The well-formed crystals not only give a good X-ray diffractogram (see Figure 4.6), but facilitate a Raman spectrum with strong peaks presented in Figure 4.8.

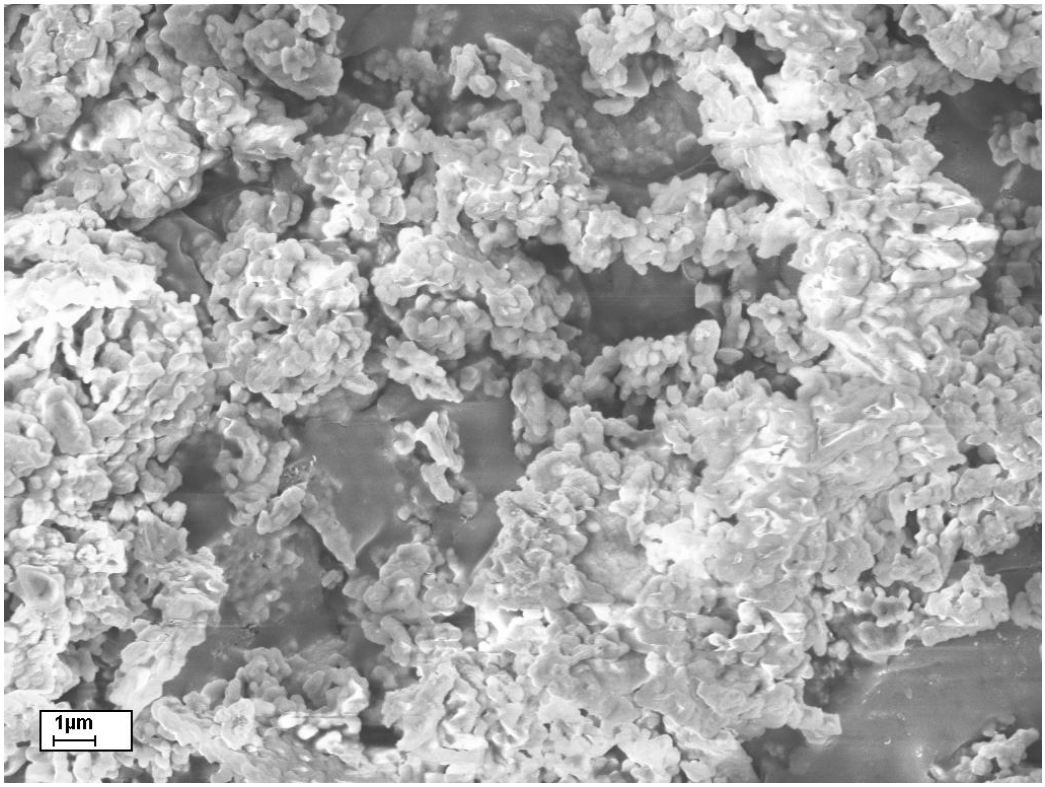

Figure 4.7 SEM image of the bulk $LiAlO_2$:Fe phosphor

Figure 4.8 represents the Raman spectrum of the bulk $LiAlO_2$:Fe phosphor in the range from 300 to 1300 cm^{-1} (Raman shift). The sample was excited by the green laser line at 532 nm. The pure tetragonal phase of the phosphor was also characterised using Raman spectroscopy. The Raman bands at 368, 401, 506, 610, 787, 807 and 841 cm^{-1}, respectively characterise the tetragonal phase [205] [206]. It also can be found that there is a small Raman band at 1088 cm^{-1} which is due to the presence of

carbonate groups. The reason is because the $LiAlO_2$:Fe phosphor tends to capture and absorb carbon dioxide (CO_2) in the atmosphere [207] [208] [209] [210]. Tiny carbonate groups were therefore formed in the sample and they were evidently detected by the Raman spectroscopy due to its high sensitivity.

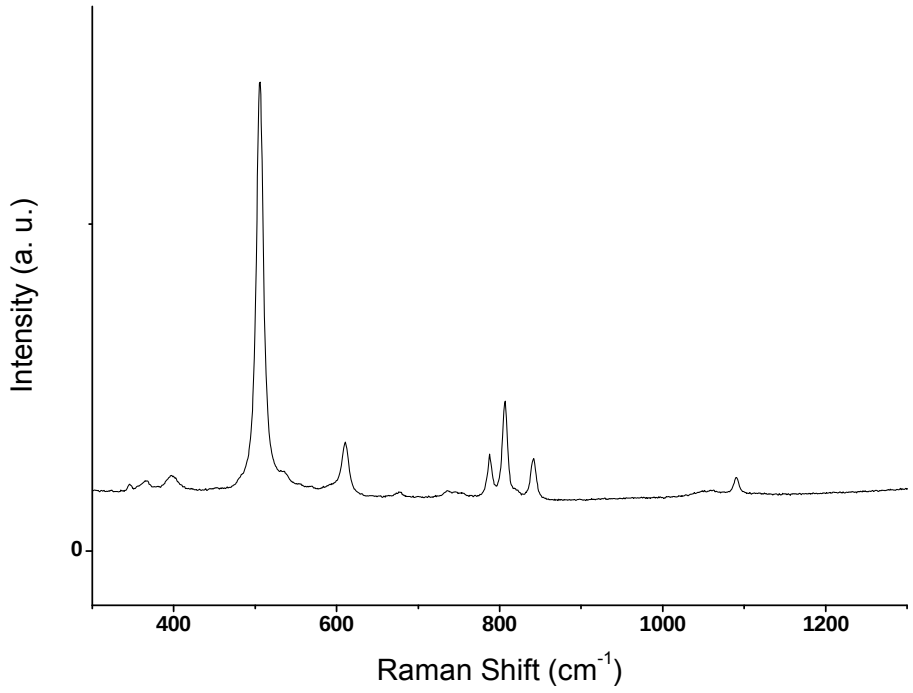

Figure 4.8 Raman spectrum of the bulk $LiAlO_2$:Fe phosphor

Photoluminescence excitation and emission spectra of the $LiAlO_2$:Fe bulk phosphor are presented in Figure 4.9. Obviously, the phosphor could be excited by the whole UV region of the electromagnetic spectrum with the main excitation peaks at 271, 350 and 390 nm, respectively, and in addition, it also could be excited by blue light ranging from 400 to 480 nm. Under the excitation of broad UV light and blue light, the phosphor could re-emit infra-red light with a wide emission peak centred at 747 nm.

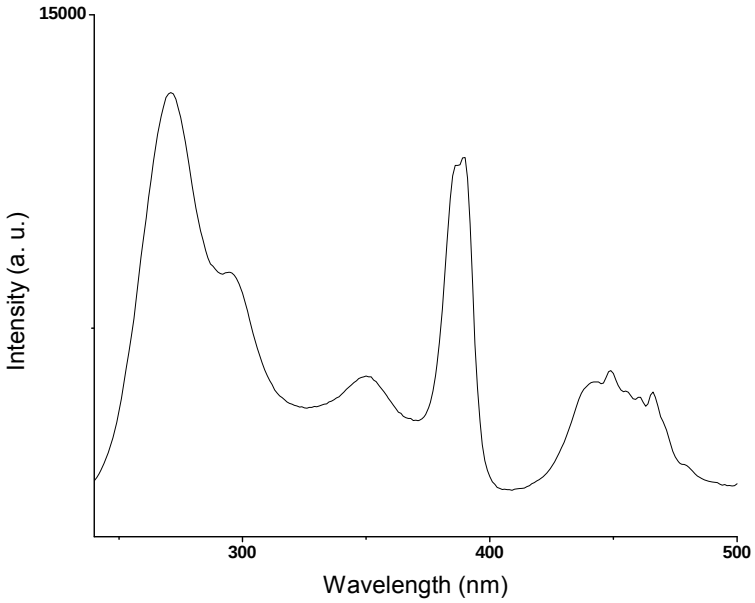

(a)

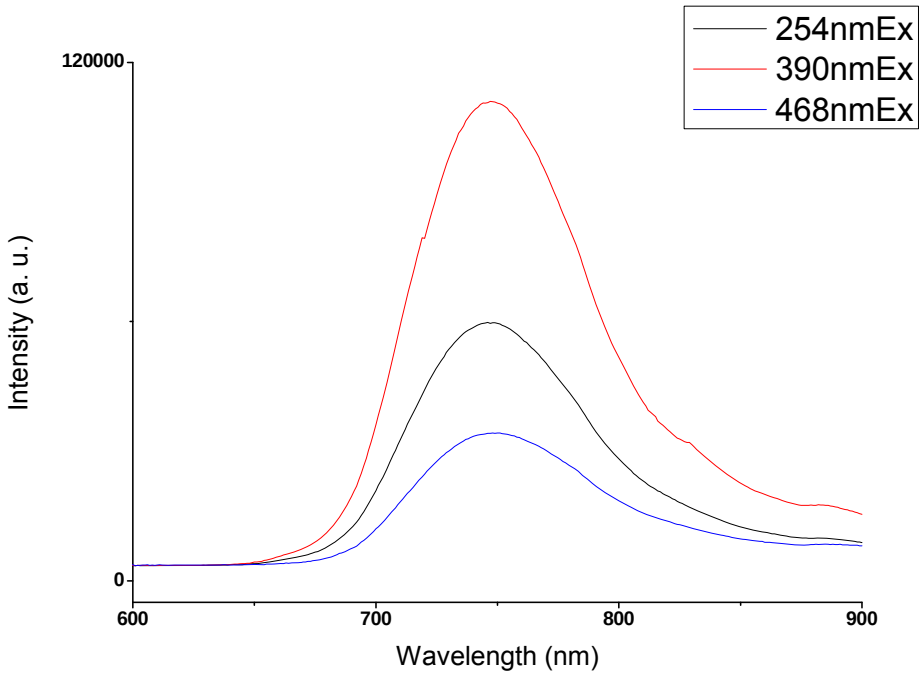

(b)

Figure 4.9 The $LiAlO_2$:Fe bulk phosphor: (a) Photoluminescence excitation spectrum, monitored at 740 nm; and (b) Photoluminescence emission spectra under 254 nm, 390 nm and 468 nm excitation.

4.3 $LiAlO_2$:Fe nanophosphors characterisation and properties

$LiAlO_2$:Fe nanophosphors were prepared by Johnson Matthey, and the latter has the capability to make them on an industrial scale (see section 2.3). The nanoparticles as first formed are not single phase, but annealing at 650˚C at JM significantly improved the crystallinity of the nanoparticles as shown by the X-ray diffractograms presented in Figure 4.10. The powder X-ray diffraction data of the annealed material was in good agreement with the known literature for the $LiAlO_2$ phase [149] [182] [204]. However, unlike the diffractogram of the pure tetragonal γ-$LiAlO_2$ phase shown in Figure 4.6, here some other lines of the annealed material could also be identified. These lines were ascribed to the presence of Li_2CO_3 which was the excess reactant left by the flame spray pyrolysis. The resulting materials and crystal information of the $LiAlO_2$:Fe nanophosphors before and after annealing are presented in Table 4.1.

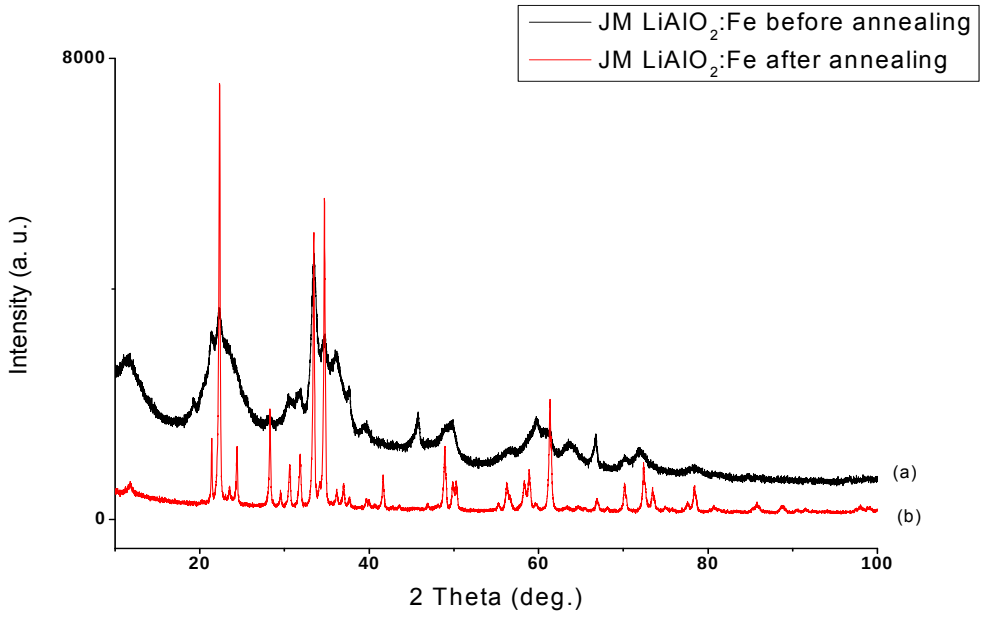

Figure 4.10 X-ray diffractograms of the $LiAlO_2$:Fe nanoparticles (a) as-prepared; (b) annealed at 650°C.

Table 4.1 Phases present and crystallite sizes within the $LiAlO_2$:Fe nanophosphors

Sample	Phase present in XRPD data and lattice parameters	Crystal size (nm)
JM $LiAlO_2$:Fe before annealing	$LiAlO_2$, a = 5.2211(19) Å, c = 6.3007(32) Å 38.48(50)% of this material is present	10.000(45)
	Li_2CO_3, a = 8.3223(98) Å, b = 5.0688(65) Å, c= 6.3418(41) Å, β= 114.706(62)° 12.31(16)% of this material is present	15.900(16)
	$Al_{2.667}O_4$, a = 5.0527(27) Å, c = 6.2185 (71) Å 49.21(66)% of this material is present	3.110(86)
JM $LiAlO_2$:Fe after annealing	$LiAlO_2$, a = 5.17689(82) Å, c = 6.27868(13) Å 79.92(14)% of this material is present	81.54(45)
	Li_2CO_3, a = 8.38236(77) Å, b = 4.97459(44) Å, c= 6.20861(30) Å, β= 114.8457(56)° 20.08(14)% of this material is present	73.30(15)

Figure 4.11 presents the SEM micrograph images of the $LiAlO_2$:Fe nanophosphors. Before annealing, the $LiAlO_2$:Fe consists of approximately 20 nm sized particles (Figure 4.11(a)) with sphere-like morphology. Annealing resulted in agglomeration to form larger aggregated particles (Figure 4.11(b)), and larger crystal sizes (Figure 4.11(c)) with plate- and star-like morphology which are probably due to both the presence of $LiAlO_2$:Fe and Li_2CO_3 existing amongst the nanoparticles.

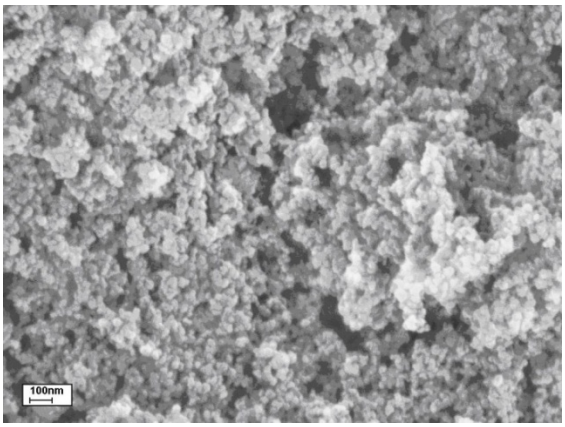

(a)

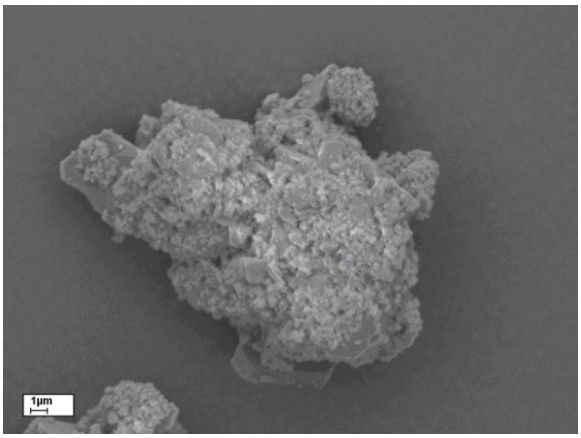

(b)

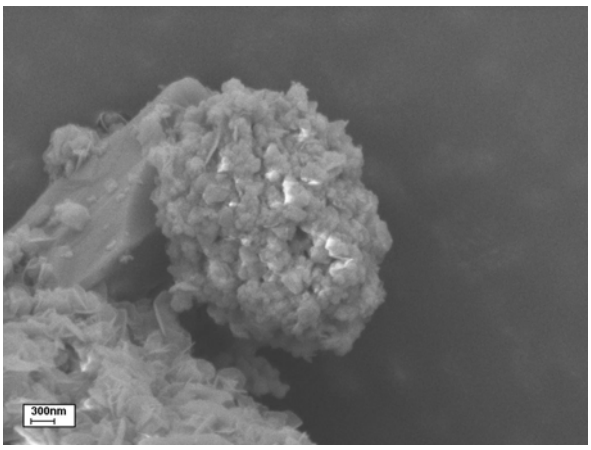

(c)

Figure 4.11 SEM images of the Johnson Matthey $LiAlO_2$:Fe nanophosphors: (a) before annealing (scale bar 100 nm); (b) after annealing at 650˚C with low magnification (scale bar 1 µm); and (c) after annealing at 650°C with high magnification (scale bar 300 nm)

The Raman spectrum of the heat treated phosphor is shown in Figure 4.12. It exhibits bands at 368, 401, 506, 610, 787, 807 and 841 cm^{-1} due to the γ-$LiAlO_2$ lattice [205] [206]. Additionally, compared with the Raman spectrum of the bulk $LiAlO_2$:Fe in Figure 4.8, it can be noticed that there is a much stronger Raman band at 1088 cm^{-1} which is evidence for the existence of the impurity phase of the Li_2CO_3 residue. This band is due to the symmetric stretching vibrations of the Li_2CO_3 molecules [211]. The result is in good agreement with the findings from the X-ray diffractogram in Figure 4.10.

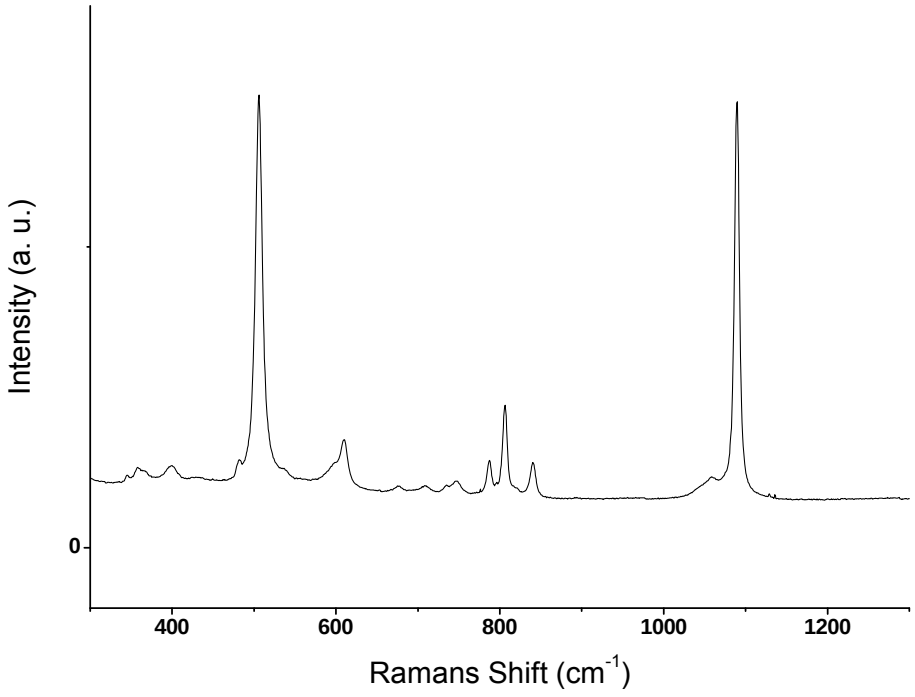

Figure 4.12 Raman spectrum of the $LiAlO_2$:Fe nanoparticles after annealing

Figure 4.13(a) presents the excitation spectrum of the $LiAlO_2$:Fe nanophosphor before annealing; it is broad and spans the entire UV with

the peaks centred at 267 nm, 324 nm and 390 nm respectively, in addition it also has bands in the blue region of the visible spectrum in agreement with the bulk material presented in Figure 4.9(a).

The unannealed $LiAlO_2$:Fe nanoparticles excited by ultraviolet radiation (or blue light) emit light in the 700-800 nm wavelength range with the emission maximum at ~747 nm, as shown in Figure 4.13(b) again in agreement with the bulk material presented in Figure 4.9(b). Quantum confinement effects in nanomaterials usually manifest for particles in the size range from 2 to 6 nm and would not be expected for the nanoparticles in this work (with the size around 20 nm as previously reported) [212] [213] [214].

After annealing when the particle sizes increased to ~100 nm both the excitation spectrum (Figure 4.14(a)) and the emission spectrum (Figure 4.14(b)) became markedly more intense. The annealing resulted in a change in the photoluminescent properties of the phosphor which now absorbs significantly more ultraviolet radiation and re-emits the energy at longer wavelengths. The spectra is very similar to that of the $LiAlO_2$:Fe bulk phosphor shown in Figure 4.9.

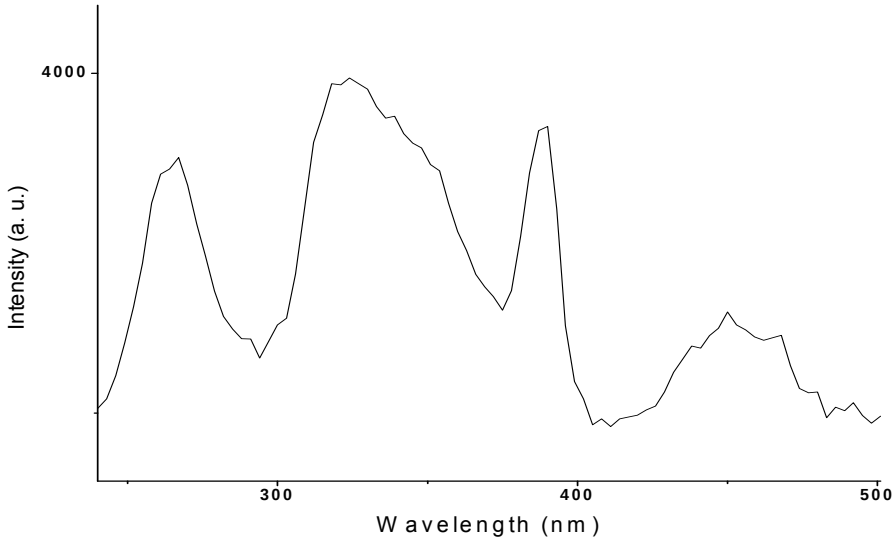

(a)

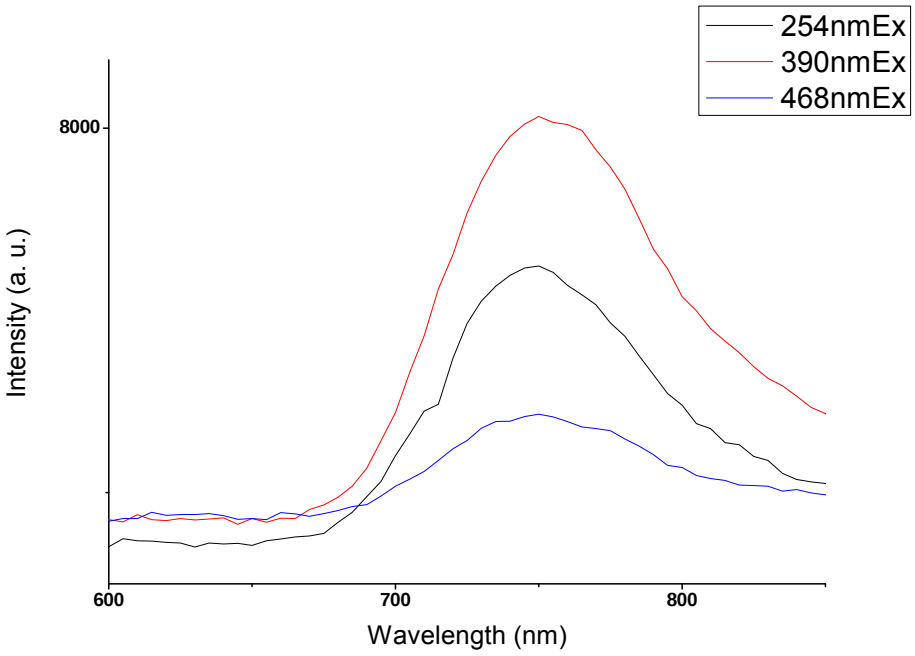

(b)

Figure 4.13 The $LiAlO_2$:Fe nanoparticles before annealing: (a) Photoluminescence excitation spectrum, monitored at 740 nm; and (b) Photoluminescence emission spectra under 254 nm, 390 nm and 468 nm excitation.

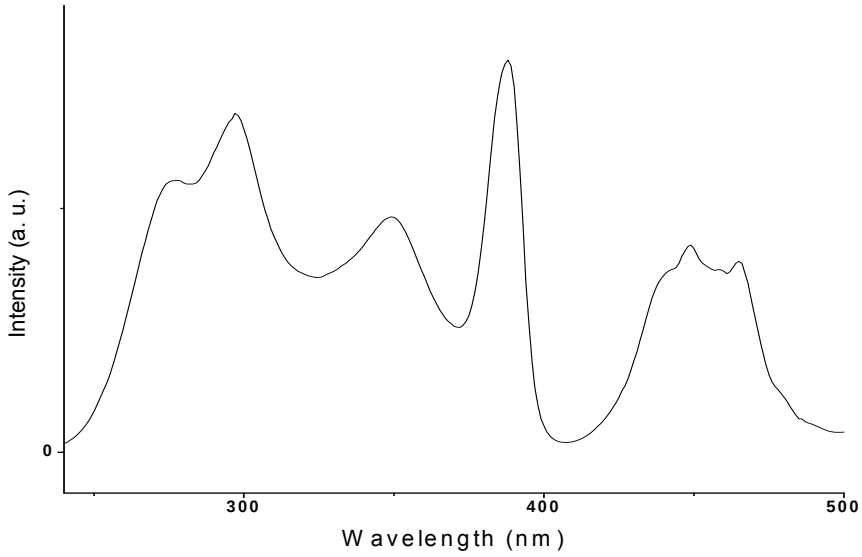

(a)

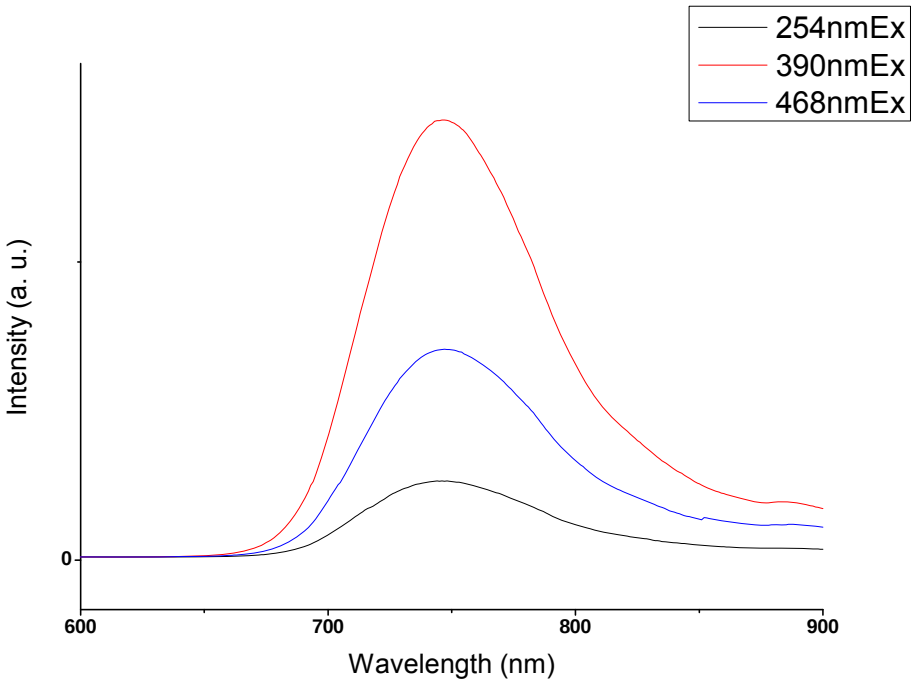

(b)

Figure 4.14 The $LiAlO_2$:Fe nanoparticles after annealing: (a) Photoluminescence excitation spectrum monitored at 740nm, and (b) Photoluminescence emission spectra, at 254 nm, 390 nm and 468 nm excitation wavelengths.

4.4 Polypropylene – $LiAlO_2$:Fe nanocomposite formation and characterisation

The annealed $LiAlO_2$:Fe nanophosphor was incorporated into polypropylene using the co-rotating twin screw extrusion method (see section 2.9) at a loading concentration of 2% in weight in order to make PP – $LiAlO_2$:Fe nanocomposite films. In the SEM micrograph presented in Figure 4.15, the dispersed particles of the phosphor can be clearly observed. Some agglomerates can also be seen.

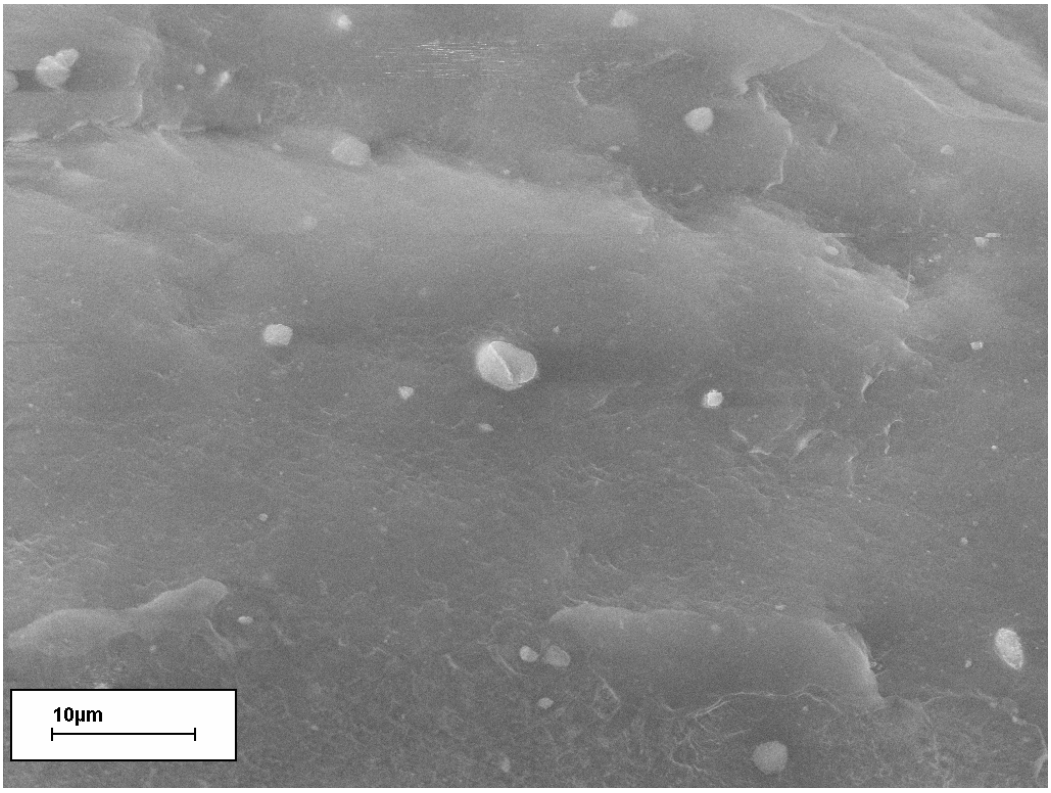

Figure 4.15 SEM image of polypropylene incorporating the $LiAlO_2$:Fe nanoparticles (after annealing at 650˚C), scale bar 10µm.

The excitation spectrum of the annealed phosphor incorporated in the polypropylene (Figure 4.16(a)) shows that the polypropylene does not inhibit the absorption of ultraviolet light by the phosphor; nor does the

polypropylene affect the emission of the absorbed energy in the near infrared region of the spectrum (see Figure 4.16(b)). However from the difference in the relative intensities of the excitation bands in Figure 4.14(a) and Figure 4.16(a) which are re-plotted and compared in Figure 4.17, it is obvious that the polypropylene is modulating the UV (probably by absorbing some of the UV wavelengths preferentially) as the radiation passes through the polypropylene matrix. Figure 4.18(a) presents a plot of the transmittance of polypropylene against wavelength and it confirms the absorption properties are not linear and are greater at shorter wavelengths, as expected, from the excitation spectra comparison shown in Figure 4.17. The emission spectrum shown in Figure 4.16(b) indicates that the $LiAlO_2$:Fe phosphor particles embedded in the polypropylene are being excited by the UV and blue wavelengths and convert this excitation to emission in the infra-red. The emission spectrum of the pure polypropylene was also investigated and the result showed that the pure polypropylene did not manifest any emission. This means that the polypropylene does not contribute to the emission in Figure 4.16(b) but only the embedded $LiAlO_2$:Fe phosphor does so.

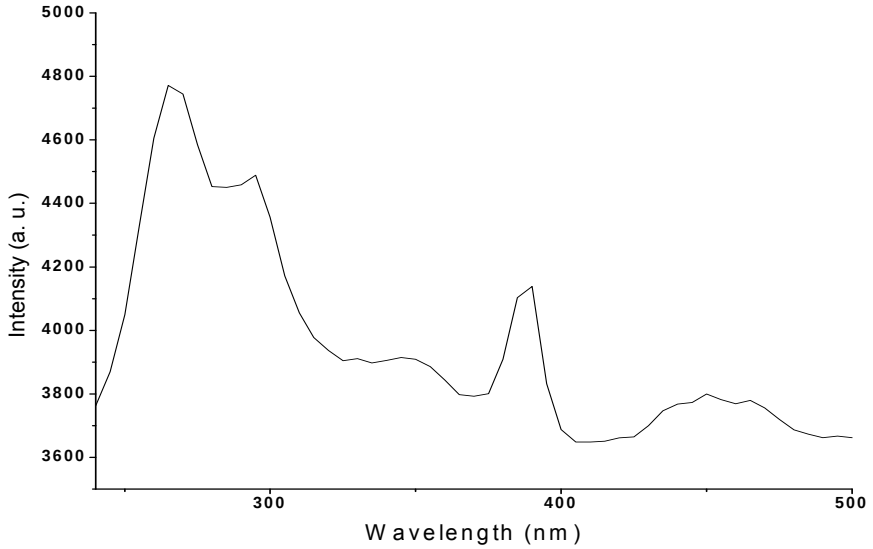

(a)

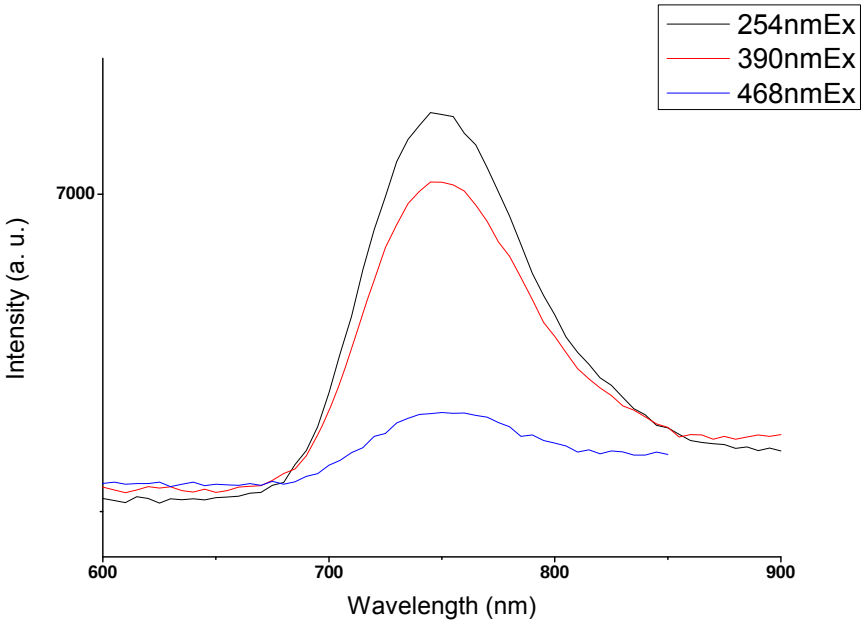

(b)

Figure 4.16 The annealed $LiAlO_2$:Fe nanoparticles incorporated into PP: (a) Excitation spectrum monitored at 740 nm, and (b) Emission spectra, under 254 nm, 390 nm and 468 nm excitation.

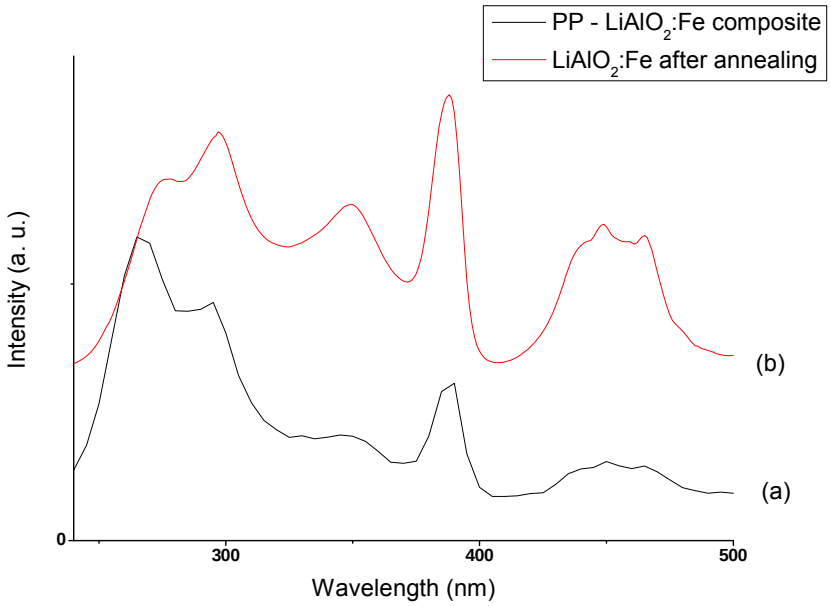

Figure 4.17 Excitation spectra comparison of (a) the PP – annealed $LiAlO_2$:Fe composite film and (b) the annealed $LiAlO_2$:Fe nanophosphor

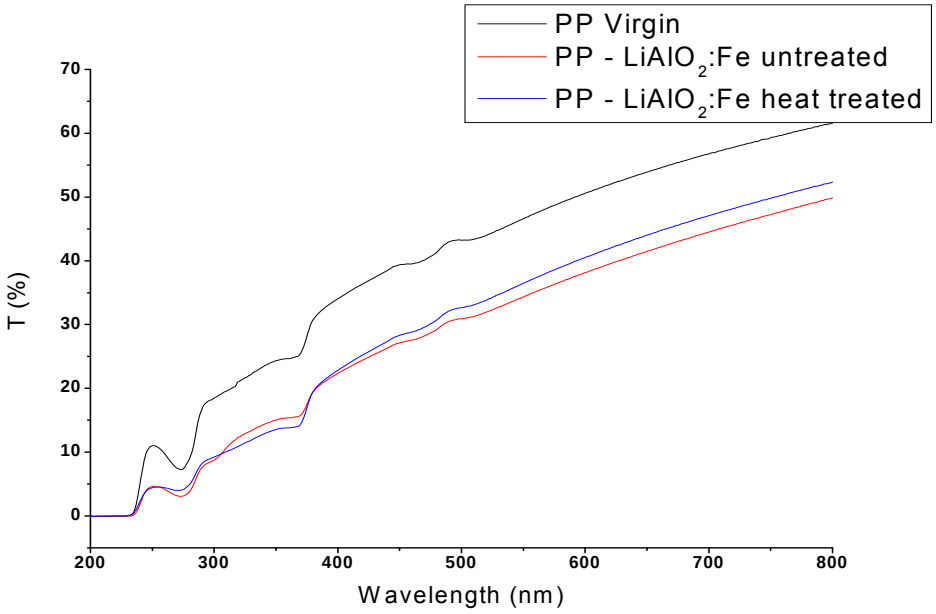

(a)

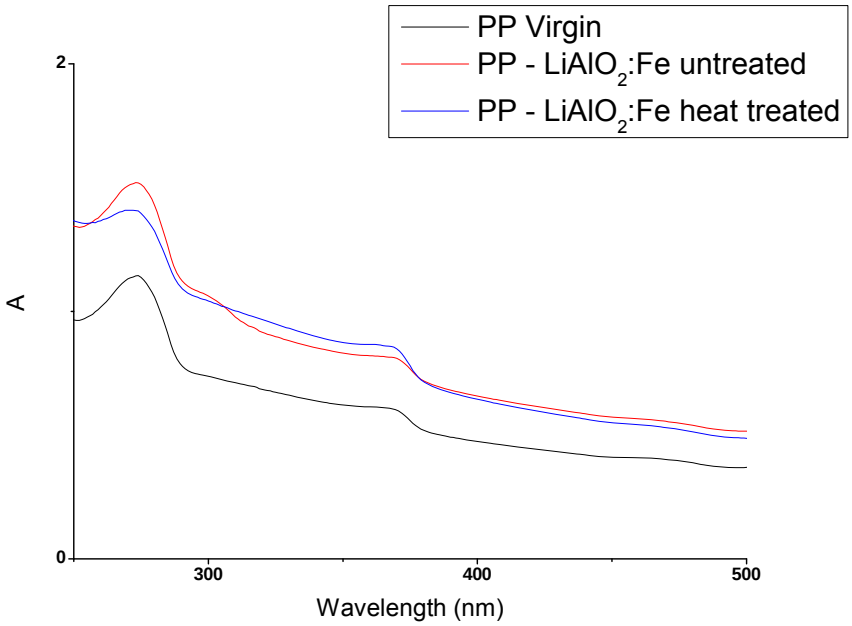

(b)

Figure 4.18 The UV/visible (a) transmission spectrum and (b) absorption spectrum of the polypropylene composite films as a function of wavelength

From Figure 4.18(a), it is obvious that incorporating the $LiAlO_2$:Fe nanophosphors decreases the transmittance of the polypropylene in the visible light region of the electromagnetic spectrum. This is because the embedded nanoparticles were agglomerated during the extrusion process to form lager particles. The evidence of those agglomerates was observed in the SEM image presented in Figure 4.15. These large agglomerates to some extent reflect and scatter the incident light, thus deteriorating the transmittance of the film. However, the absorption in the UV region increases due to the absorption and excitation characteristic of the phosphor (see Figure 4.18(b)).

Clearly the $LiAlO_2$:Fe phosphor particles are able to absorb incoming UV and blue wavelength light and convert it to harmless infra-red light, thus preventing polymer degradation. In addition this infra-red light can be used to stimulate plant growth (by keeping the plants warm and accelerating the plant photosynthesis) if this polypropylene nanocomposite is used to cover plants in fields and green houses. The $LiAlO_2$:Fe phosphor incorporated into polypropylene can also be used to maintain the temperature of anything else it covers above the ambient temperatures during daylight by downconverting UV and visible light.

4.5 Conclusions

From this work a number of conclusions are apparent:-

1. The morphology and crystal structure of the nanoparticle $LiAlO_2$:Fe before and after annealing were well characterised.
2. Annealing the nanoparticle $LiAlO_2$:Fe improved both the crystallinity and the photoluminescent excitation and emission properties of the phosphor.
3. The annealed $LiAlO_2$:Fe phosphor particles were successfully incorporated into polypropylene.
4. The excitation spectrum of the successfully incorporated $LiAlO_2$:Fe phosphor particles in polypropylene was modified by the presence of the polymer showing some UV and visible light had been absorbed by the polymer.
5. The fact that an excitation spectrum was observed of the $LiAlO_2$:Fe phosphor particles in the polymer shows that the concept of protecting the polymer from UV degradation with phosphors is feasible.
6. The fact that the $LiAlO_2$:Fe phosphor particles embedded in the polypropylene emit light in the infra-red again shows the concept of protecting the polymer from UV by down-converting the radiation with this phosphor works.
7. The fact that the $LiAlO_2$:Fe phosphor particles embedded in the polymer emit light in the infra-red shows that this material could be used to increase the temperature of whatever it covers relative to the background temperature.
8. The fact that the $LiAlO_2$:Fe phosphor particles embedded in the phosphor emit light in the infra-red shows that this material could be used to warm growing plants in cold fields during daylight.

Chapter 5 Investigation of Zinc Oxide Nanoparticles and Its Behaviour in Composites

5.1 Introduction

Zinc oxide (ZnO) is one of the most well-known II – VI compound semiconductors. Its pure crystal form can rarely be found in zincite on the earth as the mineral normally contains impurities (most probably manganese and iron) which in fact determine its colour. [215]

Recently, zinc oxide has attracted widespread interest and has been rapidly developed to exploit its unique properties:- 1) it has a wide band gap of 3.37 eV at room temperature; 2) it has a large bond strength; and 3) it has a large exciton binding energy of 60 meV [215] [216]. ZnO therefore has become an important industrial material and it has found applications in:- chemical sensors [217], thin film photovoltaic solar cells [218] [219], varistors [220], luminescent devices [221], catalysts [222] and cosmetics [223] [224] [225]. Nanoparticles (NPs) of this material have been the subject of wide interest in the last two decades, and since their successful commercial scale up for mass production [226] they have found applications in many different areas in the modern world, including as starting materials for some of the electronic applications listed above. In addition, they have found uses in transparent UV protection in sunscreen formulations [227] and they also show promise for use in food packaging applications for their antimicrobial activity [228].

Zinc oxide has been observed to have a considerable structural diversity based on its diversified morphology. It may well be that zinc

oxide has the greatest range of nanostructures found as yet among all metal oxides [229] [230] [231] [232]. Zinc oxide crystals in the light of different experimental conditions can crystallise in the form of nanospheres [233], nanorods [234], nanowires [235] [236], nanotubes [237], nanobelts [238], and in other complicated morphologies [239]. In addition zinc oxide crystals can be easily grown through a variety of synthetic methods including so-gel deposition [240] [241], thermal evaporation [242] [243], electrochemical deposition [244] [245], chemical vapour deposition (CVD) and cyclic feeding CVD [246], hydrothermal and solvothermal growth [247] [248] [249], and surfactant and capping agents-assisted growth [250].

In most cases zinc oxide has a hexagonal wurtzite crystal structure as it is its most stable phase [215] [216]. This structure belongs to the space group $P6_3mc$ and can be described by two lattice parameters:- *a* for the hexagonal edge length ranging from 3.2475 Å to 3.2501 Å and *c* for the height ranging from 5.2042 Å to 5.2075 Å [251] [252] [253]. A schematic diagram of the ZnO unit cell is presented in Figure 5.1. It can be seen that one zinc atom is coordinated with four oxygen atoms in a tetrahedral arrangement, and vice versa.

In the hexagonal wurtzite structure the morphology of the ZnO crystals manifest four most common crystal planes that include two polar ones, zinc terminated (0001) and oxygen terminated $(000\bar{1})$, as well as two non-polar $(2\bar{1}\bar{1}0)$ and $(01\bar{1}0)$ ones where the number of zinc atoms is equal to that of oxygen atoms. The various morphologies of the ZnO crystals mentioned above are in fact due to the differences in the growth rates of these crystal planes under different experimental conditions and hence the crystals preferentially grow along one of these planes [254] [255] [256].

In this chapter, ZnO nanoparticles prepared by the flame spray pyrolysis (see section 2.3) are fully characterised on the basis of their

crystal structure, morphology, as well as by reflectance and absorption characteristics.

Three methods including co-rotating twin screw extrusion, spin coating and solvent casting are employed to incorporate ZnO nanoparticles into polymers to make polymer nanocomposite films. The dispersion of the nanoparticles into these films are examined and compared in terms of different preparation methods in this chapter. In addition the optical properties of these films are also investigated.

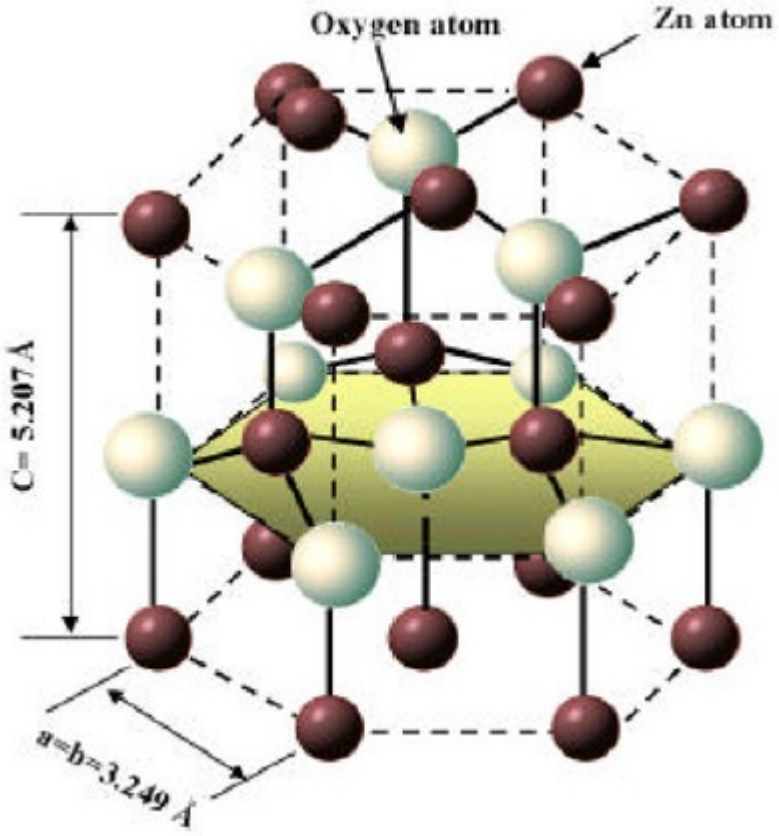

Figure 5.1 A schematic diagram of the ZnO hexagonal unit cell. The large white spheres represent the oxygen atoms while the small brown spheres represent the zinc atoms. **[216]**

5.2 ZnO nanoparticles characterisation and properties

Zinc oxide nanoparticles were synthesized by flame spray pyrolysis. The crystal structure of the nanoparticles were characterised by X-ray diffraction and the data are shown in Figure 5.2. It was shown that the nanoparticles crystallise in a wurtzite hexagonal structure with lattice parameters of a = 3.2526(1) Å and c = 5.2141(2) Å. The crystallite size of the as-prepared ZnO was observed to be 19.3(1) nm. No evidence for impurities or other phases was found in the diffractogram. The cell size of these nanoparticles is larger than those reported in the introduction for the bulk material (with 'a' ranging from 3.2475 to 3.2501 Å and 'c' ranging from 5.2042 to 5.2075 Å) [216] [253] and this finding is common behaviour for nanoparticles of a material. This is probably due to differences in the long range order of zinc and oxygen atoms between a bulk material and a nanosized one. It may be also due to a large number of oxygen vacancies, vacancy clusters and local lattice disorders present in the particle surface where either the exposed Zn^{2+} or the O vacancies contribute to the lattice expansion in the case that the particle size decreases down to the nanometre size [257] [258].

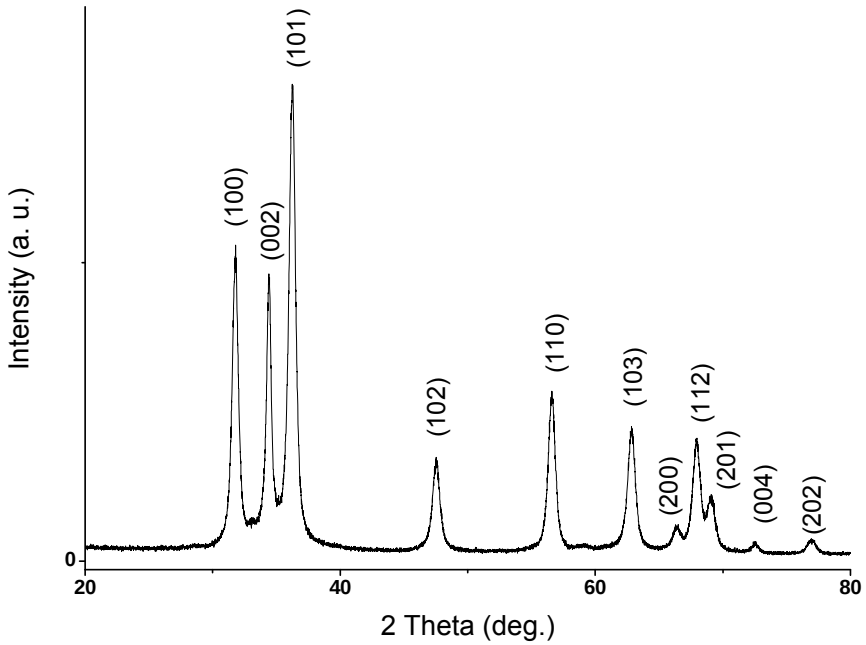

Figure 5.2 Powder X-ray diffractograms of the as-prepared zinc oxide nanoparticles

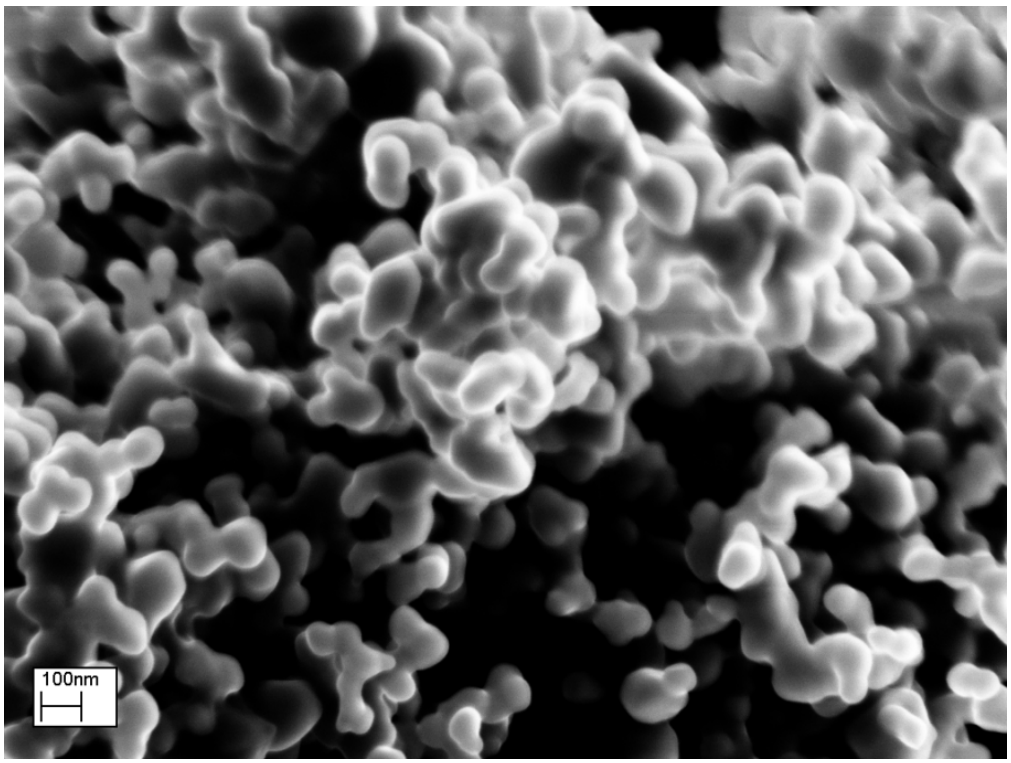

Figure 5.3 SEM image of as-prepared zinc oxide nanoparticles

As seen in the SEM image (Figure 5.3), the ZnO nanoparticles prepared via the flame spray pyrolysis have sphere-like morphologies with ultra-smooth surfaces. The image also shows that the ZnO consists of ultra-small and ultra-uniform nanoparticles sized around 50 nm.

Figure 5.4 presents the Raman spectrum of the ZnO nanoparticles in the range of 200 – 700 cm^{-1}. The spectrum exhibits two small bands at 333 cm^{-1} and 381 cm^{-1} as well as a sharp main peak at 438 cm^{-1}. This is evidence that the ZnO nanoparticles crystallise in the wurtzite hexagonal structure [259]. The relatively weak intensity of the Raman bands and the background noise are due to the small crystal size and ultra-small particle size (nano-sized) of the ZnO.

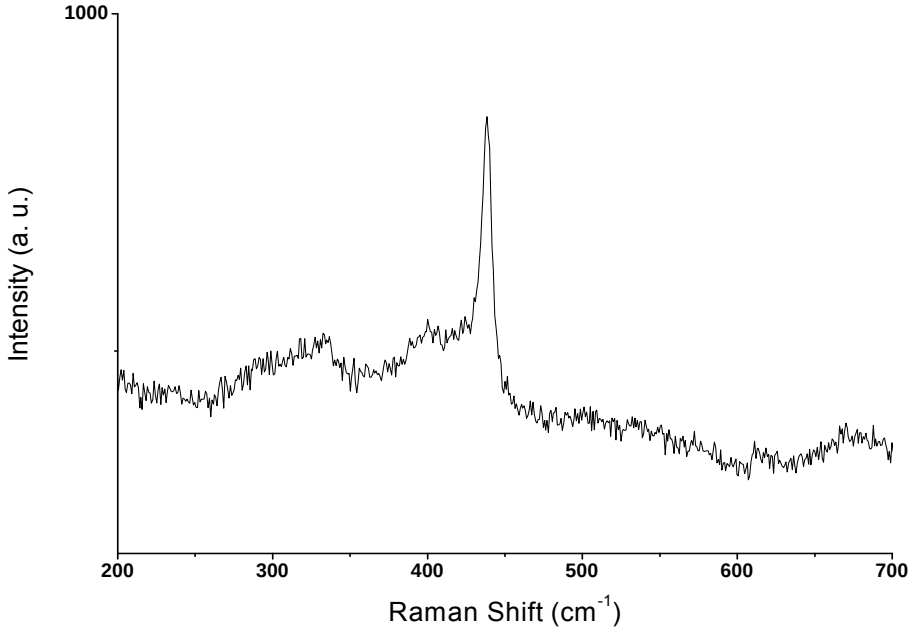

Figure 5.4 Raman spectrum of as-prepared zinc oxide nanoparticles

The UV-Visible light reflectance and absorption spectrum of the ZnO nanoparticle dry powders are presented in Figure 5.5. From around 400 to 800 nm, the ZnO powders reflect most of the light in the visible region of the electromagnetic spectrum, whereas below 400 to 200 nm

they strongly absorb the UV light. The steep cut-off at 400 nm on the spectrum indicates that the ZnO can be used as a smart material when encapsulated in the polymer only absorbing the UV light which is harmful to polymer, but reflecting or transmitting the useful visible light.

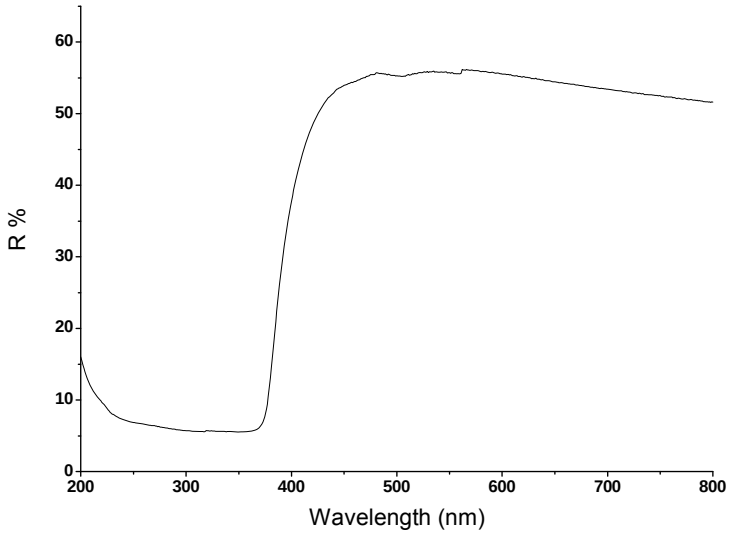

(a)

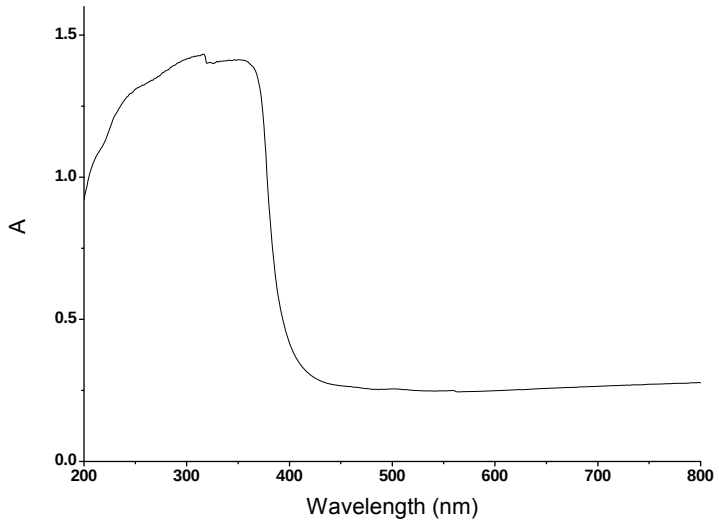

(b)

Figure 5.5 (a) Reflectance spectrum and (b) absorption spectrum of the as-prepared zinc oxide nanoparticle dry powders

5.3 Polypropylene – ZnO nanocomposite formation via the extrusion technique

The ZnO nanoparticles were incorporated into a polypropylene matrix using a co-rotating twin screw extrusion method (see Figure 5.6). The composites were extruded and collected in the form of thin films at the different loading concentrations of 2%, 5% and 10% in weight (see section 2.10).

Figure 5.6 Sheet extrusion and collection of the PP – ZnO nanocomposites

The transmittance and absorption characteristics of the extruded PP – ZnO nanocomposites are shown in Figure 5.7. The plots disclose that the virgin polypropylene film has good transparency in the visible region of the electromagnetic spectrum and does not absorb too much UV, i.e. it still shows relatively good transparency in the UV light region of the electromagnetic spectrum.

However, the absorption spectra (see Figure 5.7(b)) manifest a dramatic absorption increase from 400 down to 200 nm when incorporating the ZnO nanoparticles into the polypropylene. This indicates that the embedded ZnO nanoparticles still display some of their original properties in the matrix.

On the other hand, the transmittance spectra decrease significantly in the region of the visible light with the increasing loading concentrations of the ZnO nanofillers. The PP – ZnO sheet composite becomes translucent if incorporated with 2wt% of the ZnO nanofillers. Only 20% - 30% visible light passes through it. When incorporating more ZnO nanofillers into the polypropylene, (in the condition of 5wt% and 10wt% of the ZnO nanoparticles) the sheet composites become totally opaque and little visible light can pass through.

The reason is again mainly due to the agglomeration of the ZnO nanoparticles present in the polypropylene matrix. It is well known that when the particle size decreases down to a nanoscale, the surface area to volume ratio becomes too large to be neglected. The significantly large surface area makes a great proportion of the electrons exposed to the surface, leading to a high surface energy and great inter-particulate forces that activate surface chemistry, thus in turn leading to a strong tendency to form particle agglomeration.

In this work, before feeding the raw materials into the extruder, a physical mixing of the ZnO nanoparticles and the polypropylene pellets was conducted and this in fact could not uniformly distribute the nanoparticles and eliminate the agglomerates. Although the co-rotating

twin screw extruder provides large shear stress and good thermal mixing, it still cannot fully distribute the nanoparticles. The surviving ZnO agglomerates settle in the polypropylene matrix (see SEM images in Figures 5.8, 5.9 & 5.10), reflecting and scattering any incident light thereby deteriorating the transmittance of the composite.

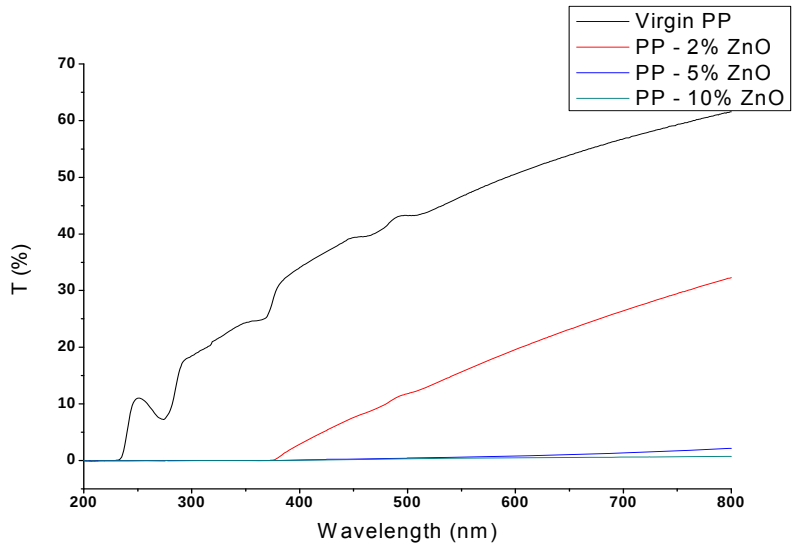

(a)

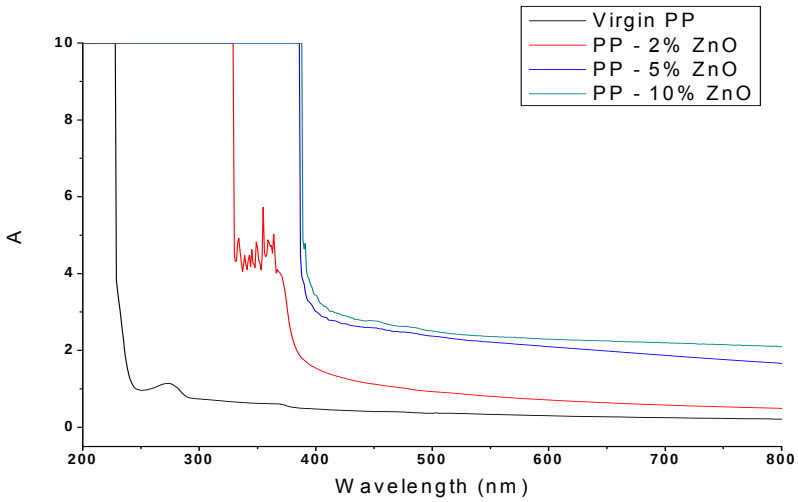

(b)

Figure 5.7 (a) Transmittance spectrum and (b) absorption spectrum of the PP-ZnO sheet composites

(a)

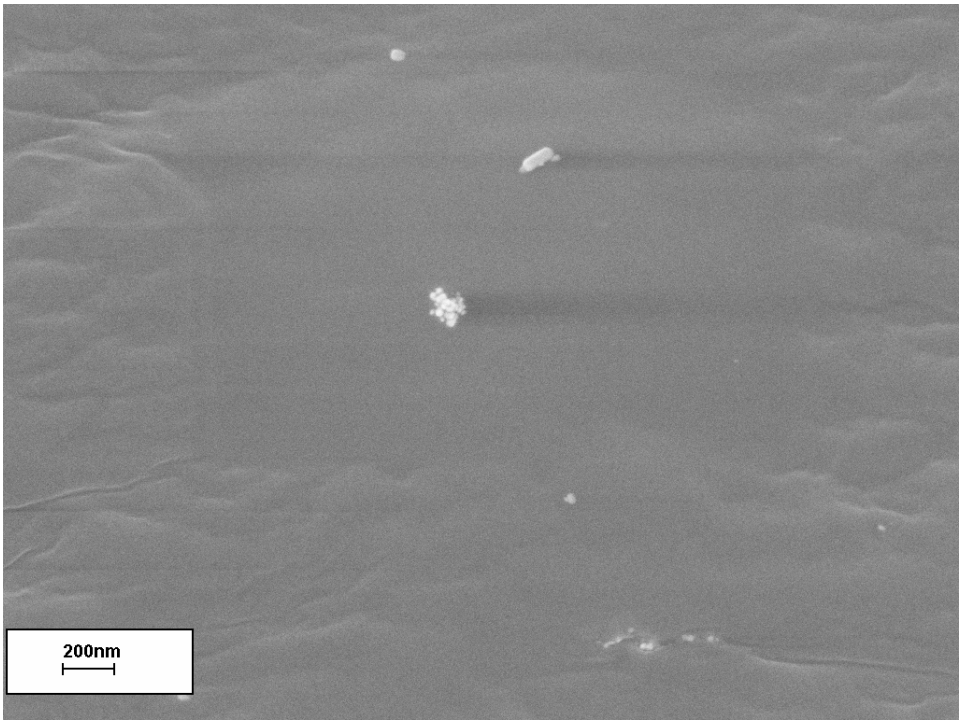

(b)

Figure 5.8 SEM images of the PP – 2wt% ZnO composite prepared via the extrusion technique (a) area 1; (b) area 2

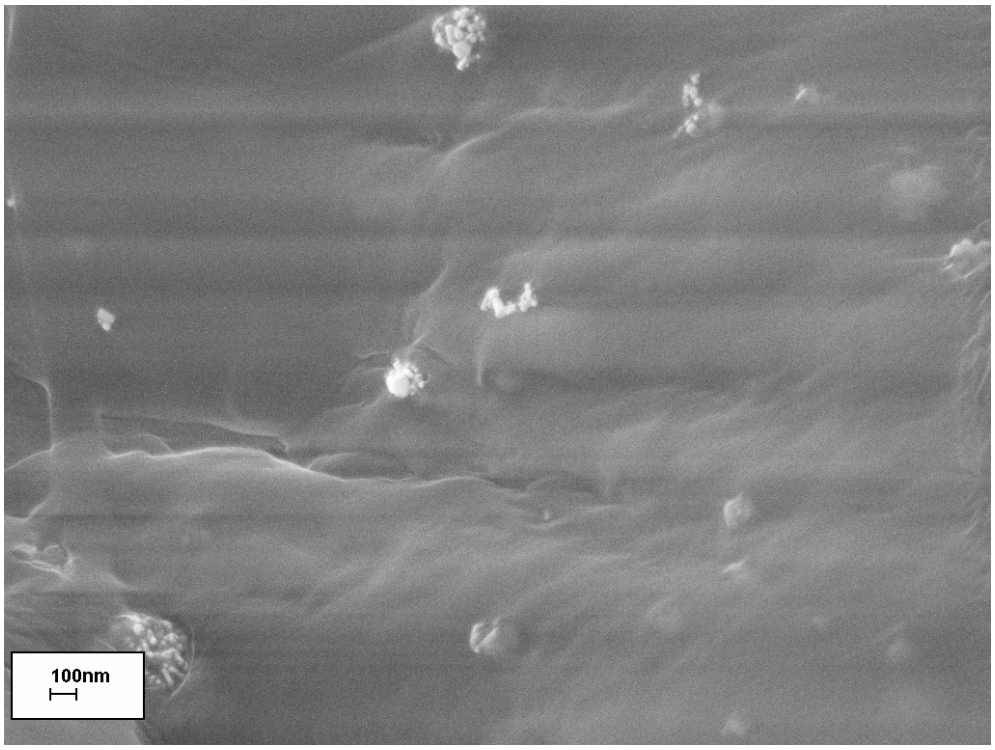

(a)

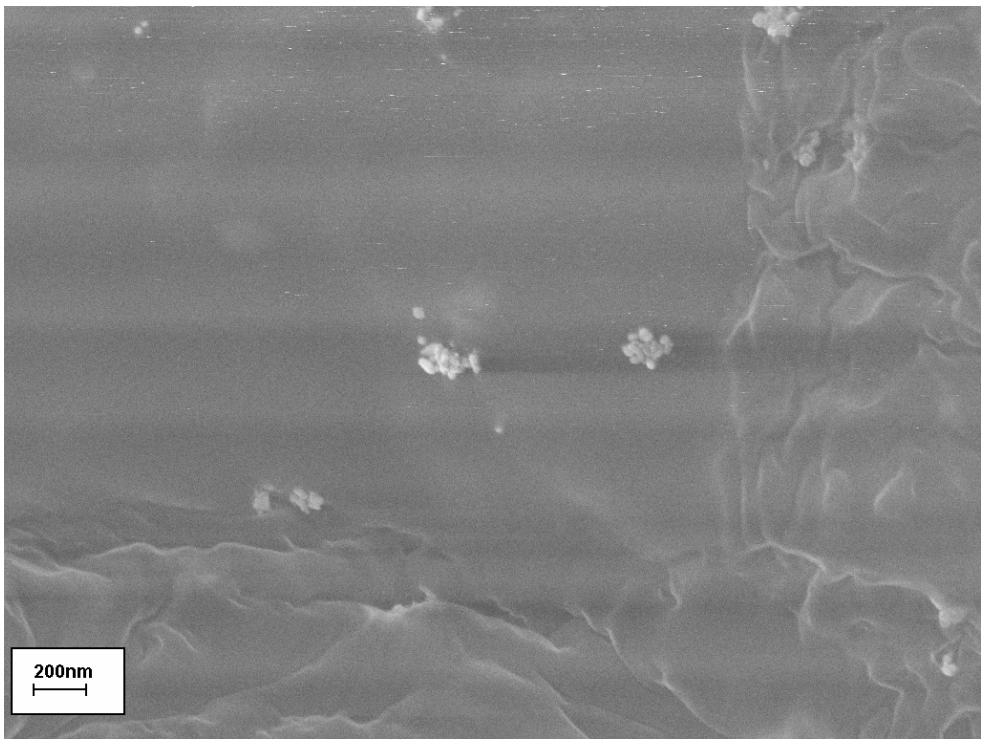

(b)

Figure 5.9 SEM images of the PP – 5wt% ZnO composite prepared via the extrusion technique (a) area 1; (b) area 2

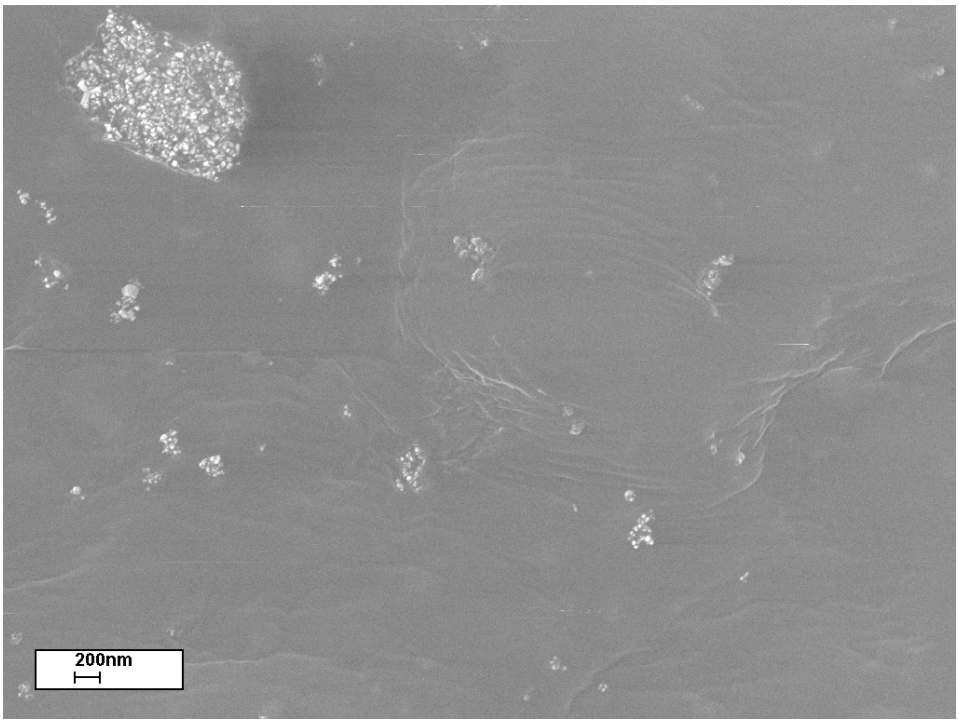

(a)

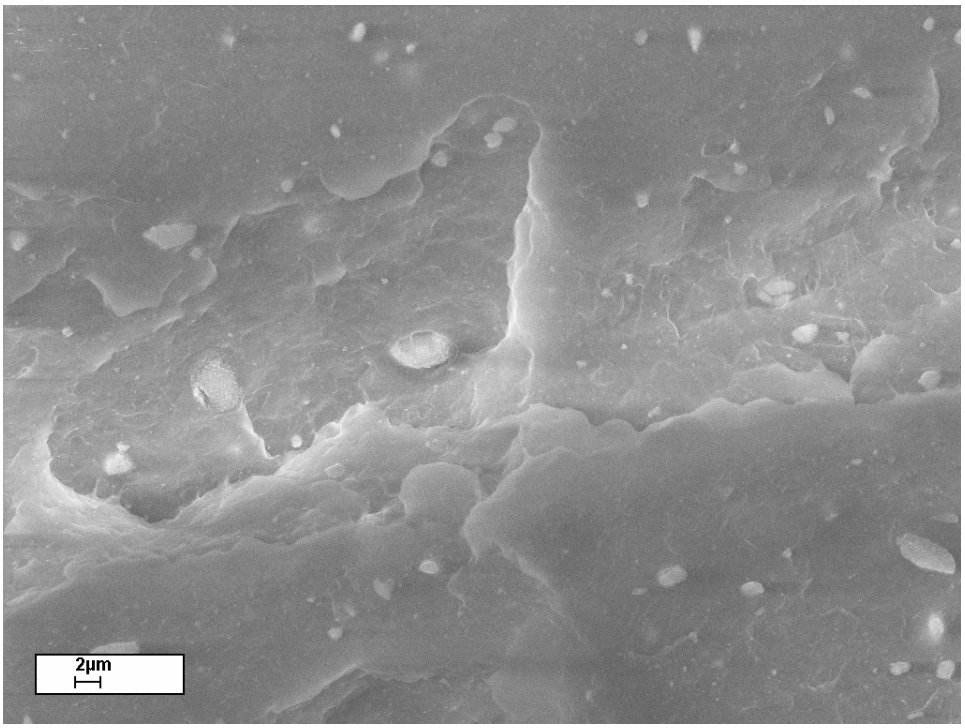

(b)

Figure 5.10 SEM images of the PP – 10wt% ZnO composite prepared via the extrusion technique (a) area 1 with high magnification; (b) area 2 with low magnification

SEM images of the PP – ZnO nanocomposites at the various loading concentrations are shown in Figures 5.8, 5.9 and 5.10. It can be seen that the extrusion thermal processing does not change the morphology of the ZnO nanoparticles (sphere-like shape). Several agglomerates are shown on the images, though the nanoparticles were well distributed into the polypropylene matrix via the extrusion. It also can be noticed that with the increasing filler concentrations, the size of agglomerates increases correspondingly, showing 100 nm in 2% of fillers, 200 nm in 5% of fillers and 1 – 2 μm in 10% of fillers.

5.4 Polystyrene – ZnO nanocomposite formation via the spin coating technique

In the previous sections (sections 4.4 and 5.3), it was reported that although the co-rotating twin screw extrusion is a fast and simple method to manufacture polymer nanocomposites in various artificial shapes, it is not an ideal technique to distribute nanoparticles into a polymer matrix due to the observed agglomerates. A new attempt was therefore conducted to address this drawback and expectantly achieve better distribution of the zinc oxide nanoparticles into the polymer matrix.

1wt% of the ZnO nanoparticles were incorporated into a polystyrene matrix using a spin coating technique to make ultra-thin films (see section 2.11). The distribution of the ZnO nanoparticles is presented in SEM images in Figure 5.11. It is obvious that the ZnO nanoparticles with sphere-like morphology were very uniformly dispersed in the polystyrene matrix. No agglomerates can be seen in the images which show much better distribution of the ZnO nanoparticles compared with that of the PP – ZnO extruded composite films (see Figures 5.8, 5.9 & 5.10)

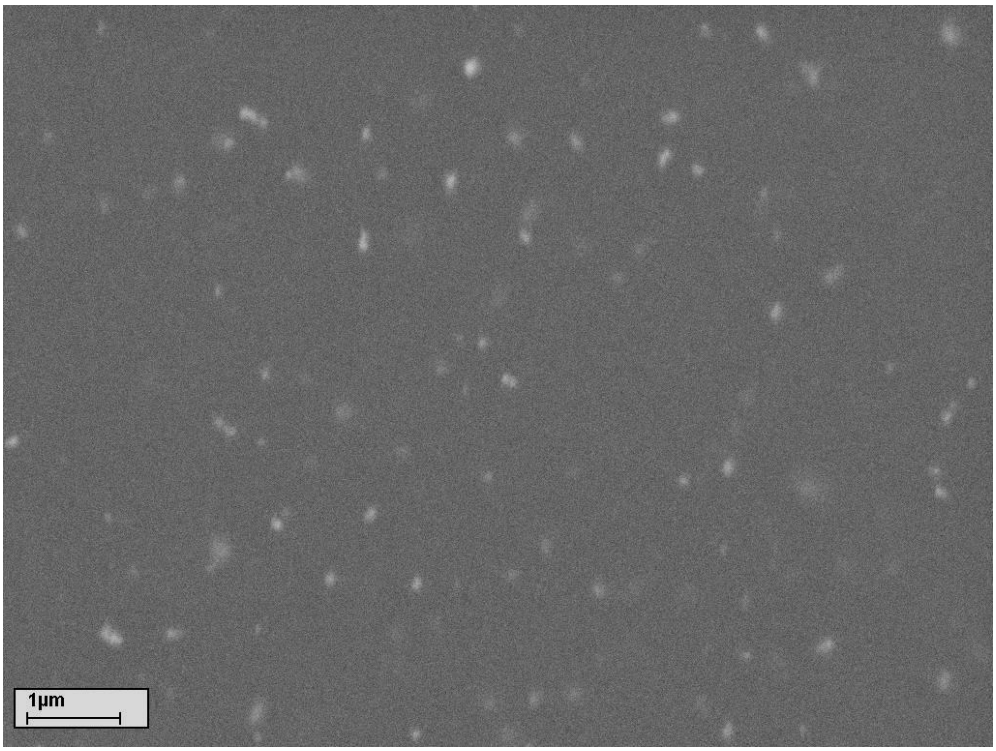

(a)

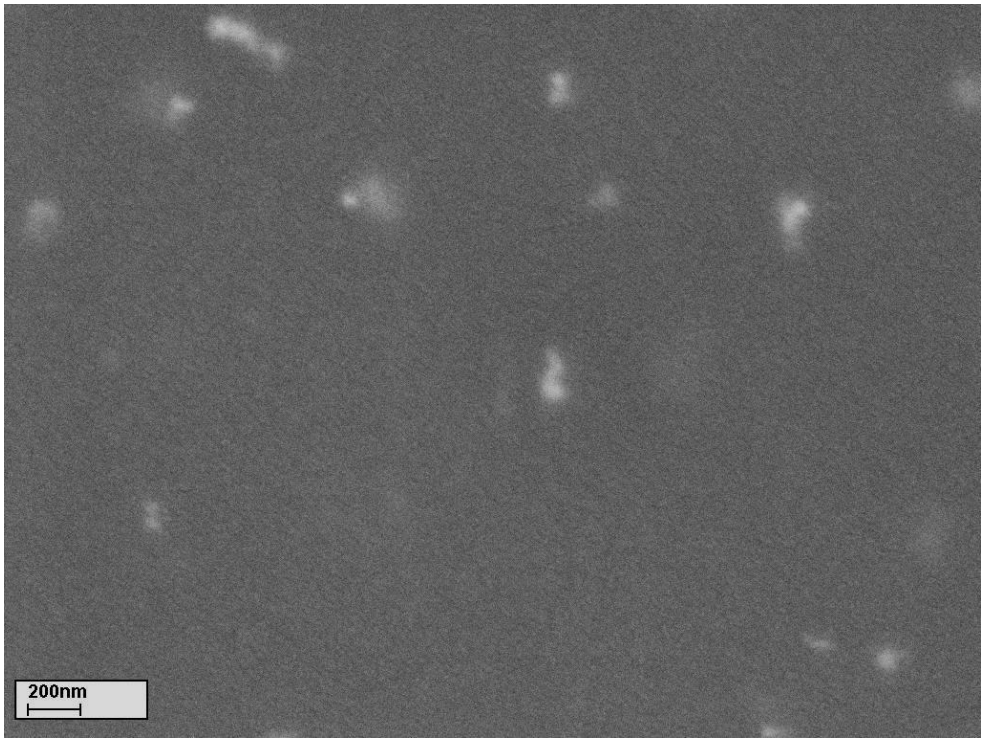

(b)

Figure 5.11 SEM images of the PS – 1wt% ZnO composite via the spin coating technique (a) low magnification; (b) high magnification

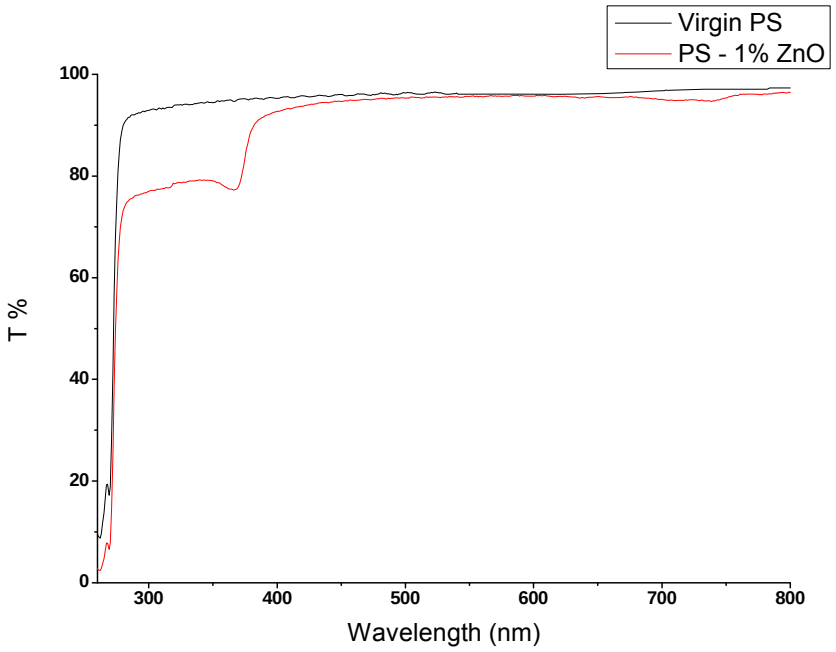

(a)

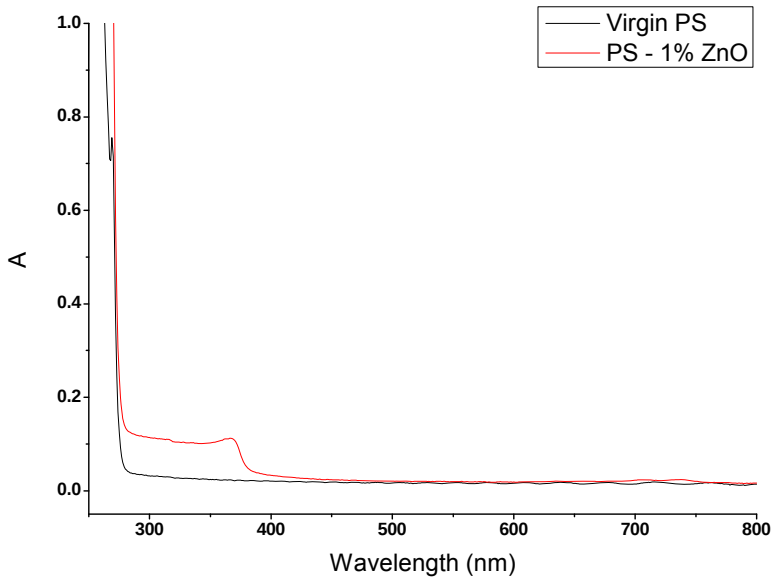

(b)

Figure 5.12 (a) Transmittance spectrum and (b) absorption spectrum of the PS – 1% ZnO composite via the spin coating technique

Figure 5.12 presents the transmittance spectrum and absorption spectrum of the PS – 1wt% ZnO nanocomposite. The virgin polystyrene film has extremely high transmittance of 96%. However, incorporating the ZnO nanoparticles does not reduce any transparency of the composite in the range of the visible light compared with that of the virgin polystyrene, but significantly absorbs the UV light which is in the region below 400 nm wavelength.

This considerable improvement is due to very even dispersion of the ZnO nanoparticles into the polystyrene matrix. Before conducting the spin coating process, an ultrasonication process was employed in order to make a well dispersed PS – ZnO suspension. The ultrasound was applied to provide abundant energy to agitate the nanoparticles at a high frequency so that the links and bonds between the nanoparticles could be thoroughly disrupted, thus preventing the agglomeration. In addition, the concentration of the polystyrene solution was adjusted accurately to achieve a desired viscosity to stabilize the nanoparticles in solution in a well suspended state. The polystyrene solution was neither too thick to cause the nanoparticles to aggregate nor too dilute to not keep them suspended, thus avoiding the deposition of the nanoparticles at the bottom of the solution and hence their further agglomeration. As long as the stable PS – ZnO suspension was achieved, the uniform film of PS – ZnO nanocomposite could be obtained by the spin coating technique. The latter technique provided a high angular speed and a simultaneous fast evaporating rate.

5.5 Polystyrene – ZnO nanocomposite formation via the solvent casting technique

A large step forward was achieved in the methodology of dispersion of the nanoparticles using the spin coating technique. However, this technique can only provide thin films (normally with the thickness of sub-microns or even below 100 nm) and it is further of limited use if thick films are required [260]. Another method was therefore adopted to produce thick PS – ZnO nanocomposite films with good nanoparticle distribution and high visible light transmittance.

To achieve thick composite films, 1wt% of the ZnO nanoparticles were embedded into the polystyrene matrix by a solvent casting technique (see section 2.11). The embedded distribution was examined and a SEM micrograph is displayed in Figure 5.13. Clearly, very even dispersion of the ZnO nanoparticles was attained via the solvent casting method. The nanoparticles were well dispersed and located in the polystyrene matrix, and few clusters could be observed.

Figure 5.14 presents transmittance and absorption spectra of the polystyrene composite film incorporated with 1wt% of the ZnO nanoparticles. From Figure 5.14 it can be seen that there is excellent transparency to the visible light as well as good absorption to the UV light, compared with the virgin polystyrene film. It is further demonstrated that very nice dispersion can also be achieved in thick films through using the ultrasonication and solvent casting technique. Good evidence for this is presented in Figure 5.15, where a transparency comparison of the polystyrene film with and without the incorporation of the ZnO nanoparticles is shown.

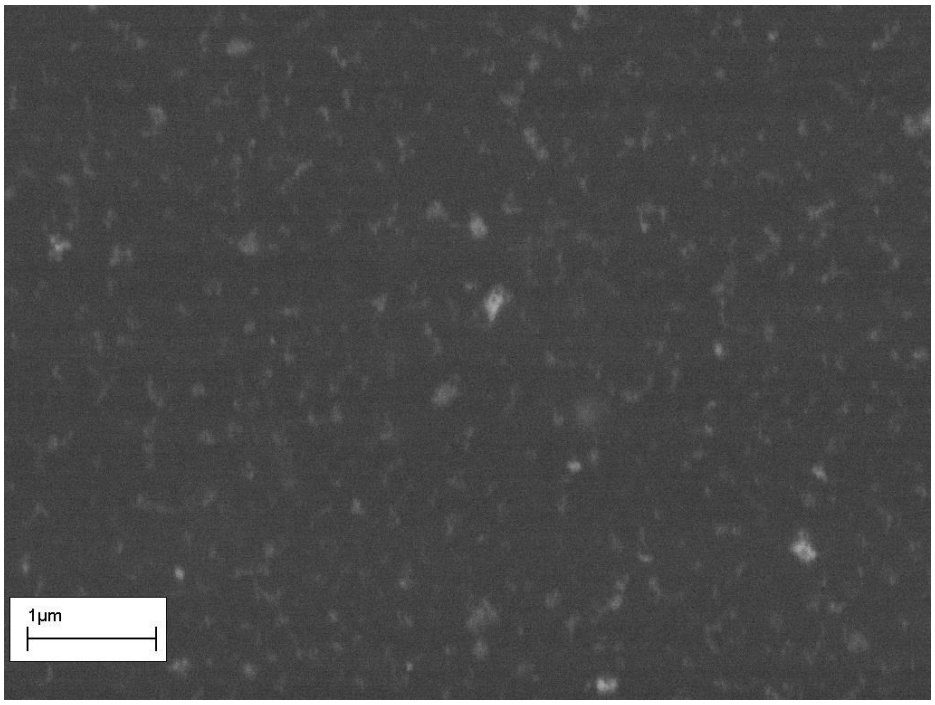

(a)

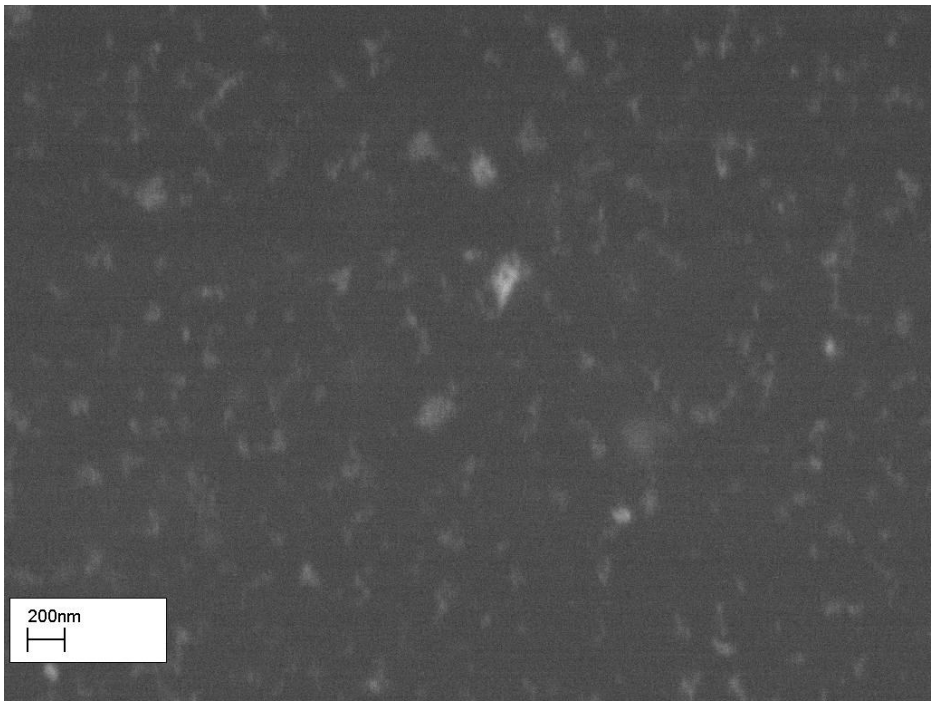

(b)

Figure 5.13 SEM images of the PS – 1wt% ZnO nanocomposite film prepared via the solvent casting method at (a) low magnification and (b) high magnification

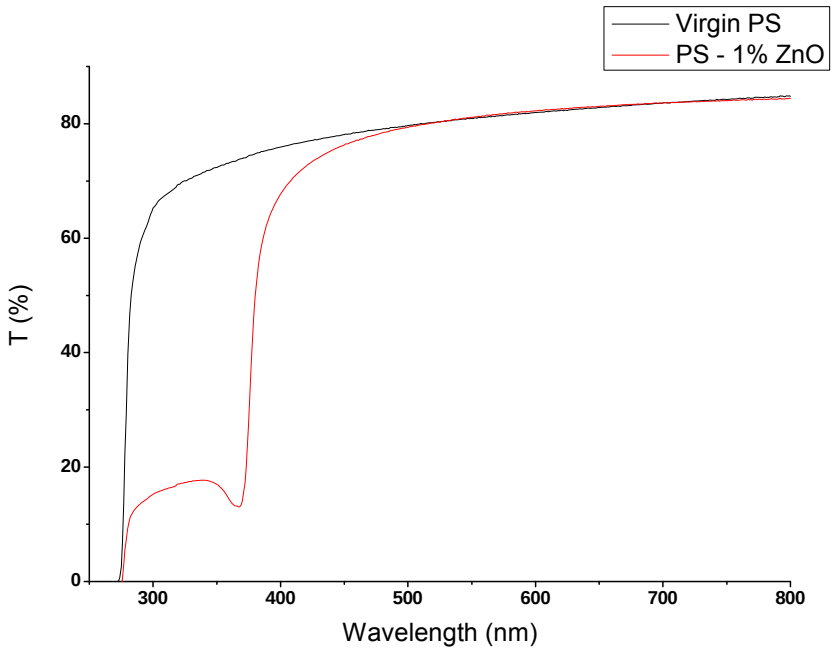

(a)

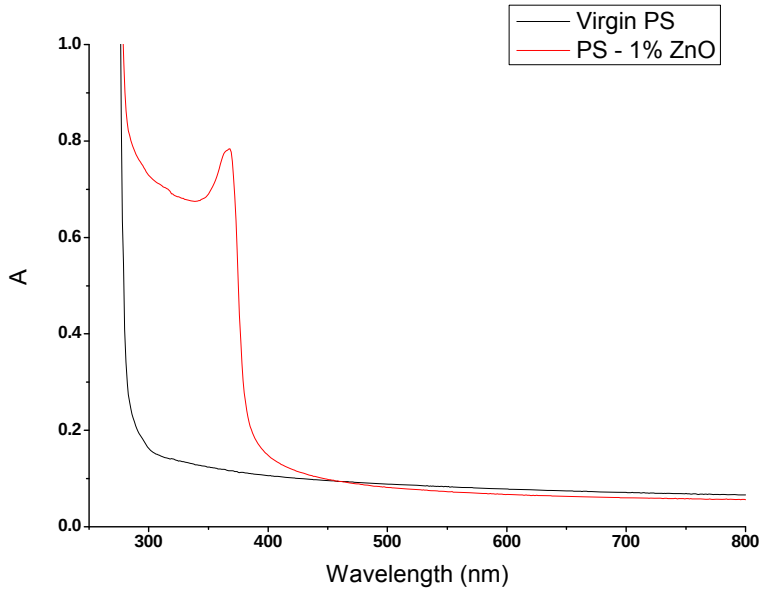

(b)

Figure 5.14 (a) Transmittance spectrum and (b) absorption spectrum of the PS – 1% ZnO composite film via the solvent casting technique.

(a) (b) (c)

Figure 5.15 Transparency comparison: (a) no cover; (b) covered with the virgin polystyrene film; (c) covered with the polystyrene film containing 1wt% of the ZnO nanoparticles

It is also worth to discuss here that there are some differences which cannot be neglected between Figure 5.12(a) and Figure 5.14(a), though both the figures present the transmittance spectra of the PS – 1wt% ZnO nanocomposite film. In the former it can be noticed that the composite has transmittance beyond 90% in the visible region and slightly decreases to 80% when the wavelength of the light resource goes below 400 nm. However the latter shows that the composite manifests around 80% transmittance to the visible light and it drops considerably to the value below 20% in the UV region. This different performance is due to the different composite formulation techniques which in turn lead to different thickness of the composite films. In Figure 5.12(a) the film is extremely thin (around 100 nm thickness), but the film shown in Figure 5.14 (a) has much higher thickness (around 0.8 millimetres). The result here is in great consistent with the Beer Lambert law explained in section 1.5.

5.6 Conclusions

From this work a number of conclusions can be made:-

1. The crystal structure and morphology of the ZnO nanoparticles were examined.
2. The ZnO nanoparticles were successfully incorporated and distributed into the polymers using the co-rotating twin screw extrusion, the spin coating and the solvent casting technique.
3. The extrusion technique was shown to lead to the poor dispersion of the ZnO nanoparticles, whereas the spin coating and the solvent casting technique provided the best uniform distribution of the nanoparticles.
4. The transparency of the extruded polypropylene composite film was significantly deteriorated with the incorporation of the ZnO nanoparticles which coalesced and aggregated to form large particles causing severe light blocking and scattering problems.
5. The transparency of the polystyrene composite films made by the spin coating and the solvent casting technique did not decrease with the introduction of the ZnO nanoparticles.
6. The fact that the ZnO nanoparticles embedded in the polymers absorb light in the UV region shows that this material could be used to protect the polymer from the UV radiation.

Chapter 6 Investigation of Luminescent Zinc Oxide Phosphor and Its Behaviour in Composite

6.1 Introduction

In the proceeding chapter the structure and some of the properties of zinc oxide were described. It is a semiconducting compound which crystallises in a wurtzite hexagonal structure [215]. Within this crystal structure, there is a large amount of space and a great number of voids that can accommodate interstitial atoms such as zinc interstitials or impurity atoms. In addition as zinc oxide crystals are not thermally stable, they can easily lose their oxygen atoms to form a non-stoichiometry structure which is referred to $ZnO_{(1-x)}$:Zn_x if they are heated (the value of x has a range from 0.04 to 0.6) [261] [262]. It is therefore difficult to prepare pure stoichiometric zinc oxide crystals. Instead these crystals normally appear with structural defects. Due to these, zinc oxide crystals can be used as n-type semiconducting materials.

In section 5.1, it was briefly explained that ZnO has distinctive properties including a wide electronic band gap (3.37 eV) and a large exciton binding energy (60 meV). These properties distinguish ZnO from other semiconductors such as gallium nitride (GaN) which is a main industrial competitor material to ZnO (with the band gap of 3.4 eV and the exciton binding energy of 21 – 25 meV) for applications in laser diodes and light emitting diodes. [263] [264].

Apart from those characteristics, the photoluminescent properties of the ZnO are also of great interest as it can be intentionally transformed into a non-stoichiometry form ZnO:Zn by a reducing process. The zinc

rich luminescent zinc oxide (ZnO:Zn) has two signature emission peaks, a sharp one centred around 380 nm (in the UV region) due to a near band edge emission and a broad one ranging from 450 to 550 nm (green emission) due to a deep defect level emission. It is well known that the origin of the UV emission is ascribed to the recombination/annihilation of free excitons but the mechanism behind the green luminescence is still under debate [265] [266] [267] [268] [269].

Several models have been proposed to understand the green emission of ZnO:Zn and these include:- oxygen vacancy (V_o) [270] [271] [272] [273] [274], oxygen antisite (O_{Zn}) [275], zinc vacancy (V_{Zn}) [276] [277] [278], zinc interstitial (Zn_i) [279], electronic transition from Zn_i to V_{Zn} [280], and extrinsic impurities [281] [282]. Among these, the oxygen vacancy is the most widely accepted mechanism to explain the green emission as it is the most common defect in zinc oxide crystals [283] [284]. The oxygen vacancy appears in three various charge states:- the neutral oxygen vacancy (V_o^0) which captures two electrons and does not show any charge to the lattice, the singly ionized oxygen vacancy ($V_0^\bullet$) which only captures one electron and shows a single positive charge, and the doubly ionized oxygen vacancy ($V_o^{\bullet\bullet}$) which does not trap any electron and is manifested by a doubly positive charge to the lattice. However, only the singly ionized $V_0^\bullet$ can act as a luminescent centre and this is responsible for the green emission of the ZnO:Zn. The electrons trapped by the singly ionized $V_0^\bullet$ recombine with the photo-excited holes in the valance band and hereby emit in the green wavelengths. It has been shown that the intensity of the green emission increases with the increasing density of the $V_0^\bullet$. [271] [272]

A number of research groups have incorporated ZnO into polymers since the work in this thesis was started however the patent [285] taken by Professors Silver and Withnall predates these works [1] [169] [170] [286] [287] [288]. Such polymer/ZnO nanocomposites have the properties of physical flexibility and are facile for processing. In

addition the polymer/ZnO nanocomposite is able to combine the advantages of both the polymer matrix and the ZnO.

Several groups have studied the degradation of polymers in the presence of ZnO nanoparticles but no others have tried to protect polymers with down converting ZnO:Zn [1] [169] [288] [289]. In this chapter studies on ZnO:Zn nanoparticles embedded in polystyrene films are reported. The zinc rich luminescent zinc oxide nanophosphor (ZnO:Zn) synthesised by following the procedures described in section 2.4 was investigated. The crystal structure and morphology of the nanophosphor were characterised by X-ray powder diffraction, Raman spectroscopy and Scanning Electron Microscopy. The UV absorption characteristics and down converting luminescent properties of both the ZnO:Zn nanophosphor itself and when embedded as a polymer composite are also reported. This work has been published at the Material Research Society 2012 Fall Meeting and its proceeding [290].

6.2 ZnO:Zn nanophosphors characterisation and properties

The zinc oxide nanoparticles made by the flame spray pyrolysis were heat treated at 800°C to form the zinc-rich luminescent zinc oxide (ZnO:Zn) nanophosphors. The processing details can be found in section 2.4. The crystal structure of as received ZnO nanoparticles (Figure 6.1(a)) and the ZnO:Zn nanophosphors (Figure 6.1(b)) were characterised using the X-Ray diffractogram. These reveal that the zinc and oxygen atoms are arranged in the wurtzite hexagonal structure. Compared with the as-prepared ZnO nanoparticles made by flame spray pyrolysis (see Figure 6.1(a)) their crystal information (fully discussed in section 5.2) was a = 3.2526(1) Å and c = 5.2141(2) Å, the lattice parameters of the ZnO:Zn nanophosphors reported here (after firing) are changed to a = 3.2531(1) Å and c = 5.2116(2) Å. Thus correspondingly there is a cell volume decrease from 47.772(3) $Å^3$ to 47.764(2) $Å^3$. This change in cell size is possibly due to the presence of oxygen vacancies and zinc atoms in interstitial sites, but more likely due to an increase in long range order as the particle sizes increase (the evidence for this is given in the following sentences). The crystallinity of the reduced zinc oxide (ZnO:Zn) particles was significantly improved as observed in the higher intensity and narrower width of the peaks as shown by the X-ray diffractogram (Figure 6.1(b)). The crystallite size of the ZnO:Zn is correspondingly observed to increase to 66.5(5) nm from 19.3(1) nm in the none reduced precursor reported in section 5.2.

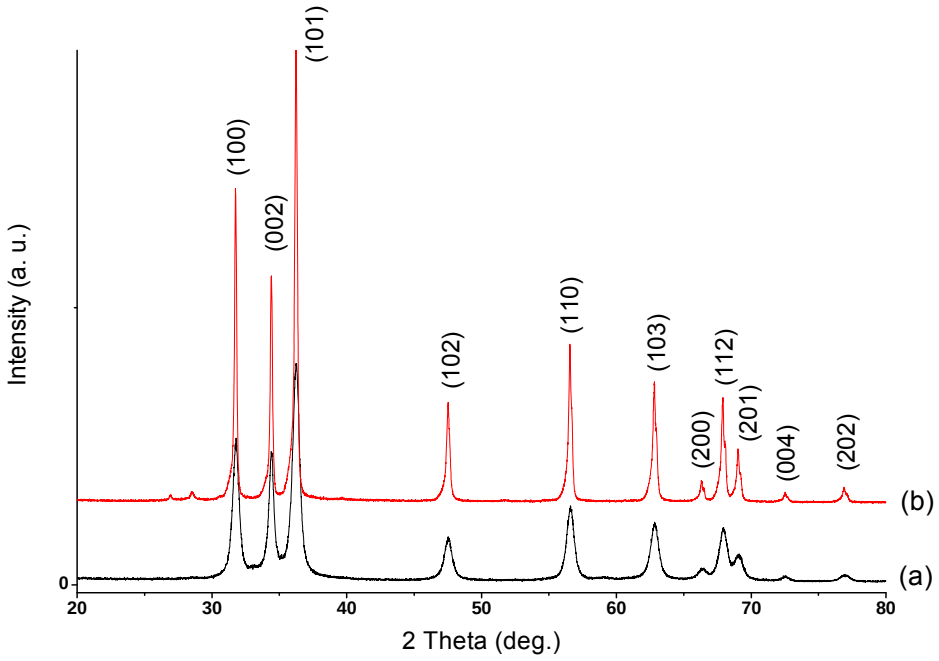

Figure 6.1 Powder X-ray diffractograms of zinc oxide nanoparticles: (a) as-prepared; (b) after firing at 800°C.

Figure 6.2 presents the SEM micrograph of the fired luminescent ZnO:Zn nanophosphors. From the micrograph, it can be seen that the morphology of the nanophosphors after firing is significantly modified, unlike the as-prepared nanoparticles which have a smooth spherical shape before firing (see Figure 5.3). In Figure 6.2 it is apparent that the nanoparticles after firing have plate- and pillar- like shapes along with rough surfaces, which probably arise from the loss of oxygen atoms [263] [268]. In addition, it is also noticed that a number of the nanoparticles are aggregated to form larger entities, leading to more irregular overall morphology.

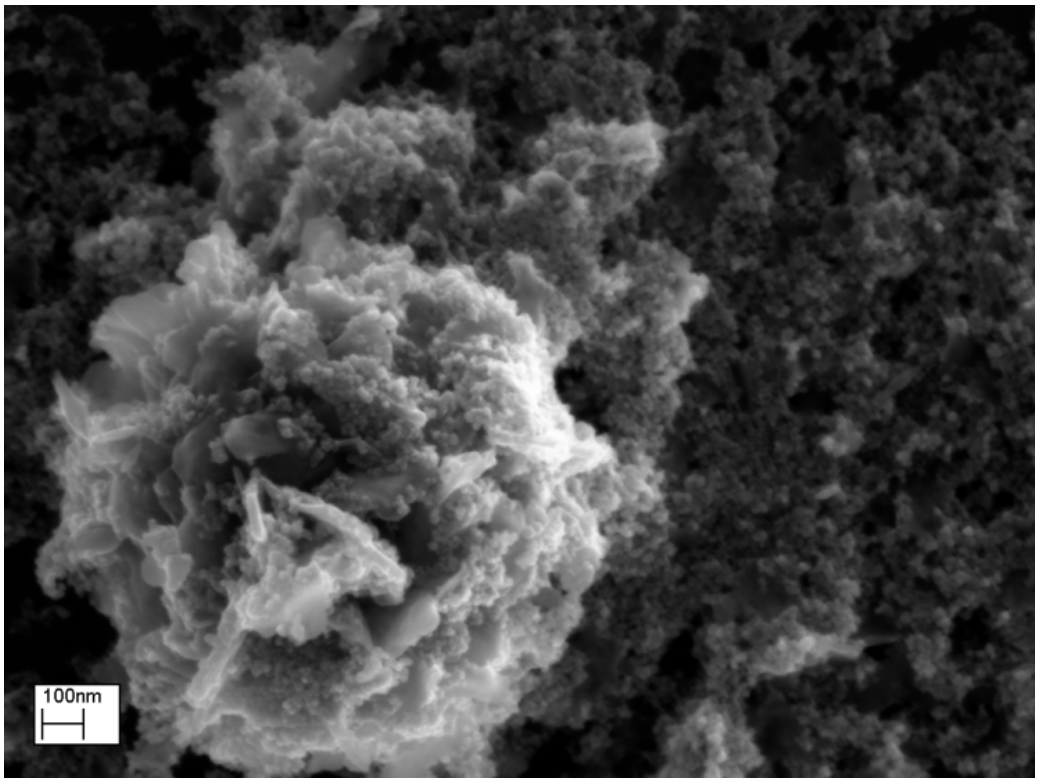

Figure 6.2 SEM image of the reduced ZnO:Zn nanophosphors

The Raman spectrum of the ZnO:Zn nanophosphors is displayed in Figure 6.3, in the range from 200 to 700 cm^{-1}. The sharp peak shapes are evidence that high degree of crystallinity in the wurtzite hexagonal structure was achieved. There is a shift of the main Raman bands to 331 and 436 cm^{-1}, respectively, compared with that of the pure ZnO nanoparticles shown in Figure 5.4 (which exhibits the Raman bands at 333 and 438 cm^{-1}). The shift is possibly due to the lattice mismatch induced during the reducing firing process [259] [291]. It is also notable that the Raman band at 580 cm^{-1}, which is associated with the zinc interstitials and oxygen vacancies, shows a dramatic increase (compared to that in Figure 5.4) in intensity after firing. This again provides evidence for lattice disorder. These results are consistent with the reducing of the ZnO lattice to form ZnO:Zn and the latter now manifests the photoluminescent characteristics displayed in Figure 6.4.

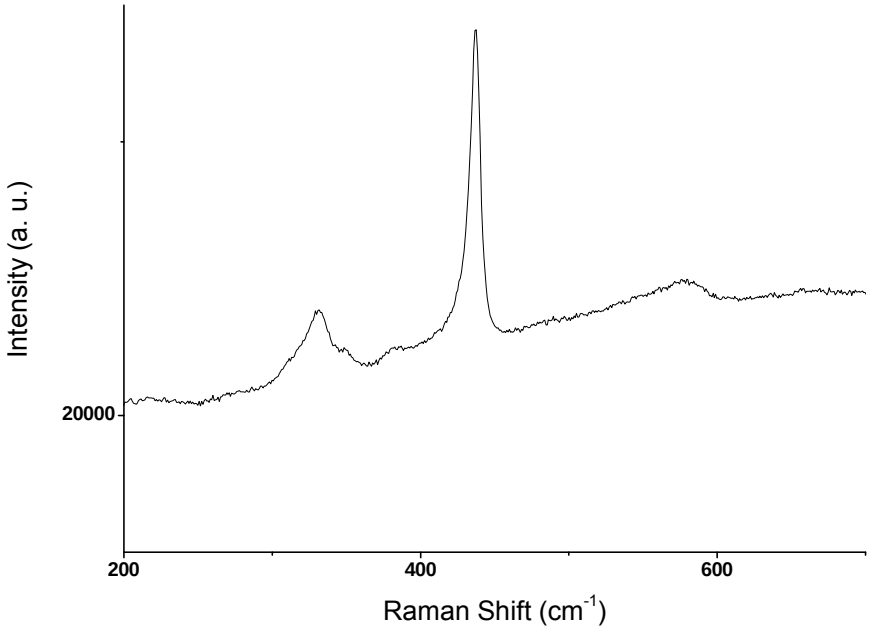

Figure 6.3 Raman spectrum of the luminescent ZnO:Zn nanophosphor

Figure 6.4 displays the excitation and emission spectra of the ZnO:Zn nanophosphors. After firing at 800°C, the ZnO:Zn absorbs broadly across nearly the entire ultraviolet range (from at least 250 to 400 nm) of the electromagnetic spectrum, and gives a strong luminescent green emission with the peak centred around 500 nm.

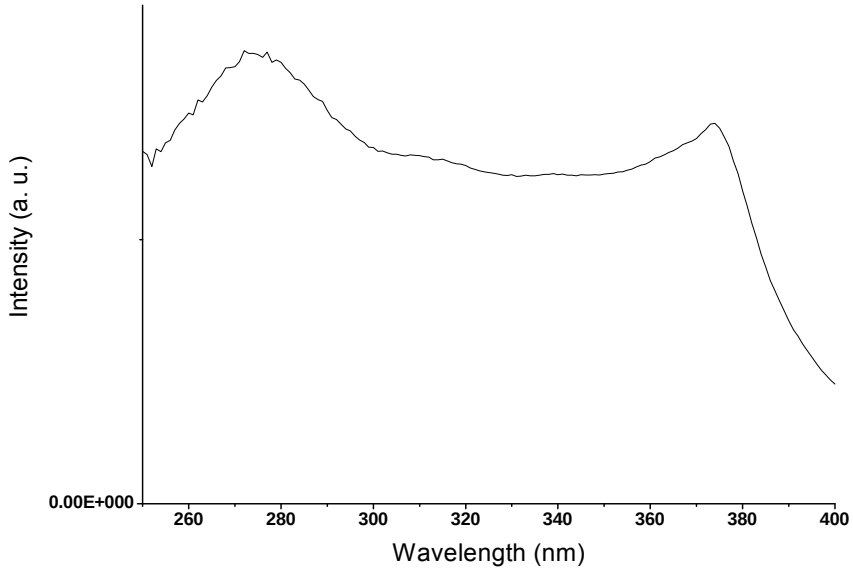

(a)

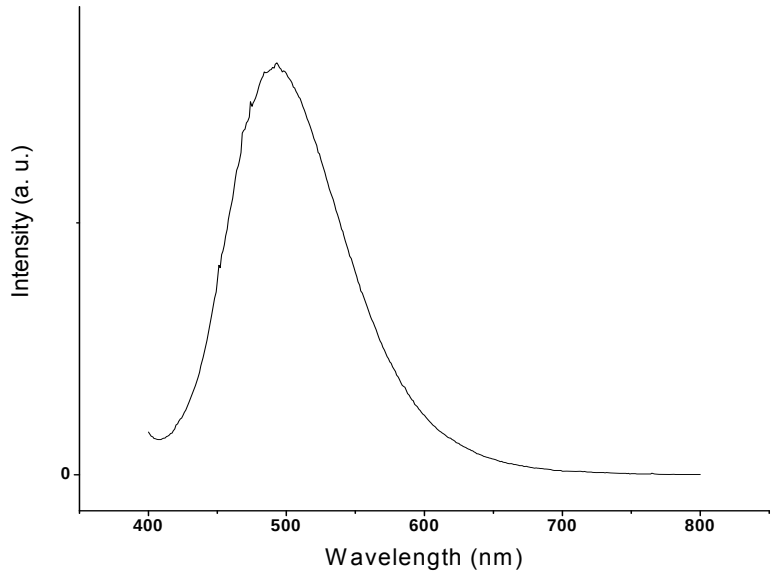

(b)

Figure 6.4 The photoluminescence spectra of the ZnO:Zn nanophosphors (a) excitation spectrum, monitored at 500 nm; (b) emission spectrum, excited at 350 nm.

6.3 Polystyrene – ZnO:Zn nanocomposite formation via the solvent casting technique

In Figure 6.5 an SEM micrograph of the polystyrene composite film containing 1wt% of the ZnO:Zn nanophosphors is presented. The preparation method of this film was described in section 2.12. It can be clearly observed that as a result of using the solvent casting technique, the ZnO:Zn nanophosphors were homogeneously dispersed into the polystyrene film and few agglomerates could be found. This good dispersion of the nanophosphors can be further demonstrated by Figure 6.9 which will be discussed later.

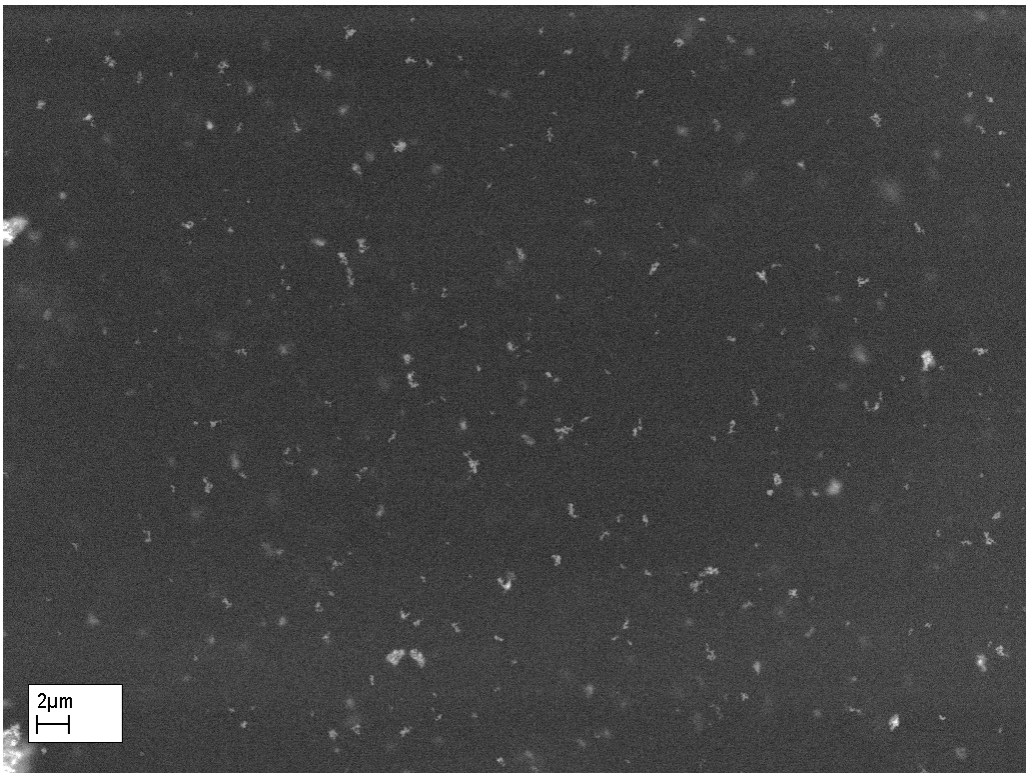

Figure 6.5 SEM image of the polystyrene film incorporating the ZnO:Zn nanophosphors.

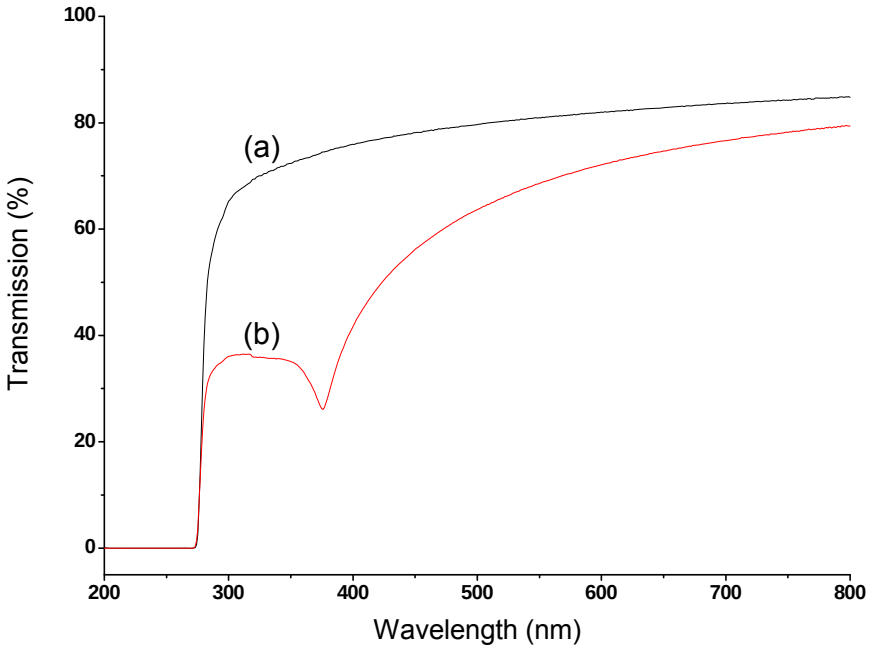

Figure 6.6 Transmission spectra of (a) the virgin polystyrene film and (b) the polystyrene film containing 1wt% of the ZnO:Zn nanophosphors.

A transmission spectrum of the virgin polystyrene film is displayed in Figure 6.6(a) as a reference, and Figure 6.6(b) presents a transmission spectrum of the polystyrene film containing 1wt% of the ZnO:Zn nanophosphors. From the spectra it is clear that compared with the virgin polystyrene film, the one containing the ZnO:Zn nanophosphors does not lose much transmission in the visible region of the electromagnetic spectrum due to the very even dispersion of the nanophosphors, but significantly absorbs ultraviolet light in the region between 275 and 400 nm.

(a) (b) (c)

Figure 6.7 Transparency comparison: (a) no cover; (b) covered with the virgin polystyrene film; (c) covered with the polystyrene film containing 1wt% of the ZnO:Zn nanophosphors.

In Figure 6.7 the transparency of the polystyrene film containing the ZnO:Zn nanophosphors to visible light is compared to that of the virgin polystyrene film. Clearly the comparison is quite favourable.

The excitation and emission spectrum of the polystyrene film containing 1wt% of the ZnO:Zn nanophosphors are presented in Figure 6.8. It is obvious that the ZnO:Zn nanophosphors still absorb the ultraviolet light with a broad absorption peak spanning most of the ultraviolet region, and in addition now give a strong green emission even when incorporated into the polystyrene (due to down conversion of the UV radiation). The peak positions observed in the excitation and emission spectrum do not appear to be influenced by the presence of the polystyrene when compared with the spectra in Figure 6.4.

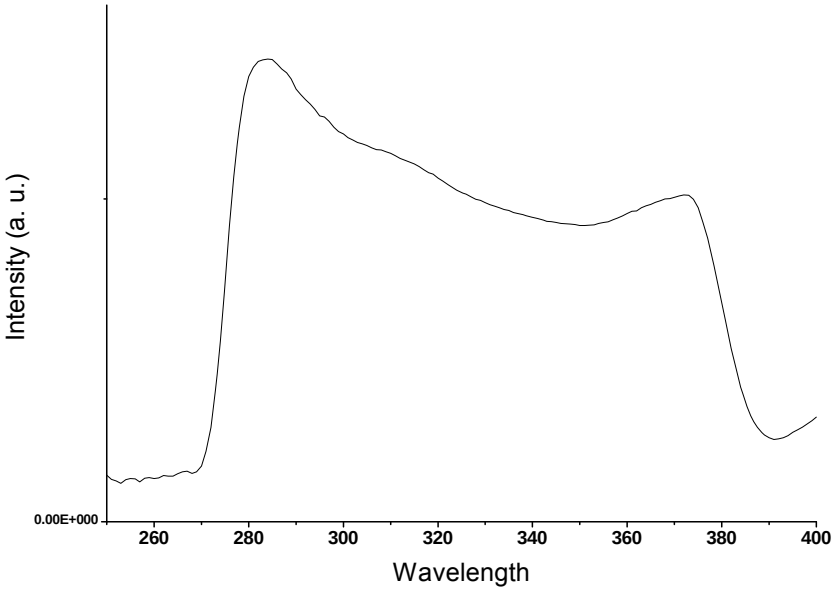

(a)

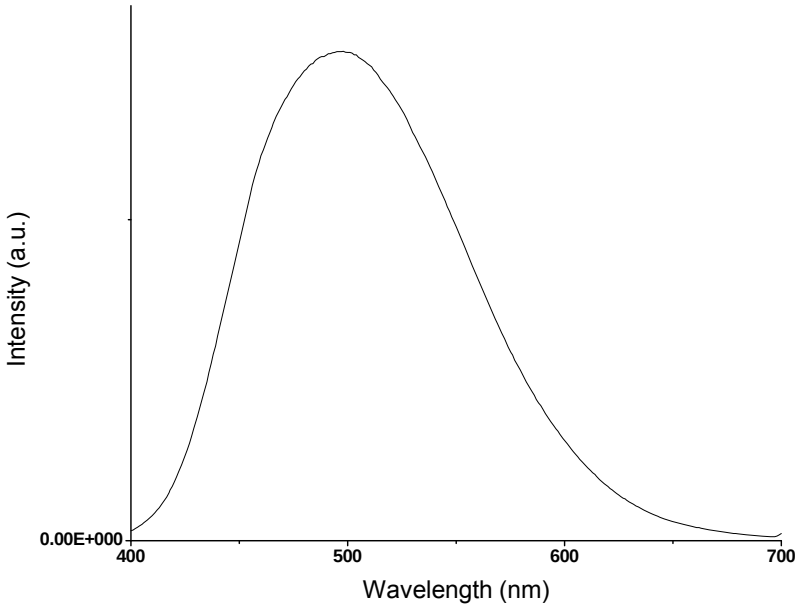

(b)

Figure 6.8 The polystyrene film containing 1wt% of the ZnO:Zn nanophosphors: (a) excitation spectrum, monitored at 500 nm; (b) emission spectrum, excited at 350 nm.

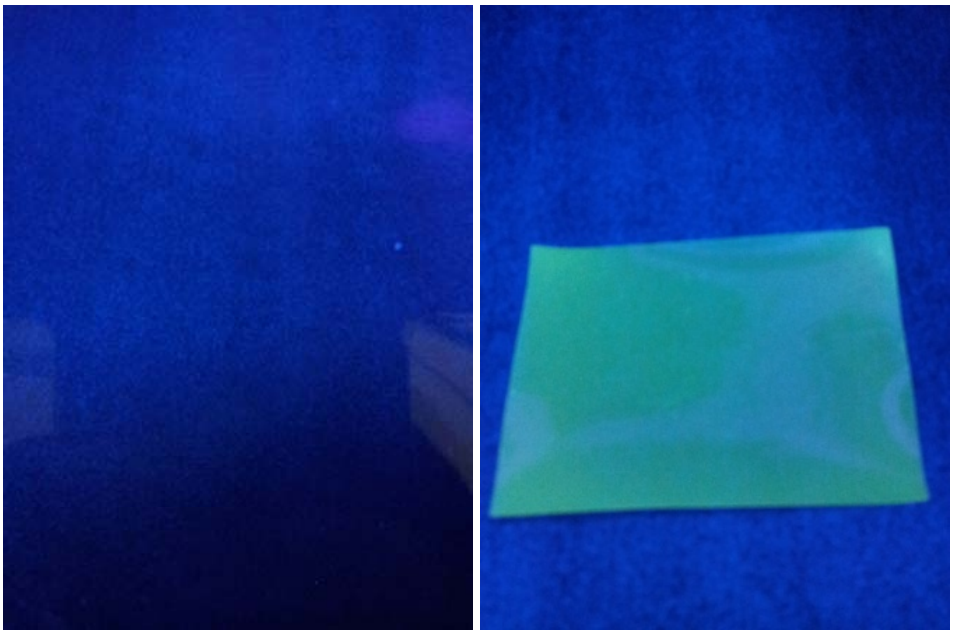

(a) (b)

Figure 6.9 Glow comparison under the UV lamp: (a) shows the virgin polystyrene film; (b) shows the polystyrene film incorporating 1wt% of the ZnO:Zn nanophosphors.

Figure 6.9 shows the virgin polystyrene film (Figure 6.9(a)) and the polystyrene film containing 1wt% of the ZnO:Zn nanophosphors (Figure 6.9(b)) under a UV excitation at 366 nm. The virgin polystyrene film does not show any luminescence, while the film containing the ZnO:Zn shows a fairly uniform green emission. Both films show good transparency to visible light (see Figures 6.7(b) and (c)). The uniform green emission here again demonstrates the good dispersion of the ZnO:Zn nanophosphors in the polystyrene matrix.

6.4 Conclusions

Incorporation of the ZnO:Zn nanophosphor into the polystyrene via the solvent casting technique was demonstrated to be an effective way to achieve the good dispersion of the nanoparticles. This even distribution leads to the composite having extremely high transmittance which was demonstrated by either the UV-Vis spectrum or the photos that show the transparency comparison between the composites and the virgin polystyrene. The photoluminescent properties of the ZnO:Zn nanophosphor, both as a pure powder and as a filler embedded into its polystyrene composite, were investigated. In addition the composite manifests a uniform green emission if it is excited under a UV lamp. These excitation and emission characteristics indicate that the luminescent zinc oxide nanophosphor can be used not only as an inhibitor of the UV degradation of polymers, but also for providing polymers with light emitting functionality.

From this work a number of conclusions can be deduced:-

1. ZnO nanoparticles can be successfully reduced at high temperature with limited growth to form ZnO:Zn nanophosphors.
2. The crystal information and particle morphology of the ZnO:Zn nanophosphors were studied and compared to those of ZnO nanoparticles. A decrease in cell volume was observed. This is probably due to increased long range order as the nanoparticle size increases.
3. These ZnO:Zn nanophosphors have good luminescent properties very similar to those of conventional larger ZnO:Zn phosphor particles.
4. The heat treated ZnO:Zn nanophosphors were incorporated into polystyrene films successfully via the solvent casting technique.
5. The transparency of the polystyrene films containing the ZnO:Zn nanophosphors was very reasonable and the incorporation of the

nanophosphors did not lead to scattering problems.

6. The excitation and emission spectra of the successfully incorporated ZnO:Zn nanophosphors in polystyrene manifest the same spectral properties as they did as a separate powder.
7. The fact that ZnO:Zn nanophosphors embedded in the polymers emit light in the visible region when the films are subjected to UV excitation verifies the idea of protecting the polymer from UV by down-converting the UV radiation into the visible spectrum works.
8. Spin-offs from the fact that it has been demonstrated herein that ZnO:Zn nanophosphors emit light in the visible region when encapsulated in the polymer could include lighting elements made from these ZnO:Zn containing polymer sheets.

Chapter 7 Surprises Encountered in Coating Zinc Oxide Nanoparticles with Alumina

7.1 Introduction

It has been well established that the properties of particles depend on their composition size and morphology. In addition for particles with one or more dimensions below 50 nm the significance of the surface energy compared to the total energy increases as particle sizes decrease. When the particles of semiconducting materials become very small additional properties come into play that are dependent on particle sizes, these have been referred to as “quantum size effects” and influence the electronic properties and the band gap size in nanoparticles [292] [293] [294] [295]. Reports of such effects in semiconducting metal oxide and sulfide nanoparticles have been instrumental in driving forward and developing understanding of how such nanoparticles can contribute to enhancing everyday life.

In this chapter the semiconducting metal oxide zinc oxide (ZnO) is again the material studied. The chemical/physical properties of ZnO have been covered in sections 5.1 and 6.1.

This chapter reports studies on the use of ZnO to control polymer degradation. It was also discussed at the beginning of this thesis (see chapter 1) that many polymers are observed to degrade when exposed to ultraviolet light. Common synthetic polymers which are attacked include polypropylene where tertiary carbon-hydrogen bonds are the primary focus of attack. It is believed that the ultraviolet radiation induces charge transfer complexes between the polymer and oxygen thus leading to photolysis, producing CO and CO_2. This is known as photooxidative degradation [56]. UV radiation stabilisers are used in plastics to reduce or

prevent degradation by the UV light. Examples include benzophenones which absorb the UV light thereby preventing the formation of free radicals, and hindered amine light stabilisers which act by quenching oxygen-polymer charge transfer complexes that are the initiators of the photooxidative degradation [56] [296].

In chapter 4 it was reported that iron doped lithium aluminate ($LiAlO_2:Fe^{3+}$) nanoparticles, which absorb and are excited by a broad wavelength range of ultraviolet light and re-emit the energy in the 700-800 nm region of the electromagnetic spectrum, can be used to protect polymers by downconverting the UV light into the near infrared light. These results were published [183] [297] [298] and it was also demonstrated that the absorption/excitation and emission characteristics make the phosphor ($LiAlO_2:Fe^{3+}$) an ideal candidate material for the reduction of damage by UV radiation to polymers when presented as either a surface coating for the polymer or as a filler within the polymer.

As an alternative approach ZnO (uncoated) was also investigated as a UV blocking agent (see chapters 5 and 6). During the early stages of this work there were two problems that were also reported by other workers [299] that are due to the intrinsic properties of ZnO itself. The first was the compatibility of the ZnO nanoparticles with the polymer which could manifest nanoparticle aggregation; but this was overcome by the processing technology (see chapter 5). The second was a more fundamental problem that arises from the band gap (3.37 eV) of the ZnO semiconductor, here the inherent photoconductivity of the nanoparticles facilitates the formation of active species within or at the polymer surface and degrades the material [300] [301]. For the latter problem it was decided to try the approach of protecting the polymers from the ZnO nanoparticles by coating the nanoparticles with a protective layer. The idea behind this approach was to isolate the nanoparticle surfaces from the polymers that are to be protected by them. The details are presented and discussed in this chapter.

The work reported in this chapter was based on a literature report [162] on the preparation of ZnO nanoparticles coated with a homogeneous Al_2O_3 layer. Unfortunately, when this method was used a number of unexpected results came to light which showed some drawbacks in the original method that were not reported [162]. This has led to a new understanding of what really happens in coating nanoparticles of ZnO with precursors for Al_2O_3 and some interesting unexpected chemistry. The implications and potential new applications of following the method given in reference [162] are also reported herein.

7.2 Phases present in alumina coated zinc oxide precipitates

The details of the sample preparations for alumina coating on the ZnO nanoparticles were described in section 2.5. The fitting of the X-ray powder diffraction (XRPD) data of some of the materials that went through the chemical coating process and then the firing process led to average crystallite sizes in the ZnO nanoparticles being apparently smaller after the coating/firing processes than before the processes (see Table 7.1) for the as received nanoparticles (sample 1) from Johnson Matthey (19.3 nm), whereas after the coating/firing processes the ZnO (samples 2B and 3B) crystallite sizes were 12.7 nm and 9.3 nm, respectively.

Table 7.1 Phases present and crystallite sizes within the ZnO nanoparticles and their products

Sample and sample number( )	**Phase present in XRPD data and lattice parameters**	**Crystal size (nm)**
JM ZnO (sample 1)	ZnO, *a* = 3.2525(1) Å, *c* = 5.2141(2) Å	19.32(5)
Al_2O_3:ZnO (5%) (sample 2B)	ZnO, *a* = 3.2532(2) Å, *c* = 5.2131(3) Å	12.70(4)
Al_2O_3:ZnO(5%) (sample 3B)	ZnO, *a* = 3.2526(3) Å, *c* = 5.2158(5) Å	9.32(3)
JM ZnO fired in air at 600°C for 1h (sample 1L)	ZnO, *a* = 3.2519(1) Å, *c* = 5.2104(2) Å	78.54(25)
Al_2O_3:ZnO (5%) before firing (sample 2A)	$Zn_5(OH)_6(CO_3)_2$ *a* = 13.7200(42) Å, *b* = 6.3473(14) Å, *c* = 5.3705(15) Å, *β*= 95.730(20)° 80.7(19)% of this material is present	10.25(10)
	$Zn_{0.65}Al_{0.35}(OH)_2(CO_3)_{0.167}(H_2O)_{0.499}$ *a* = 3.0764(1) Å, *c* = 22.75(2) Å 19.3(19)% of this material is present	14.08(25)

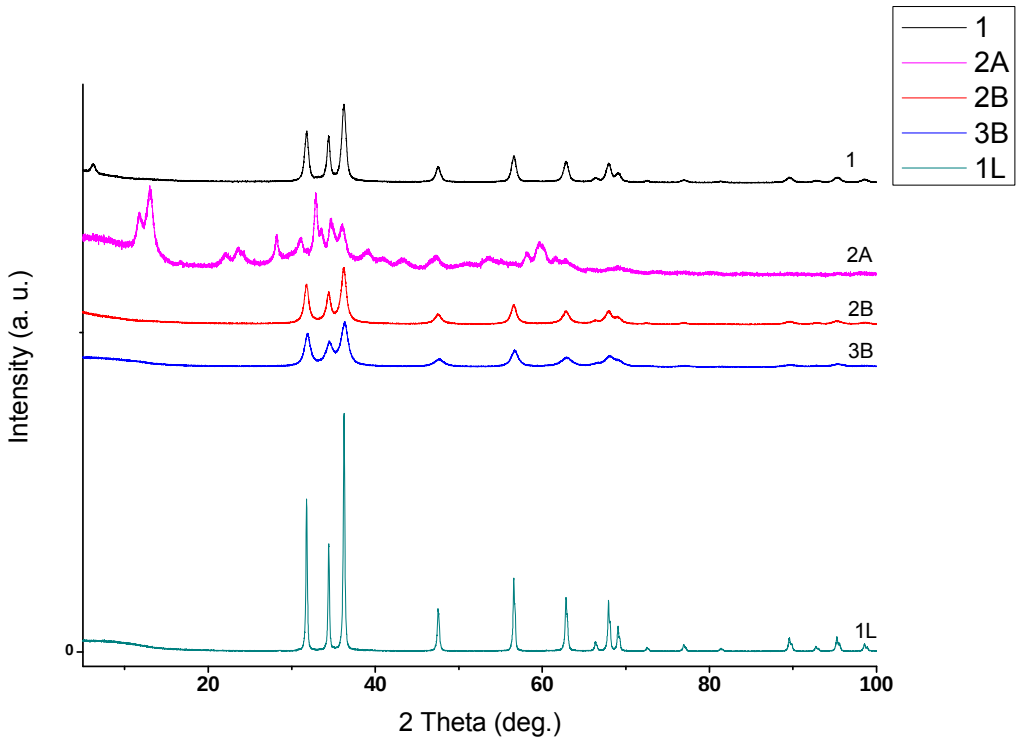

Figure 7.1 XRPD diffractograms of the ZnO nanoparticles of JM sample 1 and the samples prepared from it. Sample 2A is clearly not based on ZnO, but fits to two carbonate phases (see text). Samples 2B and 3B are ZnO based materials prepared by firing samples 2A and 3A. Sample 1L is the larger nanoparticles prepared by firing sample 1.

Clearly this was difficult to understand if the processes had only coated the ZnO particles with Al_2O_3. It was therefore decided to investigate the XRPD data of the material precipitated from the coating method before firing.

The XRPD diffractograms obtained are presented in Figure 7.1. Clearly the diffractogram of the material precipitated from the solution (sample 2A) shows no evidence for the presence of ZnO (see ZnO patterns in Figure 7.1 of the as supplied JM ZnO sample 1 before going through the coating method and also that of the particles after firing (samples 2B and 3B)). In fact the data for sample 2A provides evidence that after precipitation there are two materials present [$Zn_5(OH)_6(CO_3)_2$]

(80.7(19)%) and $[Zn_{0.65}Al_{0.35}(OH)_2(CO_3)_{0.167}(H_2O)_{0.499}]$ (19.3(19)%). The data was fitted by Reitveld refinement using the fundamental parameters method. The percentages from the XRPD data fitting depend on several factors so cannot be taken as an exact ratio of the two materials present. Figure 7.1 also presents the XRPD diffractogram of the larger nanoparticles (sample 1L) which were made from the JM ZnO nanoparticles (sample 1) and only went through the same firing condition as that of sample 2B and 3B. Here the pattern is much closer to that of bulk ZnO.

Although the cell parameters from bulk $[Zn_5(OH)_6(CO_3)_2]$ (a = 13.62 Å, b = 6.3 Å, c = 5.3705 Å, β = 95.83° , see reference [302]) were used as starting parameters to fit the data for sample 2A, the resulting cell size is larger (see Table 7.1) as expected for a nanometre sized material. In addition it is not necessary to assume that this material does not contain Al^{3+}, on the contrary it is believed that it does for the reasons explained below and this point will be again discussed later.

Figure 7.2 presents an SEM and TEMs of one of the as received JM ZnO nanoparticle samples (sample 1) and an SEM of particles from sample 1L. In contrast two kinds of crystals (acicular long crystals and more rounded plate like crystals) are observed in the SEM and TEM micrographs of sample 2A shown in Figure 7.3.

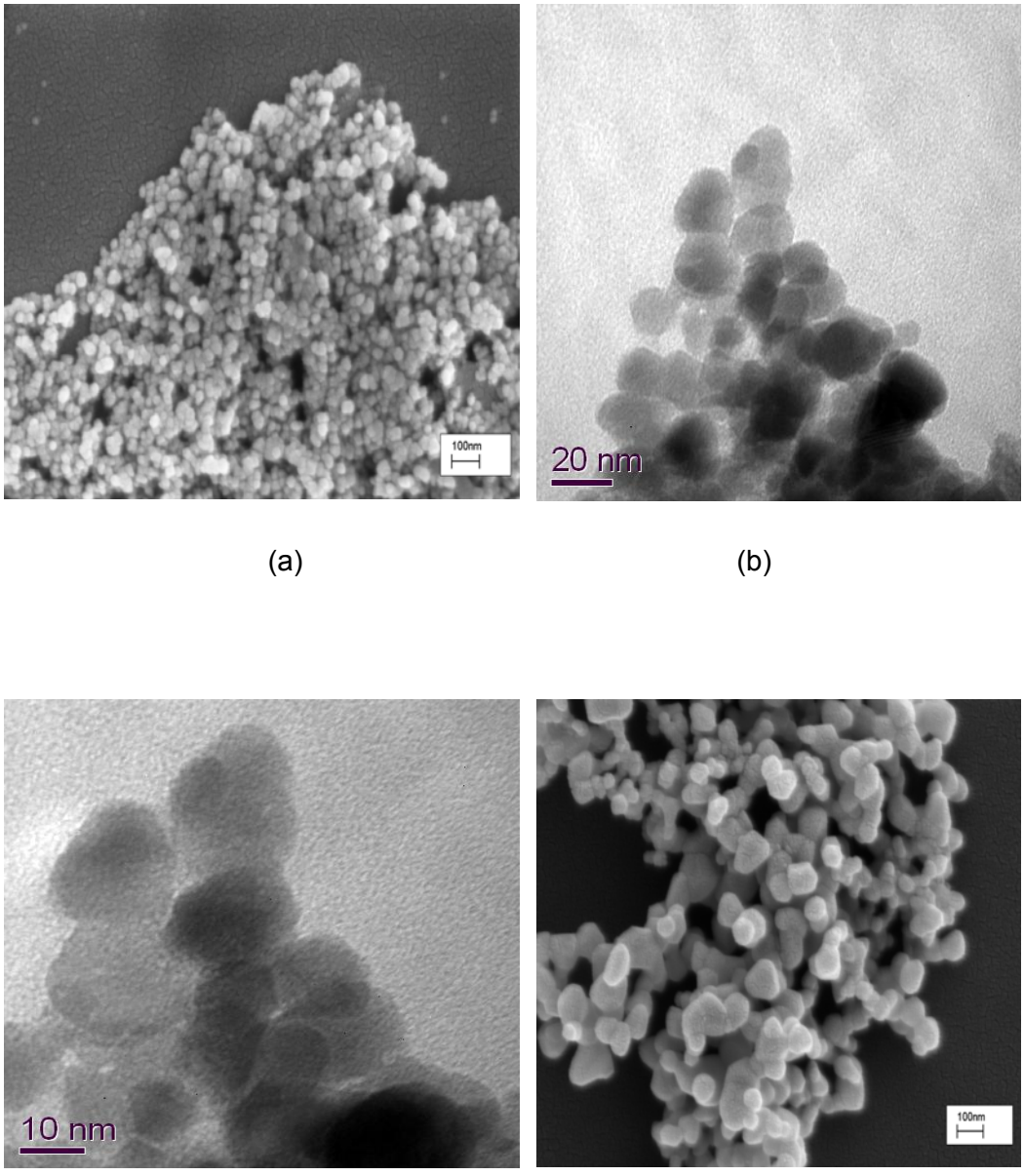

(a) (b)

(c) (d)

Figure 7.2 SEM (a) and TEMs (b) and (c) micrographs of nanoparticle crystals of ZnO as supplied by JM (sample 1). An SEM (d) is of sample 1L.

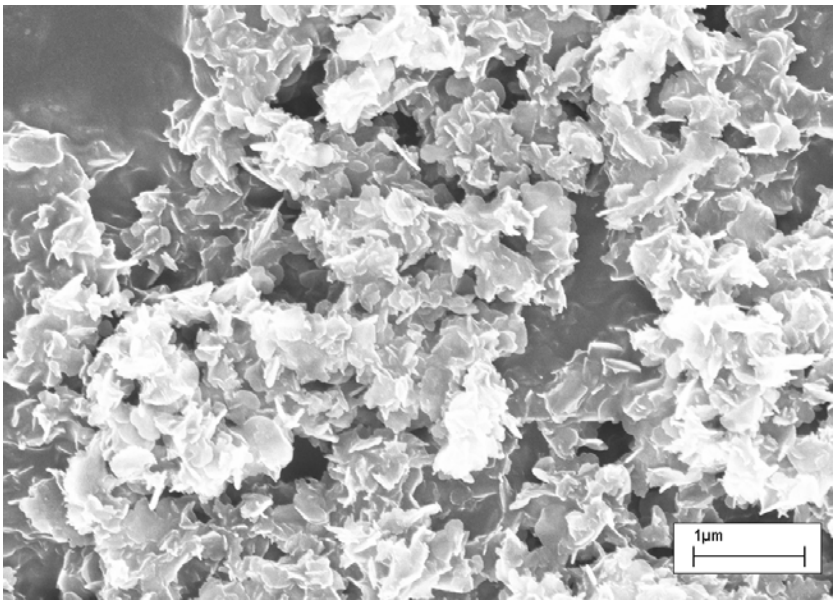

(a)

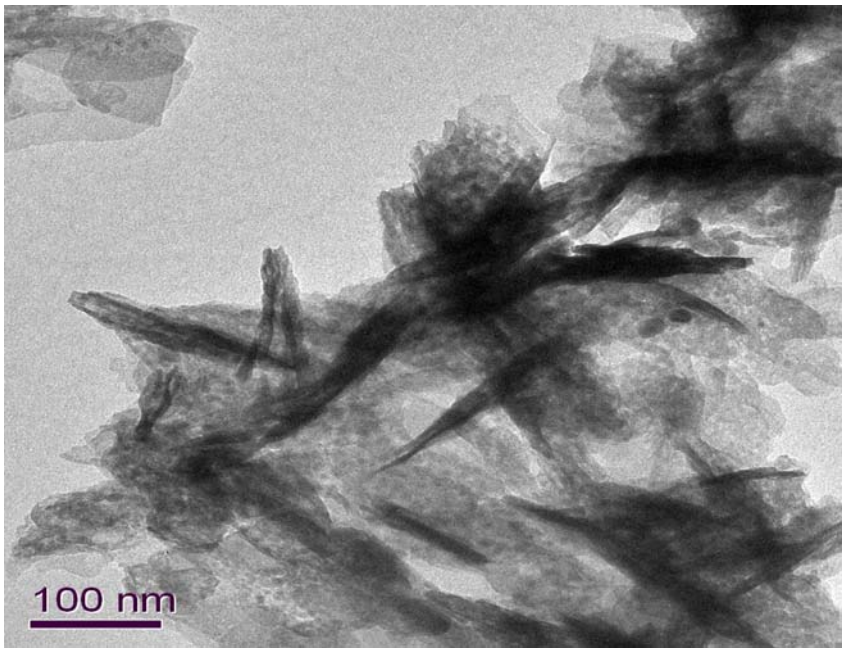

(b)

Figure 7.3 SEM (a) and TEM (b) micrographs of crystals precipitated from the Al_2O_3:ZnO (5% ratio) in the dilute conditions (sample 2A)

The previous work assumed only the $Zn_5(OH)_6(CO_3)_2$ (BCZ) was present [162] and that these particles were then coated with $Al(OH)_3$ also assumed to be the form. The Al^{3+} was induced after using $Al_2(SO_4)_3$ as the source material. From the results reported here this is not proven rather the Al^{3+} is present in the precipitate as $[Zn_{0.65}Al_{0.35}(OH)_2(CO_3)_{0.167}(H_2O)_{0.499}]$ and there is no reason to believe that the BCZ identified above does not also include the Al^{3+}.

Clearly as the nanometre sized crystals of ZnO used in this work are able to react with the solutions in preparation 1 (see section 2.5), this indicates that the chemical equations given in reference [162] need to be modified in the light of results reported herein to take into account the XRPD data. Their equation 1 is not relevant as this represented the stage before the $Al_2(SO_4)_3$ solution was added [162] and as shown here clearly the zinc species (in this case ZnO nanoparticles and in theirs BCZ nanoparticles) will react with the sulfate solution and the additional NH_4HCO_3 solution. Similarly as they did not take the latter fact into account, their equations 2 and 3 are also not relevant. However, as the exact ratio of the two products is difficult to define, it is not possible to balance the equation exactly from the XRPD data fitting here. In addition the exact amount of Al^{3+} in the $[Zn_{5-x}Al_x(OH)_6(CO_3)_2]$ is still unknown, hence the chemical equation can only be given in this somewhat rough form taking account of only the precipitate not the starting ratios of Al^{3+} to Zn^{2+}:-

$$5.6[ZnO] + 8.5[NH_4HCO_3] + X[Al_2(SO_4)_3] + H_2O =$$
$$4[Zn_{5-(2x-0.35)}Al_{2x-0.35}(OH)_6(CO_3)_2]\downarrow + [Zn_{0.65}Al_{0.35}(OH)_2(CO_3)_{0.167}(H_2O)_{0.499}]\downarrow$$
$$+ 3X[(NH_4)_2SO_4] + (8.5-3X)[NH_4OH]$$

In fact if it is assumed that all the Al^{3+} and Zn^{2+} present in the reaction ends up in these precipitates, the above equation could be balanced. However, in this work the main thrust is to indicate the chemistry taking place, so it is really beyond the scope to follow such assumptions. From measuring the pH it can be found that the final pH is

slightly alkaline hence ammonium hydroxide is formed. This equation explains the evidence for the fact that the ZnO nanoparticles had dissolved/reacted or dissolved and then reacted with the chemicals present in the solution, forming the two materials that precipitated from the solution. The crystallite sizes for these materials are also smaller than the original crystallite size of the JM ZnO (see Table 7.1) and this is readily explained as the original ZnO particles had dissolved.

7.3 Morphology and crystal structures of zinc oxide nanoparticles after coating

Surprisingly, firing the precipitates from the preparation 1 in section 2.5 gives XRPD data (see Figure 7.1) that shows the presence of what appears to be only ZnO although as will be discussed later in this section, the XRPD patterns of the nanoparticles that have been prepared through the chemistry reported herein have some obvious differences to the initial unreacted ZnO nanoparticles.

SEM micrographs of sample 2B (see Figure 7.4) appears to show that the ZnO particles are coated in (a) and (b), but (c) and (d) taken from the same sample show little evidence for any coating.

Figure 7.5 presents elemental mapping analysis of the sample 2B in which it is difficult to rule out the presence of some Zn^{2+} in the coating (clearly the general pattern of the Zn micrograph Figure 7.5(b) follows that of the crystals shown in the SEM micrograph Figure 7.5(a)), nor it is able to rule out the presence of Al^{3+} in the ZnO (micrograph Figure 7.5(c)), though in Figure 7.5(c) the Al^{3+} is fairly evenly distributed across the entire picture as would be expected from such a small concentration if it was not located only in a coating on the crystals. In addition as the Al^{3+} is not located in discrete particles but spread out evenly, it can be concluded that both the $[Zn_{5-(2x-0.35)}Al_{2x-0.35}(OH)_6(CO_3)_2]$ and $[Zn_{0.65}Al_{0.35}(OH)_2(CO_3)_{0.167}(H_2O)_{0.499}]$ contain the Al^{3+} and that they both form nanometre sized particles of ZnO doped with Al^{3+} on firing.

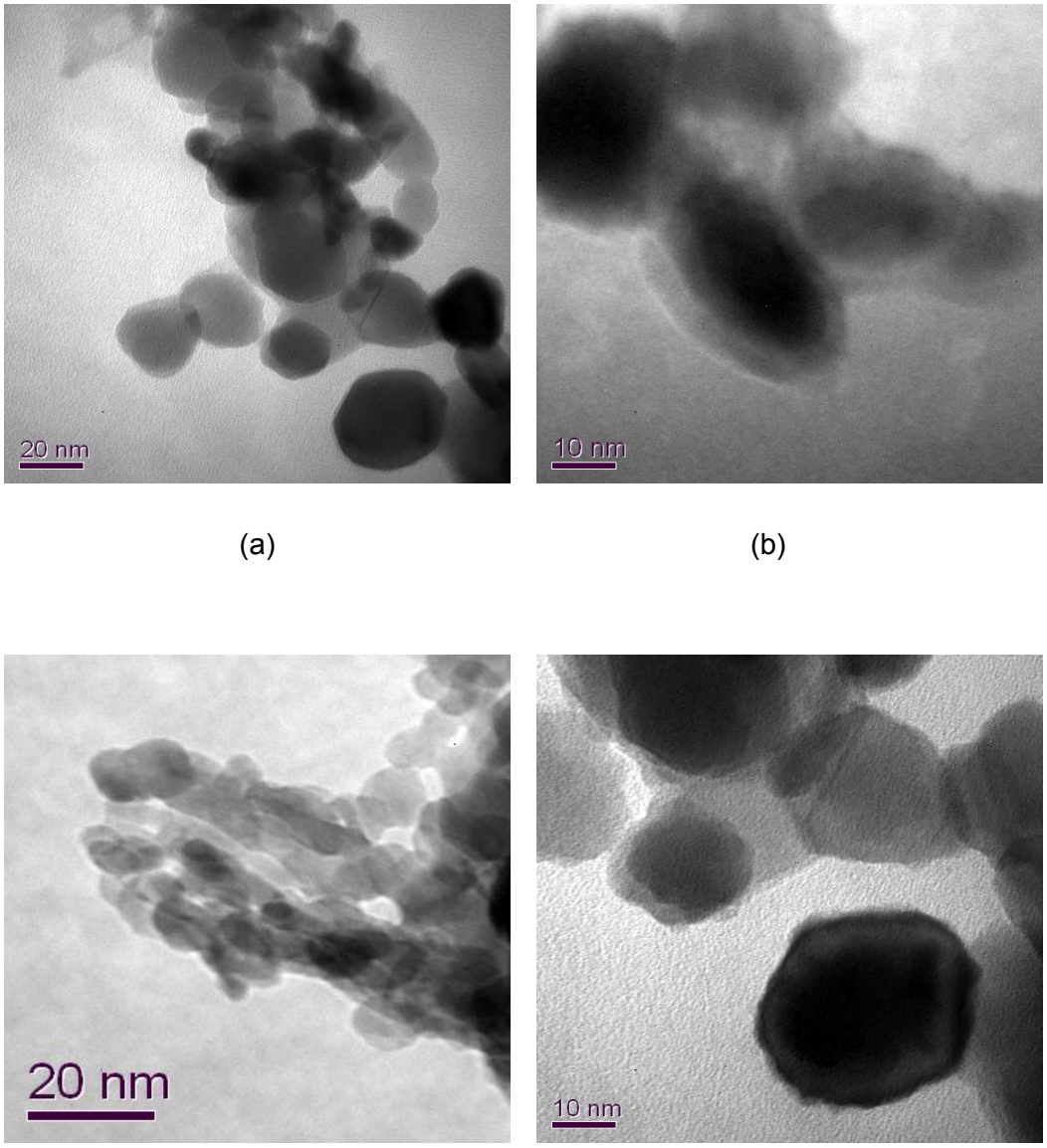

Figure 7.4 TEM micrographs of crystals of ZnO fired from the materials precipitated from the Al_2O_3:ZnO (5%) in the dilute conditions (sample 2B). In (a) there appears to be evidence for only 1 or 2 particles being coated, in (b) there appears to be evidence for several particles being coated, in (c) there is no evidence for particles being coated and in (d) there is detail that could be confused as a coating but only on one particle.

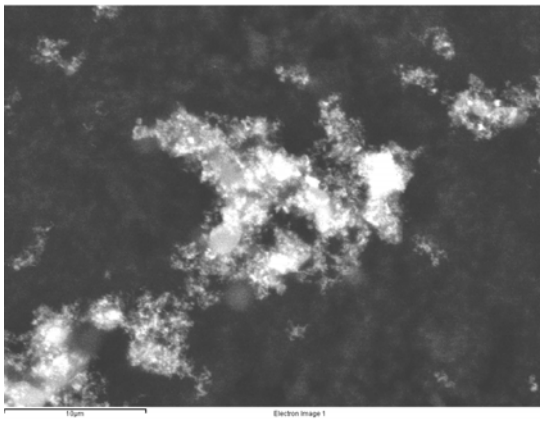

(a)

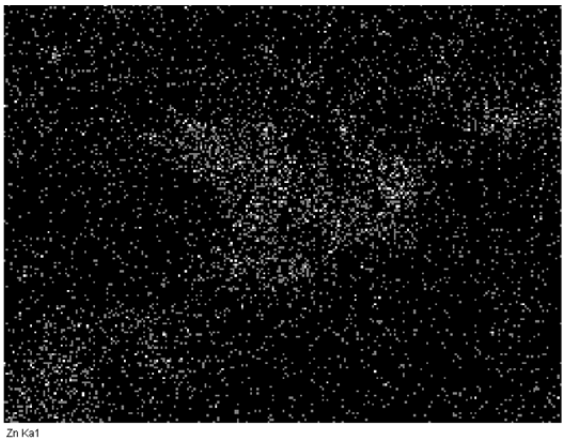

(b)

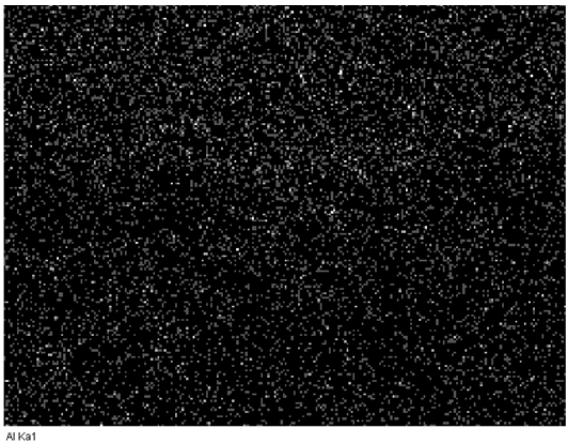

(c)

Figure 7.5 SEM of crystals of ZnO fired from the materials precipitated from the Al_2O_3:ZnO (5%) in dilute conditions (sample 2B) (a), showing the distributions of zinc (b) and aluminium (c) on a silicon substrate.

Including Al^{3+} into the crystal structure of ZnO has been previously reported [303] for aluminium doped ZnO (AZO) nanoparticles (it should be noted that on firing both materials will lose particle volume when converting to AZO particles). In that work [303] the diffraction line around a 2Ɵ value of 34° begins to coalesce with the line around 36° as the concentration of the Al^{3+} increases. There is some evidence for this in the data shown in Figure 7.1 and this is in keeping with the Al^{3+} being present in the bulk of the ZnO nanoparticle's crystal structure in AZO [303]. The unit cell data given in Table 7.1 shows an increase in lattice volume when the Al^{3+} is incorporated into the ZnO lattice to form AZO (see the cell data for samples 1, 2B and 3B in Table 7.1). The previous work [303] that generated AZO nanometre sized particles (by a very different method) gave the bulk ZnO cell as a = 3.2417 Å, c = 5.1867 Å and stated "as generally observed, the lattice parameters of the nanocrystalline particles are significantly higher compared to the bulk" in agreement with the findings reported here. They also reported that the value of 'c' decreases as the concentration of the Al^{3+} in the AZO increases whereas the value of 'a' first increases and then decreases, and put forward a plausible explanation based on the sizes of Al^{3+} and Zn^{2+}. Whilst in this work the lattice values are not exactly the same as all the values are larger, the overall trend is the same. The larger values may result from the differing preparation route for the incorporation of the Al^{3+} cations. This may result in different coordination number preference or as the samples 1 and 4 of ZnO nanoparticles prepared by JM (in large quantities) both show a larger 'a' parameter and one of them a larger 'c' parameter than those of the ZnO nanoparticles in reference [303]. It may be that the preparation/firing temperature is dominant, as both JM samples are 25% larger in diameter than those of reference [303] and it would have been expected that the latter should have had the larger parameters. Nevertheless both this work and the previous work show an increase in lattice parameters when around 7% of the Al^{3+} is present in the AZO nanoparticles.

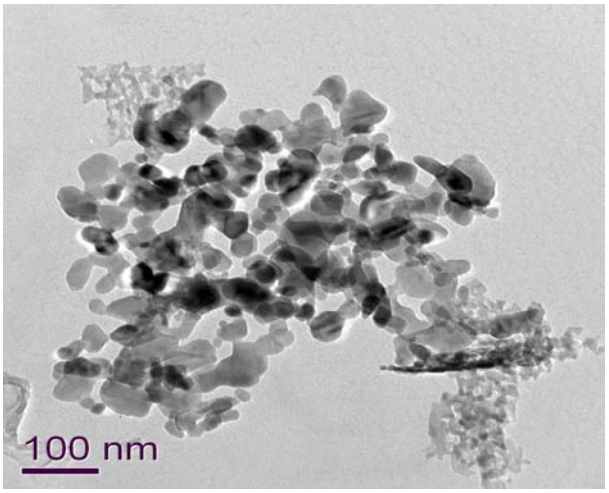

(a)

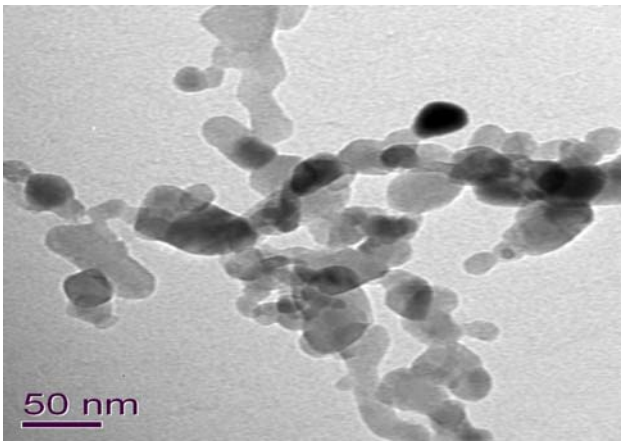

(b)

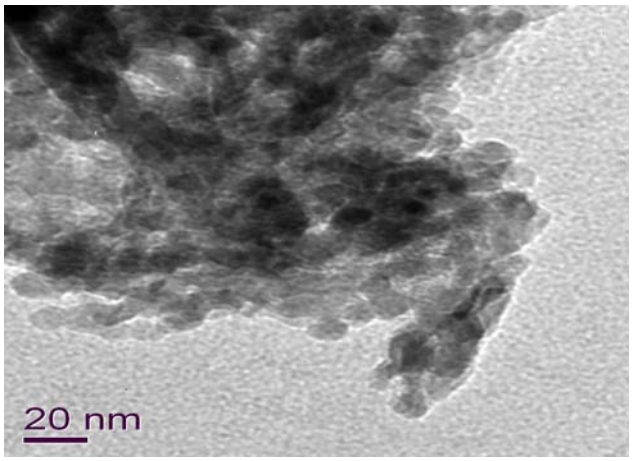

(c)

Figure 7.6 Crystals of ZnO fired from the materials precipitated from the Al_2O_3:ZnO (5%) in the concentrated conditions (sample 3B).

In Figure 7.6 TEM micrographs of the nanoparticles prepared from the Al_2O_3:ZnO (5wt% ratio as sample 3B) in the concentrated conditions (see preparation 2 in section 2.5) are presented. Here there is no evidence for the presence of distinct coating on the nanoparticles. It appears that all the Al^{3+} is in the crystal structure of ZnO. Further evidence for this is found in the XRPD data in Figure 7.1 for this material. It is apparent that the XRPD pattern is similar to that of the 7% Al^{3+} in the crystal structure of ZnO [303].

7.4 Al_2O_3 coating on large ZnO:Zn nanophosphors

As the small nanoparticles of ZnO dissolved in these solutions as described above (see sections 7.2 and 7.3), it seemed reasonable to investigate the effect of using much larger ZnO nanoparticles to start with. It was decided to produce larger nanoparticles of ZnO:Zn rather than ZnO as the former is a well-known phosphor and in addition it has UV screening potential that can down convert the UV light into visible light.

To form such nanoparticles a sample of ZnO nanoparticles supplied by Johnson Matthey were fired at 800°C for 45 minutes in a reducing atmosphere as described in section 2.6. This procedure gave rise to larger ZnO:Zn nanoparticles (sample 5) with the sample having an average crystallite size of 172.6 nm (see Table 7.2). The large ZnO:Zn nanoparticles then underwent the coating/firing process (which was described in section 2.6 and similar to preparation 1) to form samples 6A and 6B. In the XRPD diffractograms presented in Figure 7.7, those for samples 5, 6A and 6B are much sharper (more like bulk ZnO:Zn) than that of sample 4 as expected for much larger nanoparticles.

Table 7.2 Phases present and Crystallite sizes within ZnO Nanoparticles and their products

Sample and sample number( )	**Phase present in XRPD data and lattice parameters**	**Crystal Size (nm)**
JM ZnO (Sample 4)	ZnO, *a* = 3.2523(1) Å, *c* = 5.2111(1) Å	21.03(6)
ZnO:Zn (Sample 5)	ZnO:Zn, *a* = 3.2521(2) Å, *c* = 5.2096(4) Å	172.55(93)
ZnO:Zn/Al_2O_3 (Sample 6A)	ZnO:Zn, *a* = 3.2519(2) Å, *c* = 5.2095(5) Å	167.28(91)
ZnO:Zn/Al_2O_3 (Sample 6B)	ZnO, *a* = 3.2529(1) Å, *c* = 5.2111(1) Å	126.65(25)

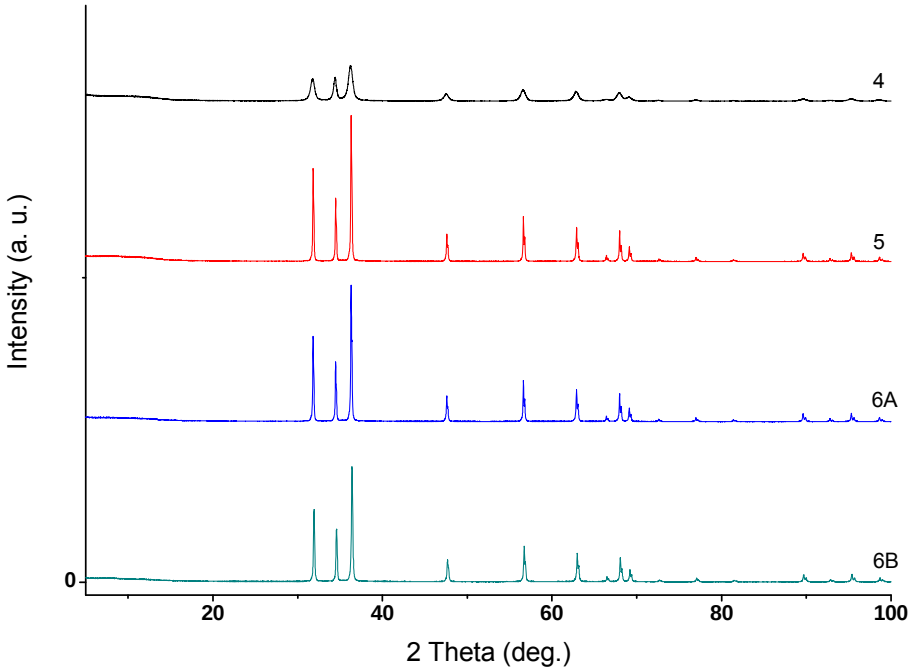

Figure 7.7 XRPD diffractograms of the ZnO nanoparticles of JM sample 4 and the samples (5, 6A and 6B) prepared from it.

Figure 7.8(a) presents a TEM micrograph of crystals of ZnO:Zn (sample 5) prepared from the JM sample 4 nanoparticles by firing for 45 minutes at 800°C in a reducing atmosphere. The photoluminescent emission spectrum of these ZnO:Zn nanometre sized crystals is presented in Figure 7.8(b).

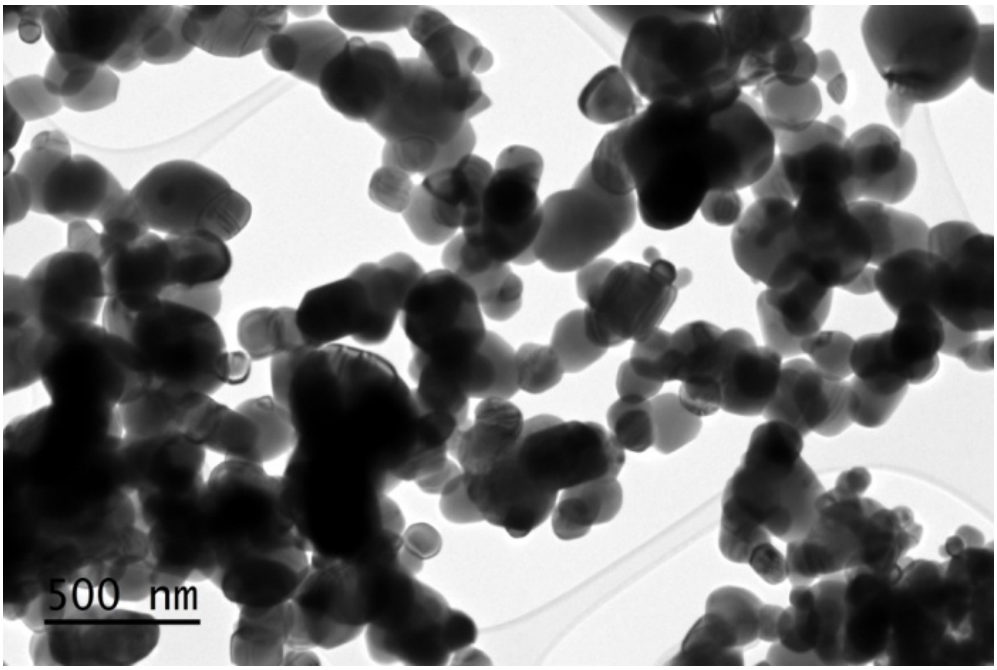

(a)

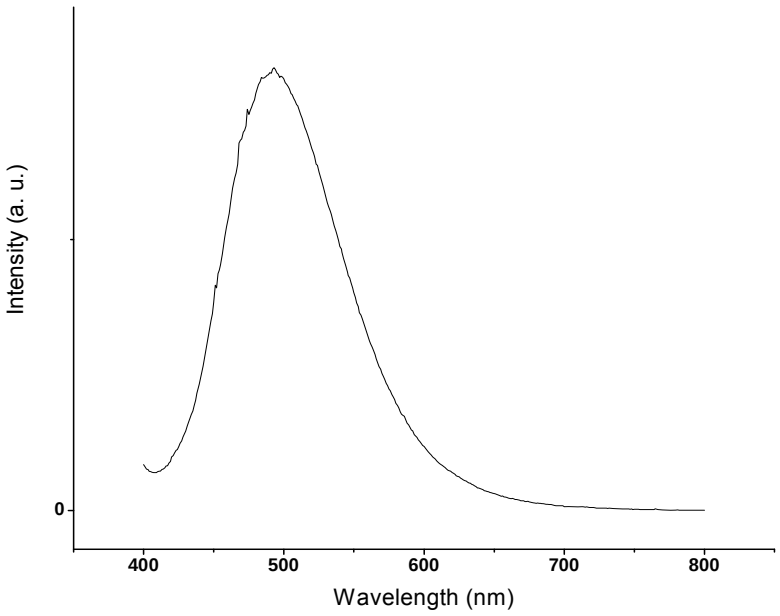

(b)

Figure 7.8 (a) TEM micrographs of crystals of ZnO:Zn (sample 5) prepared from the JM nanoparticles sample 4 by firing for 45 minutes at 800°C in a reducing atmosphere; (b) The photoluminescent emission spectrum of these ZnO:Zn nanometre sized crystals (excited at 350 nm).

Figure 7.9 presents crystals of ZnO:Zn first fired from the JM nanophosphor sample 4 then treated as in preparation 1 (see sample 6A in section 2.6). These crystals have an average crystallite size of 167.6nm (see Table 7.2). In Figure 7.9(a) the fired crystals are shown with a large amount of much smaller crystals. In Figures 9(b) and 9(c) some of the larger crystals in (a) are shown at higher magnification and there is some evidence of a coating on the larger crystals. It appears that these larger ZnO:Zn nanoparticles did not fully dissolve/react with the NH_4HCO_3 solution (1.25 M) and the 50 ml of $Al_2(SO_4)_3$ solution (0.03 M) in the time when the reaction took place. Rather they only partially dissolved and when filtered they could be seen to coexist with smaller material presumably the precipitate of the Zn^{2+} and Al^{3+} materials that formed from the surface of the ZnO:Zn crystals that did dissolve.

In Figure 7.10 the TEM micrographs of the crystals of ZnO:Zn shown in Figure 7.9 after being fired are presented (sample 6B). In Figure 7.10(a) the fired crystals are shown with a large amount of much smaller crystals. In Figures 10(b) and 10(c) some of the larger crystals in 10(a) are shown at higher magnification. In 10(b) and 10(c) there is some evidence of a coating on the larger crystals. This shows that the preparation 1 in section 2.5 does appear to work for larger nanoparticles where there is not enough acid to dissolve the larger particles, but the coating is not pure Al_2O_3 and in fact it is a ZnO layer doped with Al^{3+}.

The photoluminescent spectrum for some of these materials is presented in Figure 7.11. Clearly the luminescent properties of sample 6B were not diminished by the coating process.

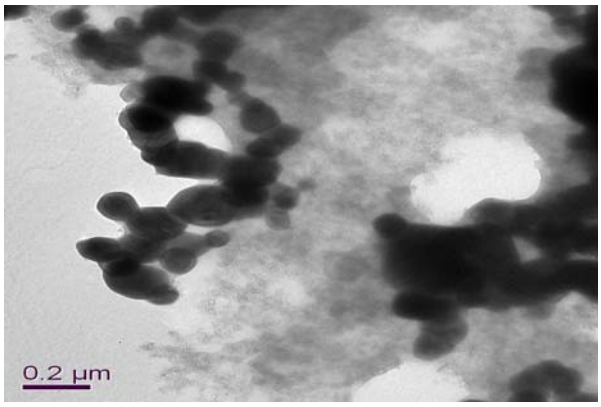

(a)

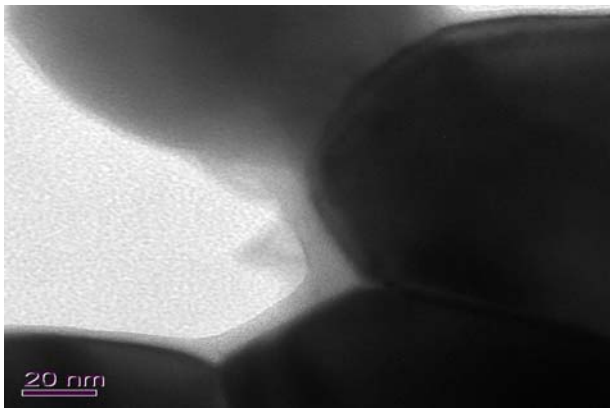

(b)

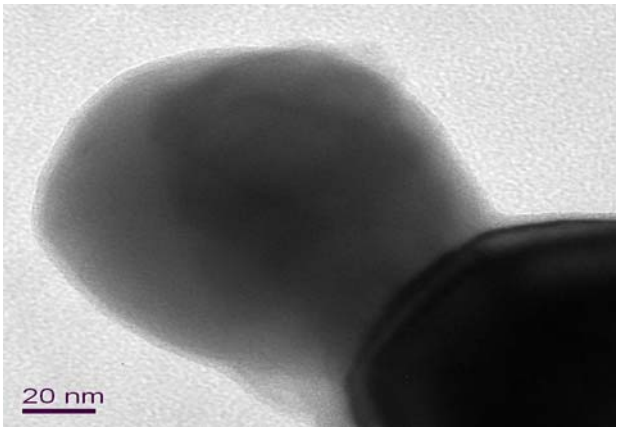

(c)

Figure 7.9 TEM micrographs of the crystals of ZnO:Zn after the procedure in preparation 1 to form sample 6A. In (a) the fired crystals are shown with a large amount of much smaller crystals. In (b) and (c) some of the larger crystals in (a) are shown at higher magnification and there is some evidence of a coating on the larger crystals.

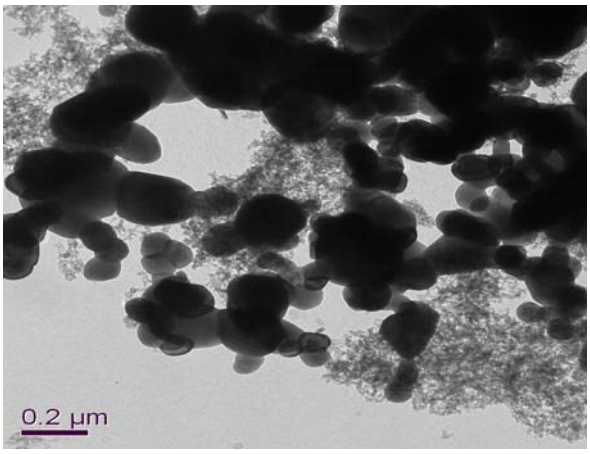

(a)

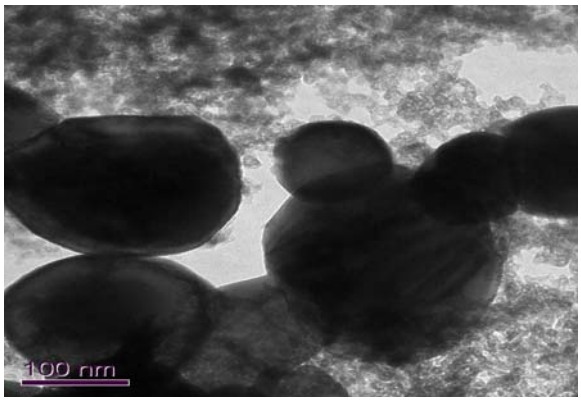

(b)

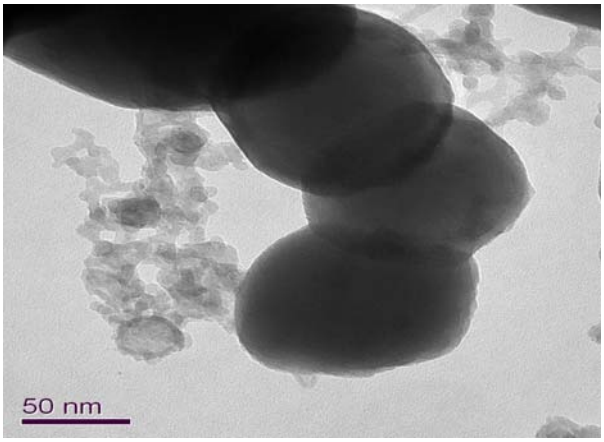

(c)

Figure 7.10 TEM micrographs of the crystals of ZnO:Zn (sample 6B) shown in Figure 7.9 after being fired at 600°C (a) the fired crystals are shown with a large amount of much smaller crystals. In (b) and (c) some of the larger crystals are shown at higher magnification, these show some evidence of a coating on the larger crystals.

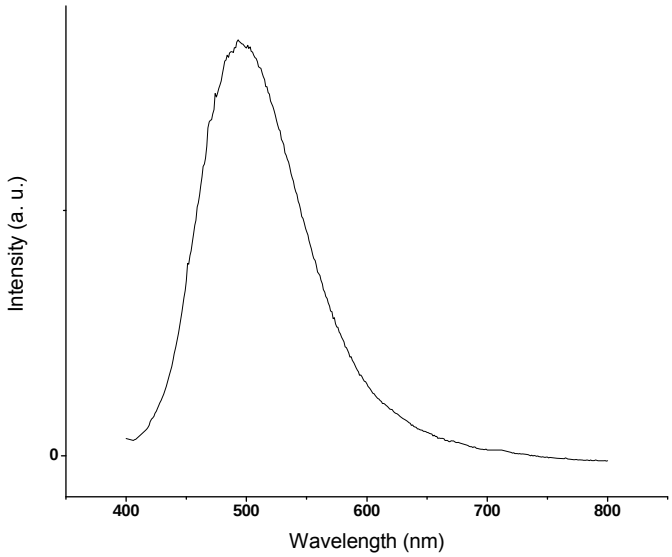

Figure 7.11 Photoluminescence emission spectrum of the ZnO:Zn (sample 6B) nanometre sized crystals (excited at 350nm) after being coated in AZO.

The unit cells, phases present and crystallite sizes found by fitting the XRPD data shown in Figure 7.7 for samples 4, 5, 6A and 6B are presented in Table 7.2. It is clear that as the particle size increases from sample 4 to sample 5, the cell size decreases in volume. As expected the cell sizes of samples 5 and 6A are the same within experimental error though the crystallite size of the latter is smaller consistent with the latter's surface reacting with the solution as described above. On firing sample 6A to form 6B the unit cell is seen to be the same within 3 standard deviations of the errors, however the crystallite size is smaller the reason for this is unclear but may be because the Al^{3+} has entered the lattice.

There was no evidence of carbonate phases in the XRPD data of sample 6A though small crystals were observed in the TEM micrographs in Figure 7.9. The reason is probably that the larger ZnO:Zn nanoparticles remaining after the reaction in solution dominate the XRPD data.

7.5 ZnO coating on large ZnO:Zn nanophosphors

Having shown it was possible to produce coated larger nanoparticles using preparation 1 in section 2.5, it was decided to explore what would happen if no $Al_2(SO_4)_3$ was used in the preparation. To do this sample 7 was prepared and then treated as explained in the experimental section to obtain samples 8A and 8B (see preparation 3 in section 2.7).

The XRPD data for these larger ZnO:Zn crystals are presented in Figure 7.12. Again as in Figure 7.7 the larger nanoparticles in this case samples 7, 8A and 8B are much sharper than those of sample 1. In addition the XRPD diffractogram for 8A in Figure 7.12 shows evidence for BCZ which arises from the ZnO:Zn nanoparticles surfaces dissolving into the solution. On firing sample 8A the BCZ is converted back to ZnO so no evidence for BCZ is found in the XRPD diffractogram for sample 8B. The cell parameters and crystalline sizes of these samples in accordance with the results in Figure 7.12 are displayed in Table 7.3.

Table 7.3 Phases present and Crystalite sizes within ZnO Nanoparticles and their products

Sample and sample number( )	**Phase present in XRPD data and lattice parameters**	**Crystal Size (nm)**
JM ZnO (Sample 1)	ZnO, *a* = 3.2525(1) Å, *c* = 5.2141(2) Å	19.32(5)
ZnO:Zn (Sample 7)	ZnO:Zn, *a* = 3.2514(1) Å, *c* = 5.2080(1) Å	175.83(95)
ZnO:Zn (Sample 8A)	ZnO:Zn, *a* = 3.2515(1) Å, *c* = 5.2084(1) Å 54.42(41)% of this material is present	212.9(31)
	$Zn_5(OH)_6(CO_3)_2$, *a* = 13.7200(52) Å, *b* = 6.3628(25) Å, *c* = 5.3742(21) Å, *β* = 97.730(38)° 45.59(41)% of this material is present	8.79(14)
ZnO:Zn coated with ZnO (Sample 8B)	ZnO, *a* = 3.2515(1) Å, *c* = 5.2085(1) Å	126.65(25)

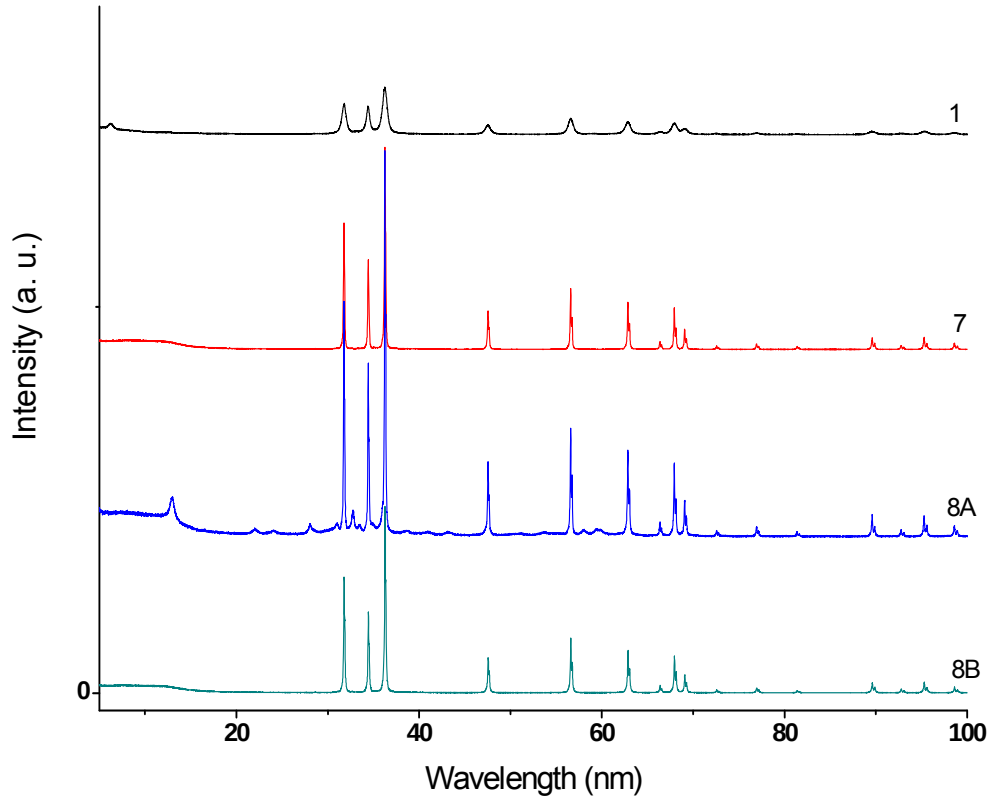

Figure 7.12 XRPD diffractograms of the ZnO nanoparticles of JM sample 1 and the samples (7, 8A and 8B) prepared from it.

In Figure 7.13 TEM micrographs of ZnO:Zn (sample 8A) prepared by first firing from the JM nanoparticles sample 1 for 45 minutes at 800°C in a reducing atmosphere (giving sample 7) then suspended in 10 ml NH_4HCO_3 solution (1.25 M) are presented. These crystals clearly show smaller pointed crystals growing from their surfaces. Obviously the ZnO:Zn crystals have reacted with the 10 ml NH_4HCO_3 to form BCZ as in the following equation:-

$$10[ZnO{:}Zn] + 4[NH_4HCO_3] + 6H_2O = 2[Zn_5(OH)_6(CO_3)_2]\downarrow + 4[(NH_4OH]$$

Note, in the equation the amount of Zn^0 in ZnO:Zn is in the order of 1mol% so it can be ignored for the purposes of the equation.

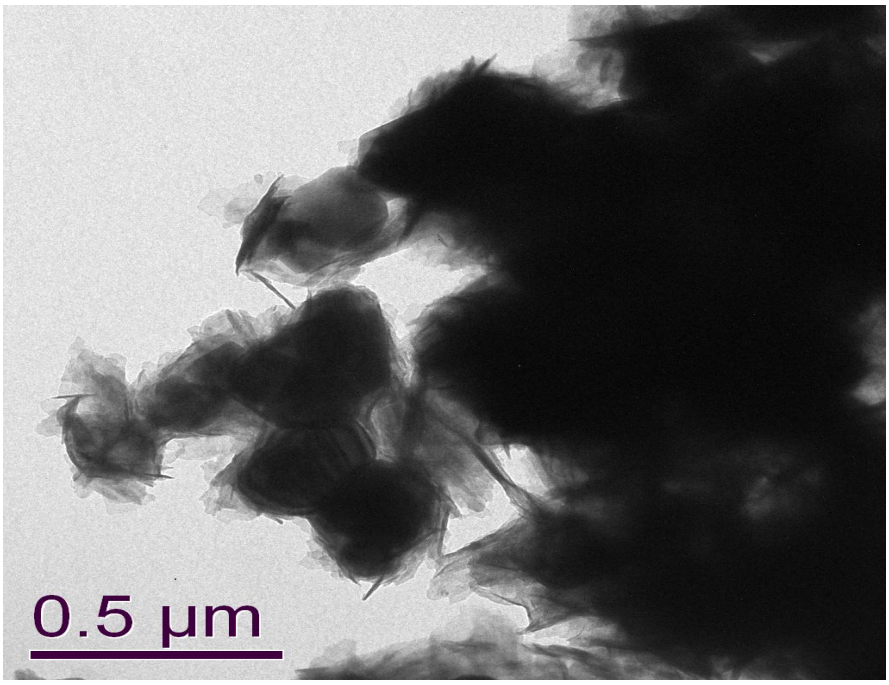

(a)

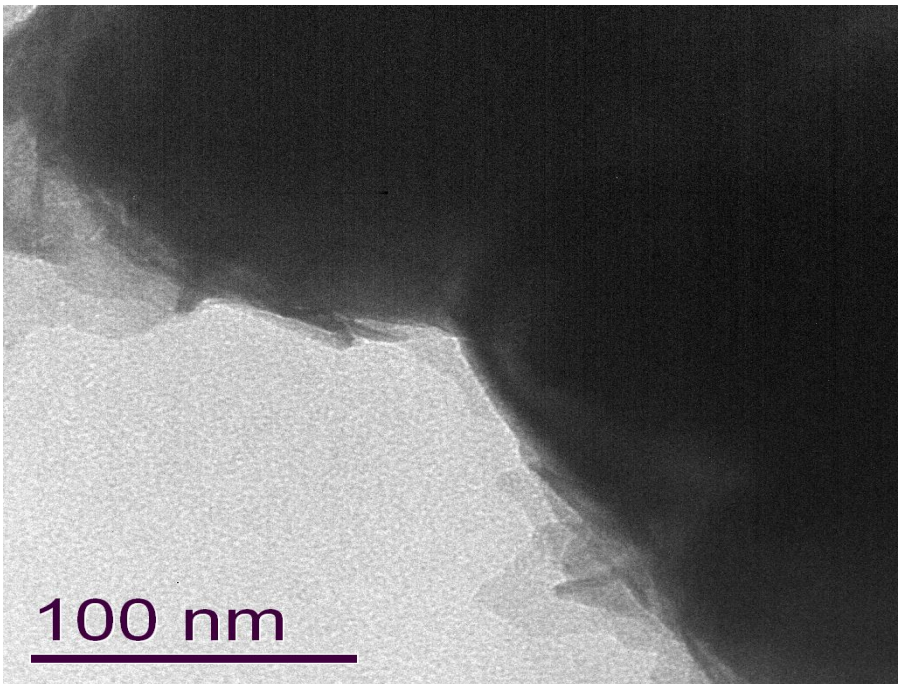

(b)

Figure 7.13 TEM micrographs of crystals of ZnO:Zn (sample 8A) first fired from the JM nanoparticles sample 1 for 45 minutes at 800°C in a reducing atmosphere then suspended in 10 ml NH_4HCO_3 solution (1.25 M). These crystals clearly show smaller pointed crystals growing from their surfaces.

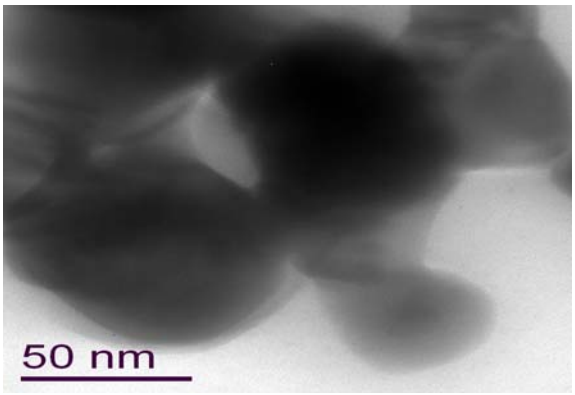

(a)

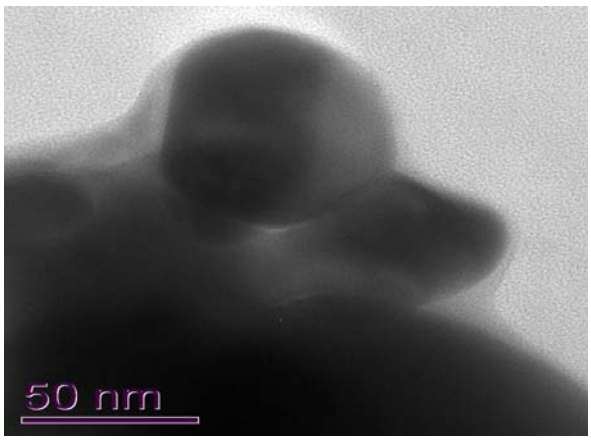

(b)

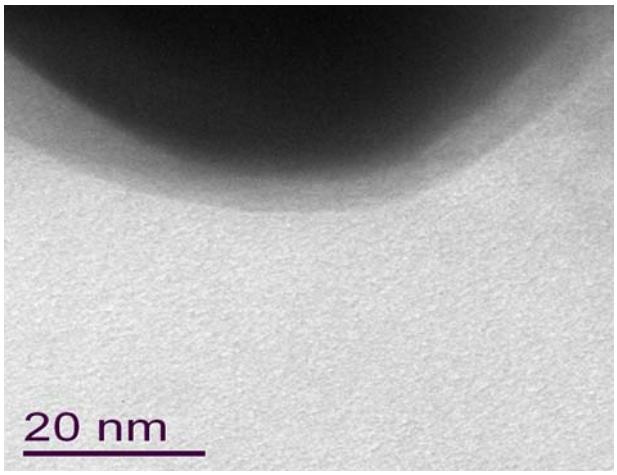

(c)

Figure 7.14 TEM micrographs of crystals of ZnO:Zn sample 8B, which was prepared by firing crystals from sample 8A (see Figure 7.13). The crystals are clearly coated.

On firing sample 8A to 600°C for 1 hour, sample 8B was produced and TEM micrographs of these crystals are presented in Figure 7.14. It is clear from Figure 7.14 that the crystals are coated with a less dense material which must be a non-crystalized form of ZnO.

Sample 8B also shows good photoluminescence properties as shown in Figure 7.15 where its excitation and emission spectra are presented. Once again it is demonstrated that these coating procedures do not disturb the photoluminescent properties of the crystal areas that do not dissolve.

The unit cells, phases present and crystallite sizes found by fitting the XRPD data shown in Figure 7.12 for samples 1, 7, 8A and 8B are presented in Table 7.3. It is clear that as the particle size increases from sample 1 to sample 7 the cell size decreases in volume in agreement with the findings from Table 7.2 for samples 4 and 5. As expected the cell sizes of samples 7 and 8A are the same within experimental error, however the crystallite size of the ZnO:Zn particles are larger in the latter sample which is inconsistent with samples 5 and 6A in Table 7.2. On firing sample 8A to form 8B the unit cell is seen to be the same, however the crystallite size is smaller than sample 7 as expected.

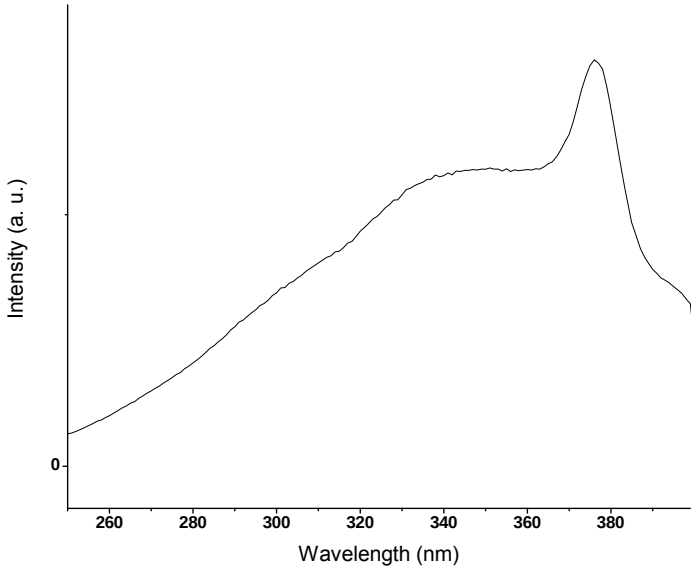

(a)

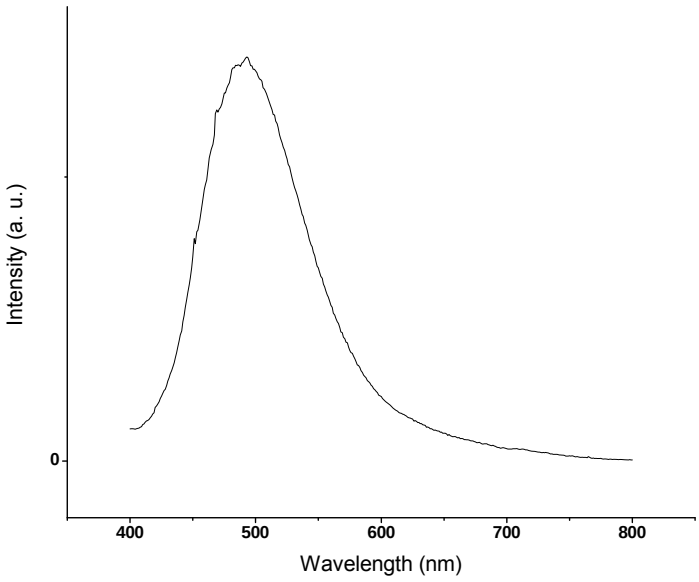

(b)

Figure 7.15 Photoluminescence (a) excitation and (b) emission spectra of the ZnO:Zn (sample 8B) nanometre sized crystals after being coated in ZnO. The excitation spectrum was monitored at 492 nm and the emission spectrum was obtained using 350 nm excitation.

7.6 AZO nanoparticles synthesis

Having shown that large nanoparticles of ZnO:Zn can be coated with AZO or ZnO using modifications of the method of Yuan et al [162]. It is then worthwhile to investigate if the method would provide a facile route for the production of small nanoparticles of AZO.

To achieve this samples of nanoparticles were prepared by dispersing nanoparticles of sample 4 in preparation 4 described in section 2.8 (Al:Zn ratios of 10wt% were used) at the higher concentrations. In this case the samples are referred to as 9A (before firing) and 9B (after firing). TEM images in Figure 7.16 show the nanoparticles of sample 9A the presence of very small particles ranging between 5 and 10 nm in size.

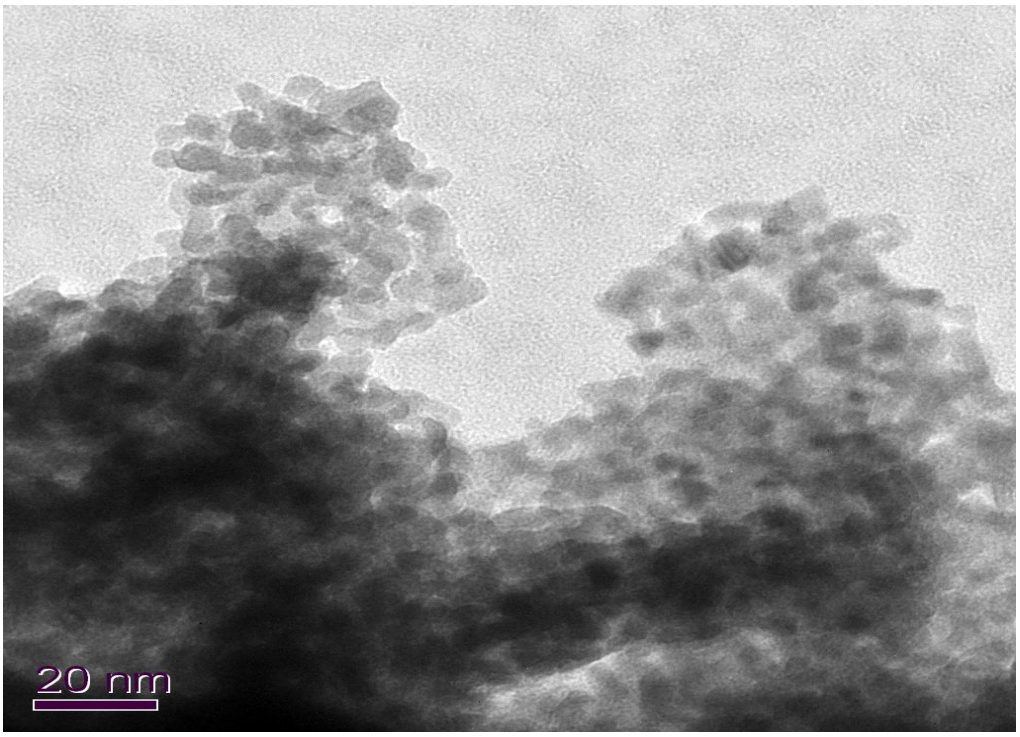

(a)

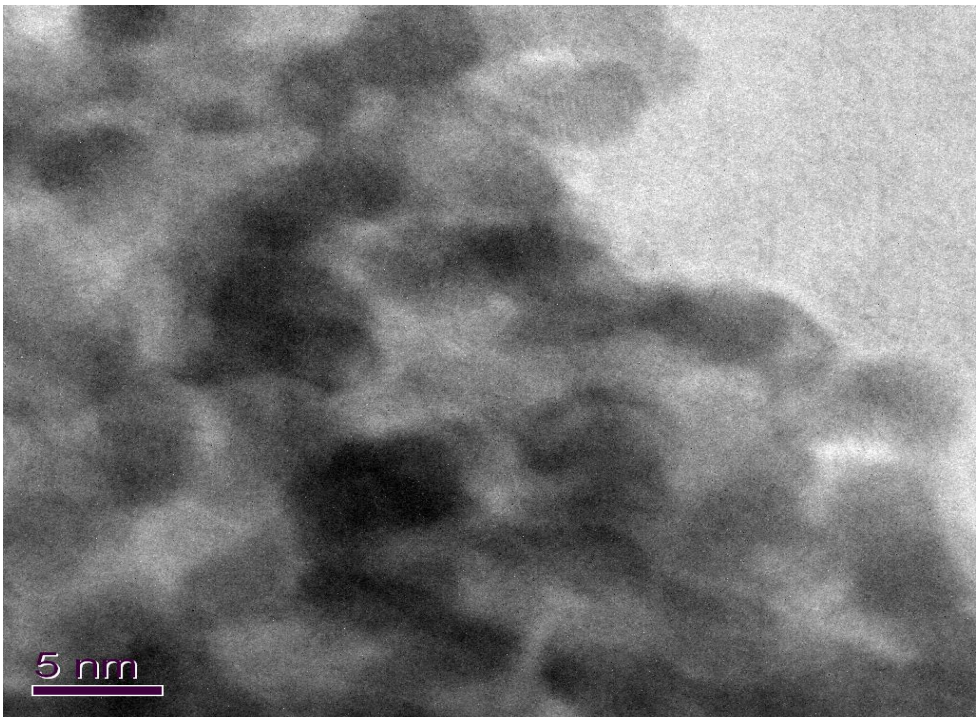

(b)

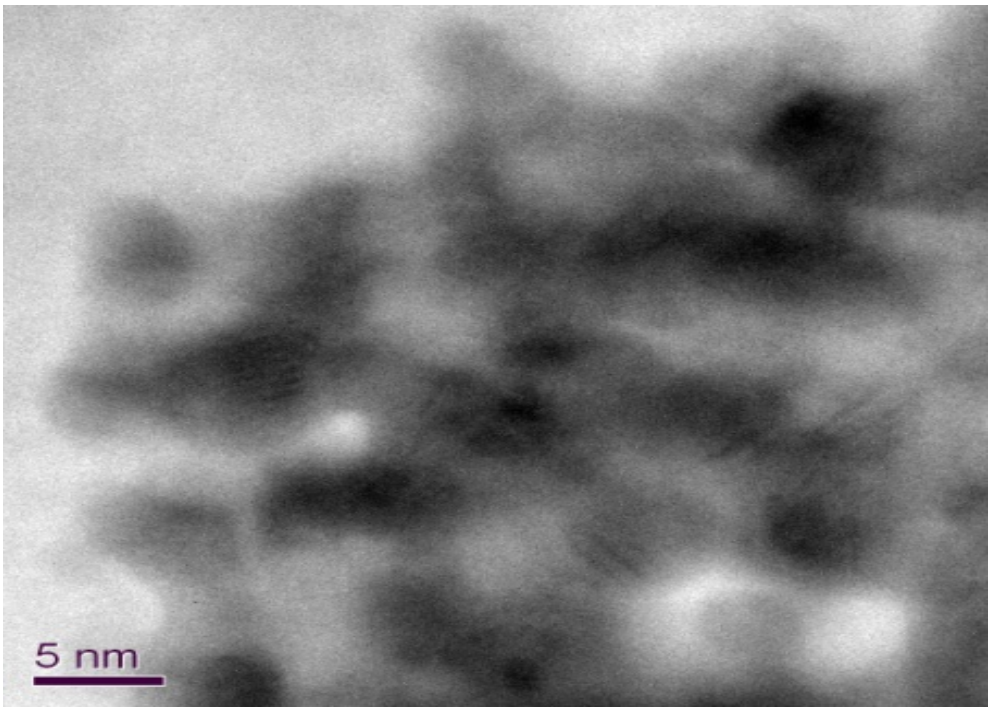

(c)

Figure 7.16 TEM micrographs of crystals of sample 9A.

From the XRPD diffractogram of sample 9A in Figure 7.17, it is apparent that these nanoparticles were BCZ and here there was no need to fit in a second material to fit the XRPD data. The cell size of the BCZ was a = 13.7200(75) Å, b = 6.3076(29) Å, c = 5.3513(24) Å, β = 97.923(36)°. After firing sample 9A to form sample 9B, there is only evidence for an AZO phase in the XRPD diffractogram in Figure 7.17.

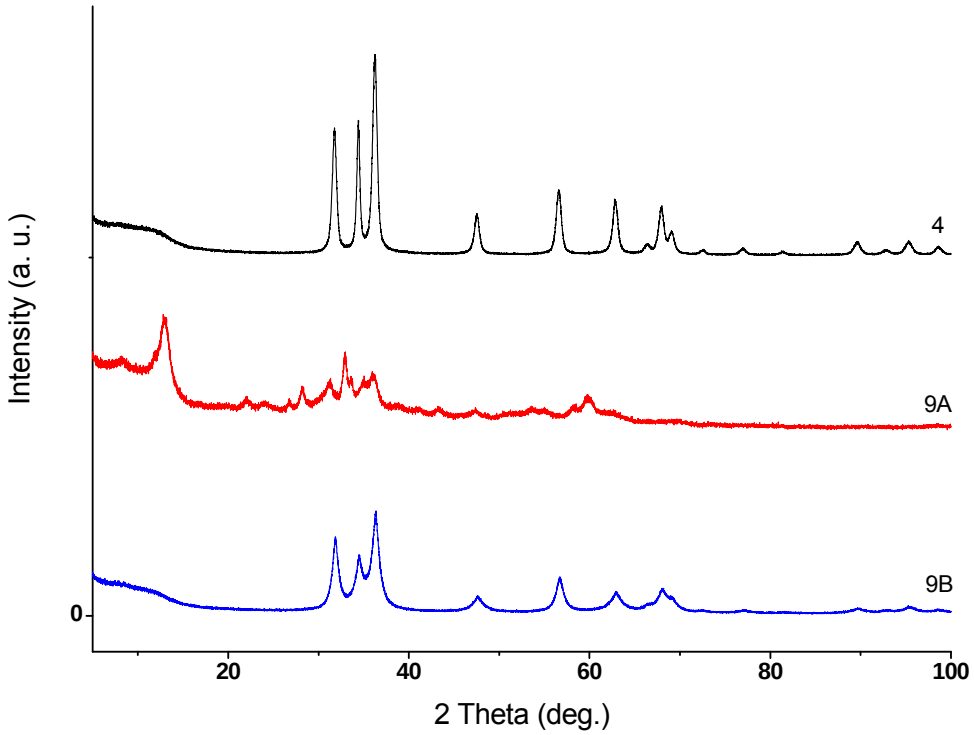

Figure 7.17 XRPD diffractograms of the ZnO nanoparticles of JM sample 4 and the samples (9A and 9B) prepared from it.

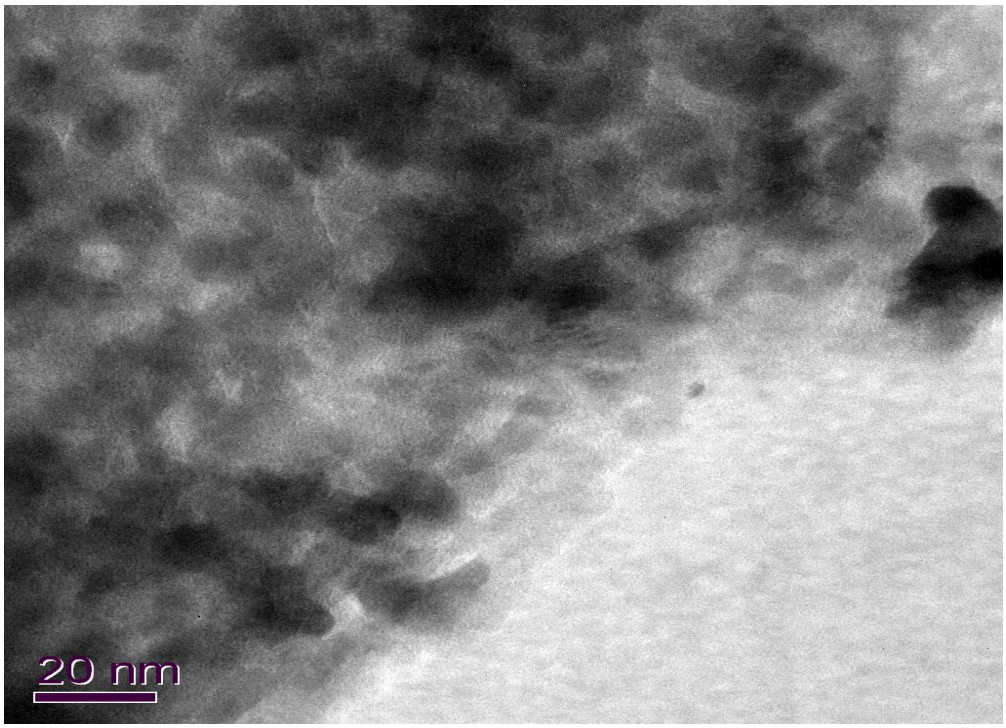

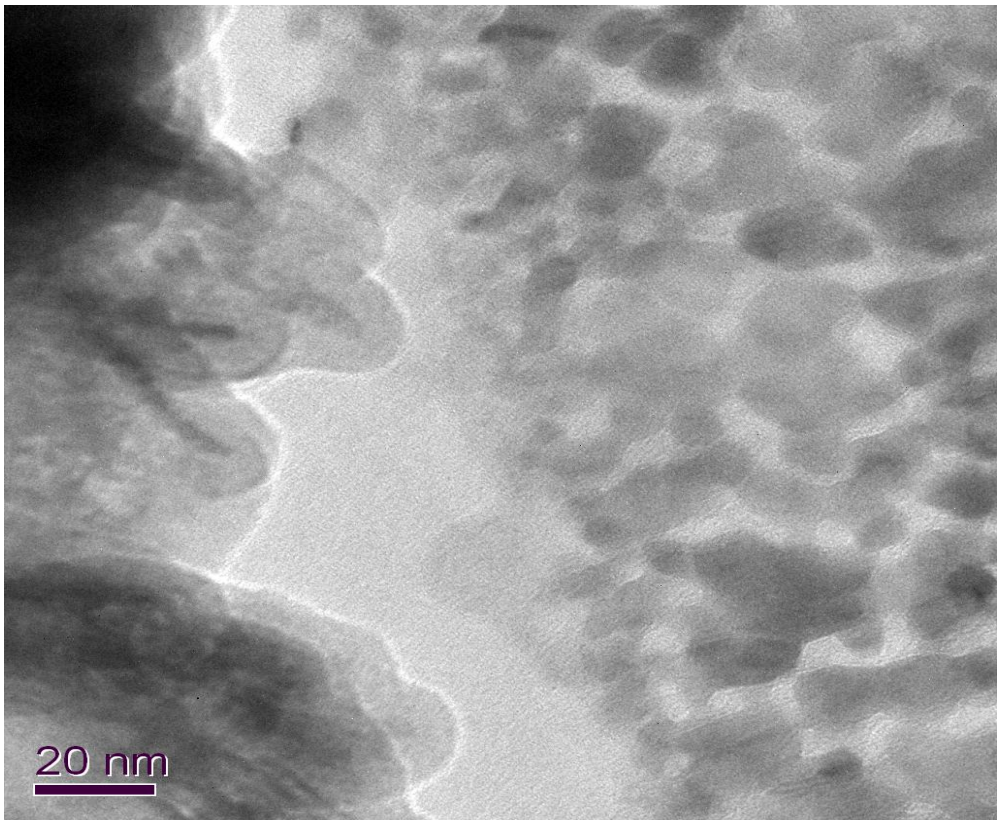

Figure 7.18 TEM micrographs of crystals of sample 9B prepared by firing sample 9A.

Figures 7.18 shows the nanoparticles of sample 9B prepared by firing sample 9A, these particles are all around 10 nm in size and have therefore not grown very much during the firing process. Their XRPD data (see Figure 7.17) are able to identify them as AZO nanoparticles. In addition the XRPD diffractogram shows further coalescence of the lines at 2Θ values of 34° and 36° compared to samples 2B and 3B in Figure 7.1 as expected for a greater Al^{3+} concentration in the AZO [303]. This evidence indicates that the Al^{3+} present in the AZO must have been present in sample 9A hence was present in the BCZ structure found for that sample and it is the final evidence that the structure can accommodate Al^{3+}. This method of preparation of AZO nanoparticles from solution is facile and produces fairly uniform particles that are very small.

In Figure 7.19, an SEM and elemental analysis maps of the sample 9B nanometre sized crystals surfaces are presented. The maps for the zinc and oxygen show elemental abundances in keeping with the crystals positions as expected. The map of the aluminium is not as detailed but clearly shows that it is spread across/through the structure and is not mainly on the surface.

A wide range of ZnO based nanostructures have been reported and many may be turned into or find uses in industrial products. It is apparent from this work that by controlling the amounts of reactants in the preparation it should be possible to coat a wide range of such ZnO nanostructures with AZO or ZnO using this method. By controlling the amount of Al^{3+} present in the reactants, coatings of AZO containing the desired Al^{3+} concentration should be easy to prepare.

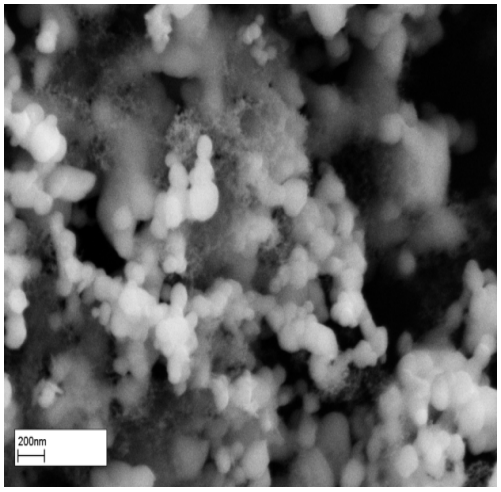

(a)

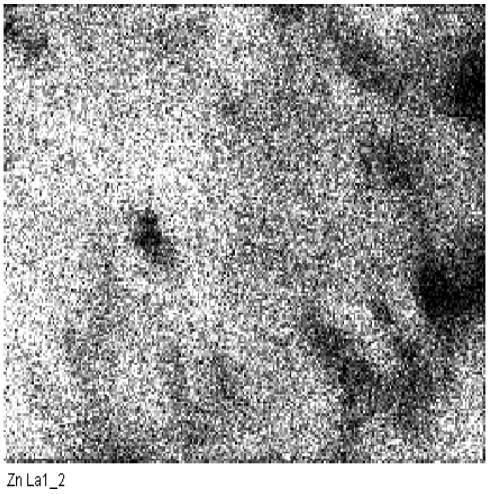

(b)

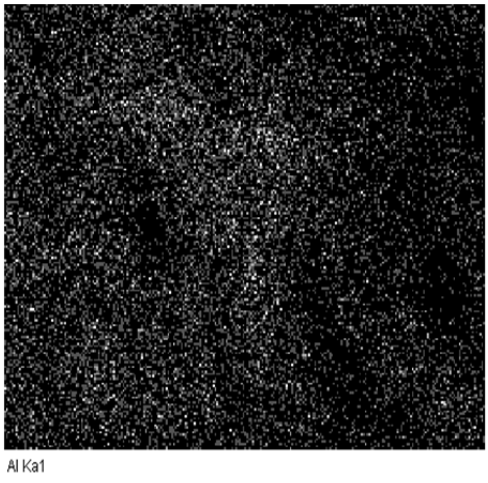

(c)

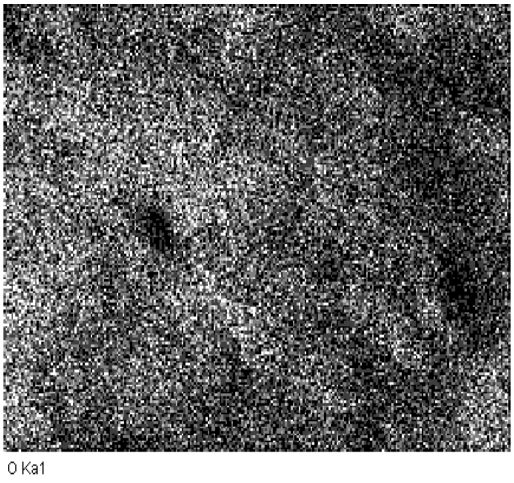

(d)

Figure 7.19 SEM of nanometre sized crystals of ZnO fired from the materials precipitated from the Al_2O_3:ZnO (10%) in the concentrated conditions (sample 9B) (a), showing the distributions of zinc (b), aluminium (c) and oxygen (d) on a silicon substrate.

7.7 Conclusions

A number of findings have been reported herein that are useful for tailoring the properties of the nanoparticles, some of which allow the nanoparticles to be coated and some do not. These are:-

1. The chemistry of the method [162] reported for the coating of zinc oxide nanoparticles with a homogeneous Al_2O_3 layer has been shown to not deliver the desired products.
2. Small nanoparticles cannot be coated using a derivative of the method as they dissolve and the products formed give rise to nanoparticles of aluminium doped ZnO that have XRPD data in agreement with previously reported AZO nanoparticles.
3. From 2 above, preparation 4 in section 2.8 reported herein is a useful way of preparing very small nanoparticles of AZO from solution rather than from a chemical vapour method [303].
4. It is possible to coat large nanoparticles of ZnO and ZnO:Zn using preparation 1 in section 2.5 but the coating is a layer of AZO not an Al_2O_3 layer.
5. It is also possible to coat large nanoparticles of ZnO:Zn with a layer of ZnO by using only $(NH_4)HCO_3$ in the absence of Al_2SO_4.
6. It has also been shown that it is possible to coat large nanoparticles of ZnO:Zn with either AZO or a layer of ZnO without destroying the luminescent properties of the phosphor sample.
7. By controlling the amounts of reactants in the preparation it should be possible to coat a wide range of ZnO nanostructures with AZO or ZnO using the chemistry reported herein.
8. It should also be possible by tailoring the amount of Al^{3+} present in the reactants, to form coatings of AZO containing any desired Al^{3+} concentration.

Chapter 8 Conclusions and Future Work

The aim of the work in this thesis arose from polymer ultraviolet degradation in outdoor uses. This work focused on the development of a range of novel polymer nanocomposites (containing inorganic nanoparticles or nanophosphors) which can down convert ultraviolet radiation into visible light or infrared thus the polymers are able to protect themselves from UV degradation or provide light emitting functionality.

The research was focused on two main areas. The first was the characterisation and the use of well crystallized nanoparticles and nanophosphors that can absorb the UV light and re-emit the light at a longer wavelength. The second one was the even distribution of these nanoparticles/nanophosphors into polymer matrices so that the polymers could maintain their transparency and also the nanofillers could still function.

Iron doped lithium aluminate ($LiAlO_2$:Fe) was the first phosphor studied. Bulk $LiAlO_2$:Fe phosphors were synthesised using a solid state reaction. Their average particle size was around 0.5 μm. The bulk phosphors were well crystallized and showed good properties of down converting the UV radiation into infrared light. The flame spray pyrolysis technique was also employed by Johnson Matthey to produce the $LiAlO_2$:Fe phosphors but in this case the phosphors were nanosized with the average particle size around 20 nm. The as-prepared $LiAlO_2$:Fe nanophosphors did not have strong excitation and emission characteristics due to their poor crystallization. However after undergoing a heat treatment at 650 °C, the nanophosphors manifested significant growth and the size was increased to approximately 100 nm along with much better crystallinity. Thereby the annealed $LiAlO_2$:Fe nanophosphors were better able to absorb the UV range from 240 to 400 nm and re-emit infrared light at the wavelength between 700 and 800 nm. In addition the

after annealing nanophosphors were embedded into polypropylene by the co-rotating twin screw extrusion technique. They were still able to manifest their photoluminescent properties which however, were to some extent modulated by the polymer.

Zinc oxide (ZnO) was also investigated. The ZnO was produced by the flame spray pyrolysis which led to very tiny and uniform particles with the particle sizes around 50 nm. High crystallinity was achieved during the synthesis procedure. It was observed that the nanosized ZnO powders strongly absorbed the UV radiation at wavelengths below 400 nm but they were highly transparent to visible light. Several methods were tried to incorporate the ZnO nanoparticles into polymers. The first trial was based on co-rotating twin screw extrusion; however this approach resulted in severe agglomerates of the ZnO nanoparticles which in turn resulted in very poor transparency of the composite. An improvement of the ZnO distribution was achieved by the spin coating technique. This preparation method provided the composite with very even dispersion of the ZnO nanoparticles. With the introduction of the ZnO, the composite did not lose any transparency in the visible light region of the electromagnetic spectrum but significantly absorbed the UV radiation. Based on such improvement, the solvent casting method was further adopted and it was found that this approach led to the composite having same characteristics as that produced by the spin coating. But here the thickness of the composite was much thicker. In fact this is a benefit because thicker surface coatings would be more beneficial as they will be more protective of the bulk polymer. This is an area where further work should be undertaken to establish optimum thickness for a given time of exposure.

Another area of research investigated in this work was based on zinc rich luminescent zinc oxide (ZnO:Zn). The ZnO:Zn nanophosphors were synthesised by firing the ZnO nanoparticles in a reducing atmosphere. The nanophosphors were grown and crystallized during the firing process. They appeared to be excited by a broad range of the UV

radiation and emitted green light with an emission peak centred at the wavelength of 500 nm. With respect to their composites, the ZnO:Zn nanophosphors were introduced into the polystyrene using the solvent casting method. The resulting composite film had extraordinarily even dispersion of the ZnO:Zn so its transparency was comparable to the virgin polystyrene film. In addition when the composite was illuminated by a UV lamp, a fairly uniform green emission could be observed and this was the evidence that the composite had maintained the down converting luminescent properties of the naked phosphor.

During the studies on the ZnO nanoparticles, a new question arose that was based on the nature of the ZnO. The question addressed here was the inherent photoconductivity of ZnO and how this property affected the surrounding polymer when ZnO was incorporated. One of the industrial partners reported that there was evidence of polymer decay in the presence of ZnO. To overcome this, a number of attempts were conducted to coat a layer of protective material on the ZnO nanoparticles by following procedures reported in the literature [162] and on methods derived from that procedure. During this work the resulted coating materials were found not to be similar to that reported. In fact the reported procedures when applied to the ZnO nanoparticles dissolved them rather than coating them. The resulted materials were characterised and found to be aluminium doped zinc oxide (ZnO:Al or AZO) nanoparticles. However when the procedures were applied on the large ZnO:Zn particles, only the surfaces of the particles were dissolved and after the firing process the particles were coated by a layer of AZO. In addition it was also demonstrated that it was feasible to produce ZnO coating on the ZnO:Zn by modifying the chemicals in the coating procedures. Therefore in this work a new approach was established to make the AZO nanoparticles and the amount of the Al^{3+} could be controlled by tailoring its amount in the reactants. The ZnO:Zn nanophosphors could also be coated by AZO or ZnO without loss of their luminescent properties. Again this work should be followed up as AZO can be very conducting and a

conducting coating could have applications for nanoparticle use in industry.

Based on the work reported in this thesis, some more future work can also be suggested. It was reported that the $LiAlO_2$:Fe, ZnO and ZnO:Zn nanoparticles (nanophosphors) could maintain their functionalities when embedded into polymers. However, the optimum loading concentrations of those nanofillers to achieve best ultraviolet absorption accompanied with high transmittance to the visible light are still unclear. Performances (such as mechanical properties and thermal stabilities) of the polymer nanocomposites need to be established. Incorporations of these nanoparticles need to be studied upon exposure to the ultraviolet radiation and in addition to be compared with polymer composites containing conventional organic UV stabilisers. These inorganic UV absorbers herein should be studied further and more evidence is required to commercialize those inorganic nanoparticles for the purpose of protecting polymers from UV degradation.

References

[1] B. Wen, F. Wang, X. F. Xu, Y. F. Ding, S. M. Zhang and M. S. Yang, *Polym. Plastics Tech. Eng.,* vol. 50, p. 1375, 2011.

[2] J. J. Condon and S. M. Ransom, "Essential Radio Astronomy: Pulsar Properties," National Radio Astronomy Observatory, 5 1 2008. [Online]. Available: http://www.cv.nrao.edu/course/astr534/Pulsars.html.

[3] A. A. Abdo and etc., *Astrophys. J.,* vol. 658, p. L33, 2007.

[4] D. H. Resnick and K. S. Krane, Physics, Wiley, 2001.

[5] K. Narisada and S. Kanaya, Phosphor Handbook: Color Vision, Taylor & Francis Group LLC., 2006.

[6] L. E. Keiner, "Microwave RF Absorbers," Coastal Carolina University, [Online]. Available: http://www.unwittingvictim.com/Absorbers.html.

[7] B. Valeur and M. N. Berberan-Santos, *J. Chem. Educ.,* vol. 88, no. 6, p. 731, 2011.

[8] J. Faist, F. Capasso, D. Sivco, C. Sirtori, A. L. Hutchinson and A. Y. Cho, *Science,* vol. 264, no. 5158, p. 553, 1994.

[9] J. W. Stouwdam and F. C. J. M. V. Veggel, *Nano Lett. ,* vol. 2, no. 7, p. 733, 2002.

[10] R. E. Bailey and S. M. Nie, *J. Am. Chem. Soc.,* vol. 125, no. 23, p. 7100, 2003.

[11] M. A. Hines and G. D. Scholes, *Adv. Mater. ,* vol. 15, no. 21, p. 1844, 2003.

[12] P. W. Barone , S. Baik, D. A. Heller and M. S. Strano, *Nature Mater.,* vol. 4, no. 1, p. 86, 2005.

[13] H. Morkoc, S. Strite, G. B. Gao, M. E. Lin, B. Sverdlov and M. Burns, *J. Appl. Phys.,* vol. 76, no. 3, p. 1363, 1994.

[14] Z. K. Tang, G. K. Wong, P. Yu, M. Kawasaki, A. Ohtomo, H. Koinuma and Y. Segawa, *Appl. Phys. Lett. ,* vol. 72, no. 25, p. 3270, 1998.

[15] M. H. Huang, S. Mao, H. Feick, H. Q. Yan, Y. Y. Wu, H. Kind, E. Weber, R. Russo and P. D. Yang, *Science,* vol. 292, no. 5523, p. 1897, 2001.

[16] T. Justel, H. Nikol and C. Ronda, *Angew. Chem. Int. Ed.,* vol. 37, p. 3084, 1998.

[17] K. Era, S. Shionoya and Y. Washizawa, *J. Phys. Chem. Solids,* vol. 29, p. 1827, 1968.

[18] K. Era, S. Shionoya, Y. Washizawa and H. Ohmatsu, *J. Phys. Chem. Solids,* vol. 29, p. 1843, 1968.

[19] G. Blasse, *J. Alloys Compd.,* vol. 225, p. 529, 1995.

[20] G. Blasse and B. C. Grabmeier, Luminescent Materials, Berlin: Springer, 1994.

[21] H. Yamamoto and H. Matsukiyo, *J. Lumin. ,* vol. 43, p. 48, 1991.

[22] C. R. Ronda, H. Bechtel, U. Kynast and T. Welker, *J. Appl. Phys.,* vol. 75, p. 4631, 1994.

[23] T. Welker, C. R. Ronda and K. J. Nieuwesteeg, *J. Electrochem. Soc.,* vol. 138, p. 602, 1991.

[24] C. R. Ronda, H. Bechtel, U. Kynast and T. Welker, *Eur. J. Solid State Inorg. Chem.,* vol. 28, p. 545, 1991.

[25] M. Sonoda, M. Takano, J. Miyahara and H. Kato, *Radiology,* vol. 148, p. 833, 1983.

[26] C. T. Schmidt, *IRE Trans. Nucl. Sci.,* vol. 7, p. 25, 1960.

[27] G. F. J. Garlick and R. A. Fatehally, *Phys. Rev.,* vol. 75, p. 1446, 1949.

[28] L. Pidol, B. Viana, A. Kahn-Harari, A. Bessiere and P. Dorenbos, *Nucl. Instrum. Methods Phys. Res. Sect. A,* vol. 537, p. 125, 2005.

[29] M. D. Birowosuto, P. Dorenbos, C. W. E. van Eijk, K. W. Kramer and H. U. Gudel, *J. Phys. Condens. Matter,* vol. 18, p. 6133, 2006.

[30] A. Bessiere, P. Dorenbos, C. W. E. van Eijk, L. Pidol, K. W. Kramer and H. U. Gudel, *Nucl. Instrum. Methods Phys. Res. Sect. A,* vol. 537, p. 242, 2005.

[31] P. Dorenbos, E. V. D. van Loef, C. W. E. van Eijk, K. W. Kramer and H. U. Gudel, *Phys. Rev. B,* vol. 68, p. 125108, 2003.

[32] S. H. M. Poort, W. P. Blokpoel and G. Blasse, *Chem. Mater. ,* vol. 7, p. 1547, 1995.

[33] J. Zhang, Z. Zhang, Z. Tang, Y. Tao and X. Long, *Chem. Mater.,* vol. 14, p. 3005, 2002.

[34] R. P. Rao, *J. Lumin. ,* vol. 113, p. 271, 2005.

[35] A. W. Veenis and A. Bril, *Phillips J. Res.,* vol. 33, p. 124, 1978.

[36] Y. Wang, X. Guo, T. Endo, Y. Murakami and M. Ushirozawa, *J. Solid State Chem.,* vol. 177, p. 2242, 2004.

[37] K. S. Sohn, C. H. Kim, J. T. Park and H. D. Park, *J. Mater. Res.,* vol. 17, p. 3201, 2002.

[38] E. van der Kolk, P. Dorenbos, C. W. E. van Eijk, H. Bechtel, T. Justel, H. Nikol, C. R. Ronda and D. U. Wiechert, *J. Lumin.,* vol. 87, p. 1246, 2000.

[39] Y. C. Kang, M. A. Lim, H. D. Park and M. Han, *J. Electrochem. Soc.,* vol. 150, p. H7, 2003.

[40] S. Nakamura, T. Mukai and M. Scnoh, *Appl. Phys. Lett.,* vol. 64, p. 1687, 1994.

[41] U. Kaufmann, M. Kunzer, K. Kohler, H. Obloh, W. Pleschen, P. Schlotter, J. Wagner, A. Ellens, W. Rossner and M. Kobusch, *Phys. Status Solidi A,* vol. 192, p. 246, 2002.

[42] S. Nakamura and G. Fasol, The Blue Laser Diode, Berlin: Springer, 1997.

[43] R. Mueller-Mach, G. Mueller, M. R. Krames, H. A. Hoppe, F. Stadler, W. Schnick, T. Justel and P. Schmidt, *Phys. Status Solidi A,* vol. 202, p. 1727, 2005.

[44] J. F. Suyver, A. Aebischer, D. Biner, P. Gemer, J. Grimm, S. Heer, K. W. Kramer, C. Reinhard and H. U. Gudel, *Opt. Mater. ,* vol. 27, p. 1111, 2005.

[45] A. Shalav, B. S. Richards, T. Trupke, K. W. Kramer and H. U. Gudel, *Appl. Phys. Lett.,* vol. 86, p. 013505, 2005.

[46] B. S. Richards and A. Shalav, *IEEE Trans. Electron Devices,* vol. 54, p. 2679, 2007.

[47] C. Feldmann, T. Justel, C. R. Ronda and P. J. Schmidt, *Adv. Funct. Mater.,* vol. 13, no. 7, p. 511, 2003.

[48] M. A. Aegerter, J. Puetz, G. Gasparro and N. Al-Dahoudi, *Opt. Mater.,* vol. 26, p. 155, 2004.

[49] C. Feldmann, *Adv. Funct. Mater.,* vol. 13, p. 101, 2003.

[50] G. Buhler and C. Feldmann, *Angew. Chem. ,* vol. 118, p. 4982, 2006.

[51] H. A. Hoppe, *Angew. Chem. Int. Ed.,* vol. 48, p. 3572, 2009.

[52] F. So, B. Krummacher, M. K. Mathai, D. Poplavskyy, S. A. Choulis and V. E. Choong, *J. Appl. Phys.,* vol. 102, p. 091101, 2007.

[53] X. Y. Huang, S. Y. Han, W. Huang and X. G. Liu, *Chem. Soc. Rev.,* vol. 42, p. 173, 2013.

[54] N. Vu, T. K. Anh, G. C. Yi and W. Strek, *J. Lumin.,* Vols. 122-123, p. 776, 2007.

[55] W. M. Yen, S. Shionoya and H. Yamamoto, Phosphor Handbook, New York: CRC Press, 2007.

[56] P. Gijsman, G. Meijers and G. Vitarelli, *Polym. Degrad. Stab.,* vol. 65, p. 433, 1999.

[57] A. Tidjani, *J. Appl. Polym. Sci.,* vol. 64, no. 13, p. 2497, 1997.

[58] W. Stevenson and J. R. White, *J. Mater. Sci.,* vol. 37, p. 1091, 2002.

[59] M. S. Rabello and J. R. White, *Polym. Degrad. Stab.,* vol. 56, p. 55, 1997.

[60] L. Audouin, V. Langlois, J. Verdu and J. C. De Bruijn, *J. Mater. Sci.,* vol. 29, p. 569, 1994.

[61] J. C. W. Chien and D. S. T. Wang , *Macromolecules,* vol. 8, p. 920, 1975.

[62] N. Martakis, M. Niaounakis and D. Pissimissis, *J. Appl. Polym. Sci. ,* vol. 51, p. 313, 1994.

[63] M. Mucha, *Colloid Polym. Sci.,* vol. 264, p. 113, 1986.

[64] R. Baumhardt-Neto and M. A. De Paoli, *Polym. Degrad. Stab.,* vol. 40, p. 59, 1993.

[65] I. L. J. Dogue, N. Mermilliod and F. Genoud, *J. Polym. Sci., Polym. Chem. Edn.,* vol. 32, p. 2193, 1994.

[66] N. C. Billingham, P. Prentice and T. Walker , *J. Polym. Sci. Symp.,* vol. 57, p. 287, 1976.

[67] N. Y. Rapoport, S. I. Berulava, A. L. Kovarskii, I. N. Musayelyan, Y. A. Yershov and V. B. Miller, *Polym. Sci. USSR,* vol. A17, p. 2901, 1975.

[68] G. Akay, T. Tincer and E. Aydin, *Eur. Polym. J.,* vol. 16, p. 597, 1980.

[69] E. M. Slobodetskaya, *Russ. Chem. Rev.,* vol. 49, p. 771, 1980.

[70] D. J. Carlsson and D. M. Wiles, *J. Macromol. Sci. Rev. Macromol. Chem.,* vol. C14, no. 1, p. 65, 1976.

[71] A. Garton, D. J. Carlsson and D. M. Wiles , *J. Polym. Sci., Polym. Chem. Edn.,* vol. 16, p. 33, 1978.

[72] A. Garton, D. J. Carlsson and D. M. Wiles, *Macromol.,* vol. 12, no. 6, p. 1071, 1979.

[73] A. Garton, D. J. Carlsson and D. M. Wiles, *Makromol. Chem.,* vol. 181, p. 1841, 1980.

[74] J. F. Rabek, Polymer Photodegradation. Mechanisms and Experimental Methods, Chapman and Hall, 1995.

[75] F. P. Miller, A. F. Vandome and J. McBrewster, Beer-Lambert Law, Alphascript Publishing, 2009.

[76] H. Books, Articles on Visiblity, Hephaestus Books, 2011.

[77] J. T. Houghton, The Physics of Atmosphere, CUP Archive, 1977.

[78] G. Geuskens and C. David, *Pure Appl. Chem.,* vol. 51, p. 233, 1979.

[79] E. T. Denisov and G. Scott, Develpments in Polymer Stabilization, Applied Science, 1982.

[80] O. Cicchetti, *Adv. Polym. Sci.,* vol. 7, p. 70, 1970.

[81] J. F. Rabek , Photostabilization of Polymers, Elsevier Applied Science, 1990.

[82] E. Niki, C. Decker and F. R. Mayo, *J. Polym. Sci.: Polym. Chem. Ed.,* vol. 11, p. 2813, 1973.

[83] C. Decker and F. R. Mayo, *J. Polym. Sci.: Polym. Chem. Ed.,* vol. 11, p. 2847, 1973.

[84] F. R. Mayo, *Macromol.,* vol. 11, p. 942, 1978.

[85] D. J. Carlsson, A. Garton and D. M. Wiles, *Macromole.,* vol. 9, no. 5, p. 695, 1976.

[86] F. Gugumus, R. Gacher and H. Muller, Plastic Additives Handbook, Hanser, 1990.

[87] G. A. Russel , *J. Am. Chem. Soc.,* vol. 79, p. 3871, 1975.

[88] H. X. Zhao and R. K. Y. Li, *Polymer,* vol. 47, p. 3207, 2006.

[89] J. Lacoste, D. Vaillant and D. J. Carlsson, *J. Polym. Sci., Part A: Polym. Chem. ,* vol. 31, p. 715, 1993.

[90] N. S. Allen and M. Edge, Fundamentals of Polymer Degradation and Stablization, Elsevier Applied Science, 1992.

[91] A. Factor, C. A. Russel and T. G. Traylor, *J. Am. Chem. Soc. ,* vol. 87, p. 3692, 1965.

[92] T. G. Traylor and C. A. Russel, *J. Am. Chem. Soc.,* vol. 87, p. 3698, 1965.

[93] A. Bandyopadhyay and G. Chandra Basak, *Mater. Sci. Tech.,* vol. 23, no. 3, p. 307, 2007.

[94] N. N. Barashkov and T. V. Sakhno, Optically Transparent Polymers and Materials Based on Them, Moscow: Khimiya, 1992.

[95] A. K. Pikaev, Modern Radiation Chemistry. The Solid State and Polymers, Moscow: Nauka, 1987.

[96] B. M. Krasovitskii and B. M. Bolotin, Organic Luminophores, Moscow: Khimiya, 1984.

[97] B. V. Grinev and V. G. Sentchishin, Plastic Scintillators, Kharkov: Akta, 2003.

[98] J. Guillet, Polymer Photophysics and Photocaemistry, Moscow: Mir, 1988.

[99] B. V. Grinev and V. G. Senchishin, Plastic Scintillators, Kharkov: Akta, 2003.

[100] R. N. Nurmukhametov, N. V. Ryzhakova, I. L. Belaits and R. Yunyaev, *Vysokomol. Soedin. B,* vol. 43, p. 1586, 2001.

[101] S. I. Kuzina and A. I. Mikhailov, *Eur. Polym. J.,* vol. 29, no. 12, p. 1589, 1993.

[102] S. I. Kuzina, A. I. Mikhailov and V. I. Gol'danskii, *Int. J. Radiat. Phys. Chem.,* vol. 8, no. 1, p. 503, 1976.

[103] R. N. Nurmukhametov, L. V. Volkova, V. G. Klimenko, S. P. Kabanov and R. V. Salov, *J. Appl. Spec.,* vol. 74, no. 6, p. 824, 2007.

[104] S. I. Kuzina and A. I. Mikhailov, *Eur. Polym. J.,* vol. 34, no. 2, p. 291, 1998.

[105] R. N. Nurmukhametov, L. V. Volkova and S. P. Kabanov, *J. Appl. Spec.,* vol. 73, no. 1, p. 55, 2006.

[106] N. Nagai, *Anal. Sci. Suppl.,* vol. 17, p. i671, 2001.

[107] N. Nagai, T. Imai, K. Terada, H. Seki, H. Okumura and H. Fujino, *Surf Interface Anal,* vol. 34, p. 545, 2002.

[108] H. Okumura, T. Takahagi, N. Nagai and S. Shingubara, *J. Polym. Sci. B,* vol. 41, p. 2071, 2003.

[109] H. Okumura, K. Takeda and N. Nagai, *J. Photopolym. Sci. Tech.,* vol. 17, p. 535, 2004.

[110] N. Nagai, H. Okumura, T. Imai and I. Nishiyama, *Polym. Degrad. Stab.,* vol. 81, p. 491, 2003.

[111] N. Nagai, T. Matsunobe and T. Imai, *Polym. Degrad. Stab.,* vol. 88, p. 224, 2005.

[112] A. Rivaton, B. Mailhot, J. Soulestin, H. Varghese and J. L. Gardette, *Polym. Degrad. Stab.,* vol. 75, p. 17, 2002.

[113] J. G. Bokria and S. Schlick, *Polymer,* vol. 43, p. 3239, 2002.

[114] M. V. Motyakin and S. Schlick, *Polym Degrad. Stab.,* vol. 76, p. 25, 2002.

[115] A. V. Shyichuk, J. R. White, I. H. Craig and I. D. Syrotynska, *Polym. Degrad. Stab.,* vol. 88, p. 415, 2005.

[116] T. Grossetete, L. Gonon and V. Verney, *Polym. Degrad. Stab.,* vol. 78, p. 203, 2002.

[117] G. Ahlblad, T. Reitberger, B. Terselius and B. Stenberg, *Polym. Degrad. Stab.,* vol. 65, p. 185, 1999.

[118] X. Jouan and J. L. Gardette, *Polym. Commun.,* vol. 28, p. 329, 1987.

[119] X. Jouan , C. Adam, D. Framageot, J. L. Gardette and J. Lemaire, *Polym. Degrad. Stab.,* vol. 25, p. 247, 1989.

[120] B. D. Sarwade and R. P. Singh, *J. Appl. Polym. Sci.,* vol. 72, p. 215, 1999.

[121] M. Celina, J. Wise, D. K. Ottesen, K. T. Gillen and R. L. Clough, *Polym. Degrad. Stab.,* vol. 68, p. 171, 2000.

[122] P. M. Ajayan, L. S. Schadler and P. V. Braun, Nanocomposite Science and Technology, New York: Wiley, 2003.

[123] I. Y. Jeon and J. B. Baek, *Materials,* vol. 3, p. 3654, 2010.

[124] J. Jordan, K. I. Jacob, R. Tannenbaum, M. A. Sharaf and I. Jasiuk, *Mater. Sci. Eng. A,* vol. 393, p. 1, 2005.

[125] M. Berta, C. Lindsay, G. Pans and G. Camino, *Polym. Degrad. Stabil.,* vol. 91, p. 1179, 2006.

[126] C. Sanchez, B. Julian, P. Belleville and M. Popall, *J. Mater. Chem.,* vol. 15, p. 3559, 2005.

[127] M. A. Osman, J. E. Rupp and U. W. Suter, *Polymer,* vol. 46, p. 8202, 2005.

[128] J. W. Cho and D. R. Paul, *Polymer,* vol. 42, p. 1083, 2001.

[129] A. Chandra, L. S. Turng, P. Gopalan, R. M. Rowell and S. Gong, *Comp. Sci. Technol.,* vol. 68, p. 768, 2008.

[130] T. Wu and Y. Ke, *Thin Solid Films,* vol. 515, p. 5220, 2007.

[131] V. Mittal, *Materials,* vol. 2, p. 992, 2009.

[132] M. Alexandre and P. Dubois, *Mater. Sci. Eng.,* vol. 28, p. 1, 2000.

[133] R. A. Vaia and E. P. Giannelis, *Macromolecules ,* vol. 30, p. 7990, 1997.

[134] M. Kawasumi, N. Hasegawa, M. Kato, A. Usuki and A. Okada, *Macromolecules,* vol. 30, p. 6333, 1997.

[135] T. D. Fornes, P. J. Yoon, H. Keskkula and D. R. Paul, *Polymer,* vol. 42, p. 9929, 2001.

[136] T. McNally, W. R. Murphy, C. Y. Lew, R. J. Turner and G. P. Brennan, *Polymer,* vol. 44, p. 2761, 2003.

[137] C. H. Davis, L. J. Mathias, J. W. Gilman, D. A. Schiraldi, J. R. Shields, P. Trulove, T. E. Sutto and H. C. Delong, *J. Polym. Sci. B Polym. Phys.,* vol. 40, p. 2661, 2002.

[138] N. Ogata, S. Kawakage and T. Ogihara, *Polymer,* vol. 38, p. 5115, 1997.

[139] H. G. Jeon, H. T. Jung, S. W. Lee and S. D. Hudson, *Polym. Bull.,* vol. 41, p. 107, 1998.

[140] R. Levy and C. W. Francis, *J. Colloid Interface Sci.,* vol. 50, p. 442, 1975.

[141] V. Krikorian and D. Pochan, *Chem. Mater.,* vol. 15, p. 4317, 2003.

[142] R. L. Parfitt and D. J. Greenland, *Clay Miner.,* vol. 8, p. 305, 1970.

[143] M. Okamoto, S. Morita, T. Kotaka and H. Tateyama, *Polymer,* vol. 41, p. 3887, 2000.

[144] M. Okamota, S. Morita and T. Kotaka, *Polymer,* vol. 42, p. 2685, 2001.

[145] K. J. Yao, M. Song, D. J. Hourston and D. Z. Luo, *Polymer,* vol. 43, p. 1017, 2002.

[146] O. C. Wilson, T. Olorunyolemi, A. Jaworski, L. Borum, D. Young, A. Siriwat, E. Dickens, E. Oriakhi and M. Lerner, *Appl. clay Sci.,* vol. 15, p. 265, 1999.

[147] C. O. Oriakhi, I. V. Farr and M. M. Lerner, *Clays Clay Miner.,* vol. 45, p. 194, 1997.

[148] P. Camargo, K. Satyanarayana and F. Wypych, *Mater. Res.,* vol. 12, p. 1, 2009.

[149] N. Suriyamurthy, B. S. Panigrahi and A. Natarajan, *Mater. Sci. Eng. A,* vol. 403, p. 182, 2005.

[150] S. E. Pratsinis, *Prog. Energy Combust Sci.,* vol. 24, p. 197, 1998.

[151] R. Strobel, A. Baiker and S. E. Pratsinis, *Adv. Powder. Technol.,* vol. 17, no. 5, p. 457, 2006.

[152] K. Hembram, D. Sivaprakasam, T. N. Rao and K. Wegner, *J. Nanopart. Res.,* vol. 15, p. 1461, 2013.

[153] A. Tricoli and T. D. Elmoe, *AIChE J.,* vol. 58, no. 11, p. 3578, 2012.

[154] J. Karthikeyan, C. C. Berndt, J. Tikkanen, J. Y. Wang, A. H. King and H. Herman, *Nanostruct. Mater.,* vol. 9, p. 137, 1997.

[155] J. Tikkanen, K. A. Gross, C. C. Berndt, V. Pitkanen, J. Keskinen, S. Raghu, M. Rajala and J. Karthikeyan, *Surf. Coat Technol.,* vol. 90, p. 210, 1997.

[156] E. K. Athanassiou, R. N. Grass and W. J. Stark, *Aerosol Sci. Technol.,* vol. 44, p. 161, 2010.

[157] W. Y. Teoh, R. Amal and L. Madler, *Nanoscale,* vol. 2, p. 1324, 2010.

[158] G. L. Chiarello, I. Rossetti and L. Forni, *J. Catal.,* vol. 236, p. 251, 2005.

[159] R. Mueller, R. Jossen, H. K. Kammler, S. E. Pratsinis and M. K. Akhtar, *AIChE J.,* vol. 50, no. 12, p. 3085, 2004.

[160] W. J. Stark, L. Madler, M. Maciejewski, S. E. Partsinis and A. Baiker, *Chem. Commun.,* p. 588, 2003.

[161] K. T. Jung and Y. C. Kang, *Mater. Lett.,* vol. 58, p. 2161, 2004.

[162] F. L. Yuan, P. Hu, Y. Ye, C. L. Yin and H. Ryu, *Mater. Sci. Eng. B,* vol. 122, p. 55, 2005.

[163] R. Dangtungee, J. Yun and P. Supaphol, *Polym. Testing,* vol. 24, p. 2, 2005.

[164] R. Dangtungee and P. Supaphol, *Polym. Testing,* vol. 27, p. 951, 2008.

[165] M. Majid, E. Hassan, A. Davoud and M. Saman, *Composite: Part B,* vol. 42, p.

2038, 2011.

[166] S. Adanur and E. Selver, *Inter. J. Polym. Mater.,* vol. 62, p. 236, 2013.

[167] B. Harieche, B. Boudine, O. Halimi, A. Fischer, A. Boudrioua and M. Sebais, *J. Optoelect. Adv. Mater.,* vol. 13, no. 6, p. 693, 2011.

[168] B. Jaleh, M. Shayegani Madad, M. Farshchi Tabrizi, S. Habibi, R. Golbedaghi and M. R. Keymanesh, *J. Iran. Chem. Soc.,* vol. 8, p. 161, 2011.

[169] P. P. Jeeju, A. M. Sajimol, V. G. Sreevalsa, S. J. Varma and S. Jayalekshmi, *Polym. Int.,* vol. 60, p. 1263, 2011.

[170] P. P. Jeeju and S. Jayalekshmi, *J. Appl. Polym. Sci.,* vol. 120, p. 1361, 2011.

[171] N. Alemdar, B. Karagoz, A. T. Erciyes and N. Bicak, *J. Appl. Polym. Sci.,* vol. 116, p. 165, 2010.

[172] D. W. Chae and B. C. Kim, *Polym. Adv. Technol. ,* vol. 16, p. 846, 2005.

[173] M. A. Aegerter and M. Menning, Sol-gel technologies for glass producers and users, Boston: Kluwer Academic , 2004.

[174] L. E. Scriven, *MRS Proceedings,* vol. 121, 1988.

[175] U. Siemann, *Progr. Colloid Polym. Sci.,* vol. 130, p. 1, 2005.

[176] S. Zhang, L. Li and A. Kumar, Materials Characterization Techniques, CRC Press, 2009.

[177] E. Smith and G. Dent, Modern Raman Spectroscopy - A Practical Approach, John Wiley & Sons, 2005.

[178] K. Ueda, N. Hirosaki, Y. Yamamoto, A. Naito, T. Nakajima and H. Yamamoto, *Electochem. Solid State Lett.,* vol. 9, no. 4, p. 22, 2006.

[179] Y.-H. Tseng, B. Chiou, C. Peng and L. Ozawa, *Thin Solid Films,* vol. 330, p. 173, 1998.

[180] W. J. Tang and D. H. Chen, *Mater. Res. Bull.,* vol. 44, p. 836, 2009.

[181] J. Zhang, Z. Zhang, Z. Tang, Y. Lin and Z. Zheng, *J. Mater. Proc. Tech.,* vol. 121, p. 265, 2002.

[182] M. Aoyama, Y. Amano, K. Inoue, S. Honda, S. Hashimoto and Y. Iwamoto, *J. Lumin.,* vol. 135, p. 211, 2013.

[183] J. Silver, R. Withnall, R. Li, A. Lipman, P. J. Marsh, G. R. Fern, K. Tarverdi, P. Bishop and B. Thiebaut, *Proc. IDW,* vol. 3, p. 1409, 2011.

[184] S. Hashimoto, K. Hattori, K. Inoue, A. Nakahashi, S. Honda and Y. Iwamoto, *Mater. Res. Bull.,* vol. 44, p. 70, 2009.

[185] M. Marezio, *Acta. Cryst.,* vol. 19, p. 396, 1965.

[186] M. Marezio and J. P. Remeika, *J. Chem. Phys.,* vol. 44, no. 9, p. 3348, 1966.

[187] N. T. Melamed, P. J. Viccaro, J. O. Artman, F. De and S. Barros, *J. Lumin,* Vols. 1-2, p. 348, 1970.

[188] T. Abitta, F. De, S. Barros and N. T. Melamed, *J. Lumin.,* vol. 33, p. 141, 1985.

[189] S. S. Pitale, V. Kumar, I. Nagpure, O. M. Ntwaeaborwa and H. C. Swart, *Current Appl. Phys.,* p. 1, 2010.

[190] V. Singh, R. Chakradhar, J. L. Rao and H. Y. Kwak, *Solid State Sci.,* vol. 11, p. 870, 2009.

[191] S. Kuck, S. Hartung, K. Petermann and G. Huber, *Appl. Phys. B,* vol. 61, p. 33, 1995.

[192] S. Kuck and S. Hartung, *Chem. Phys.,* vol. 240, p. 387, 1999.

[193] M. Yamaga, J. Wells, M. Honda, T. Han and B. Henderson, *J. Lumin.,* vol. 108, p. 313, 2004.

[194] M. Aoyama, Y. Amano, K. Inoue, S. Honda and S. Hashimoto, *J. Lumin.,* vol. 136, p. 411, 2013.

[195] M. G. Brik, H. Teng, H. Lin, S. Zhou and N. M. Avram, *J. Alloy Compd.,* vol. 506, p. 4, 2010.

[196] T. Kutty and M. Nayak, *Mater. Res. Bull.,* vol. 34, no. 2, p. 249, 1999.

[197] R. Dronskowski, *Inorgan. Chem.,* vol. 32, no. 1, 1993.

[198] Z. Weyberg, *Zbl. Mineralog,* p. 645, 1906.

[199] K. R. Poeppelmeier, C. K. Chiang and D. O. Kipp, *Inorg. Chem.,* vol. 27, p. 4523, 1988.

[200] M. Marezio, *Acta. Crystallogr.,* vol. 18, p. 481, 1965.

[201] E. F. Bertaut, A. Delapalme, G. Bassi, A. D. Burif-Varambon and J. C. Joubert, *Bull. Soc. Fr. Miner. Cristallogr.,* vol. 88, p. 103, 1965.

[202] K. Kinoshita, J. W. Sim and J. P. Ackerman, *Mater. Res. Bull.,* vol. 13, p. 445, 1978.

[203] J. Beceril, P. Bosch and S. Bulbulian, *J. Nucl. Mater.,* vol. 185, p. 304, 1991.

[204] M. M. Chou, H. C. Huang, D. S. Gan and C. W. Hsu, *J. Cryst. Growth,* vol. 291, p. 485, 2006.

[205] J. Zou, S. M. Zhou, J. Xu, L. H. Zhang, Z. L. Xie, P. Han and R. Zhang, *J. Appl. Phys.,* vol. 98, p. 084909, 2005.

[206] J. Zou and W. D. Xiang, *J. Crys. Growth,* vol. 311, p. 3285, 2009.

[207] T. Avalos-Rendon, J. Casa-Madrid and H. Pfeiffer, *J. Phys.Chem. A,* vol. 113, no. 25, p. 6919, 2009.

[208] P. V. Korake and A. G. Gaikwad, *Frontiers of Chemical Engineering in China,* vol. 5, no. 2, p. 215, 2011.

[209] T. Avalos-Rendon, V. H. Lara and H. Pfeiffer, *Industrial and Engineering Chemistry Research,* vol. 51, no. 6, p. 2622, 2012.

[210] Y. Wang, J. Liu, M. Kan and Z. Liu, *Adv. Mater. Research ,* vol. 669, p. 115, 2013.

[211] P. Pasierb, S. Komornicki, M. Rokita and M. Rekas, *J. Mole. Struc.,* vol. 596, p. 151, 2001.

[212] H. J. Song and S. H. Lee, *Nanotechnology,* vol. 18, p. 055402, 2007.

[213] R. F. Li, C. F. Cai, L. Hu, H. Z. Wu, W. H. Zhang and J. F. Zhu, *Appl. Surf. Sci.,* vol. 276, p. 258, 2013.

[214] Y. Li, B. P. Zhang, J. X. Zhao, H. Z. Ge, X. K. Zhao and L. Zou, *Appl. Surf. Sci.,* vol. 279, p. 367, 2013.

[215] L. Bergman and J. L. McHale, Handbook of Luminescent Semiconductor Materials, CRC Press, 2012.

[216] Y. B. Hahn, *Korean J. Chem. Eng.,* vol. 28, no. 9, p. 1797, 2011.

[217] R. Mochinaga, T. Yamasaki and T. Arakawa, *Sensor Actuators B,* vol. 52, p. 96, 1998.

[218] D. Gal, G. Hodes, D. Lincot and H. Schok, *Thin Solid Films,* vol. 79, p. 361, 2000.

[219] D. Lincot, *Actualite Chimique (May),* p. 23, 1999.

[220] C. W. Nahm and C. H. Park, *J. Mater. Sci.,* vol. 35, p. 3037, 2000.

[221] T. Pauporte and D. Liincot, *Electrochim. Acta.,* vol. 45, p. 3345, 2000.

[222] M. Pineda, J. Palacios, L. Alonso, E. Garcia and R. Moliner, *Fuel,* vol. 79, p. 885, 2000.

[223] M. Turkoglu and S. Yener, *Int. J. Cosmet. Sci.,* vol. 19, p. 193, 1997.

[224] M. Mitchnick, D. Fairhurst and S. Pinnell, *J. Am. Acad. Dermtol. ,* vol. 40, p. 85, 1999.

[225] T. Iwasaki, M. Satoh, T. Masuda and T. Fujita, *J. Mater. Sci. ,* vol. 35, p. 4025, 2000.

[226] R. J. Hannick and A. Hill, Nanostructure Control of Materials, Cambridge: Woodhead Publishing Ltd., 2006.

[227] M. J. Osmond and M. J. Mccall, *Nanotoxicology,* vol. 4, p. 15, 2010.

[228] P. J. Perez Espitia, N. d. F. Ferreira Soares, J. S. d. Reis Coimbra, N. J. d. Andrade, R. Souza Cruz and E. A. Alves Medeiros, *Food Bioprocess Technol.,* vol. 5, p. 1447, 2012.

[229] Z. L. Wang, *Mater. Today,* p. 26, 2004.

[230] S. J. Pearton, D. P. Norton, K. Ip, Y. W. Heo and T. Steiner, *Superlatt. Microstruct.,* vol. 34, p. 3, 2003.

[231] T. Zhang, W. Dong, M. K. Brewer, S. Konar, R. N. Njabon and Z. R. Tian, *J. Am. Chem. Soc.,* vol. 128, p. 10960, 2006.

[232] G. C. Yi, C. Wang and W. II Park, *Semicond. Sci. Technol.,* vol. 20, p. S22, 2005.

[233] E. K. Goharshadi, M. Abareshi, R. Mehrkhah, S. Samiee, M. Moosavi, A. Youssefi and P. Nancarrow, *Mater. Sci. Semiconduct. Processing,* vol. 14, p. 69, 2011.

[234] G. Shen, D. Chen and C. J. Lee, *J. Phys. Chem. B,* vol. 110, p. 15689, 2006.

[235] A. Eftekhari, F. Molaei and H. Arami, *Mater. Sci. Eng. A,* vol. 437, p. 446, 2006.

[236] G. Shen, J. H. Cho, J. K. Yoo, G. C. Yi and C. J. Lee, *J. Phys. Chem. B,* vol. 109, p. 5491, 2005.

[237] B. P. Zhang, N. T. Binh, K. Wakatsuki, Y. Segawa, Y. Yamada, N. Usami, M. Kawasaki and H. Koinuma, *Appl. Phys. Lett.,* vol. 84, p. 4098, 2004.

[238] J. Liu, P. X. Gao, W. J. Mai, C. S. Lao, Z. L. Wang and R. Tummala, *Appl. Phys. Lett.,* vol. 89, p. 63125, 2006.

[239] Z. Y. Fan and J. G. Lu, *J. Nanosci. Nanotechnol.,* vol. 5, no. 10, p. 1561, 2005.

[240] R. Kaur, A. V. Singh, K. Sehrawat, N. C. Mehra and R. M. Metra, *J. Non-Cryst. Sol.,* vol. 352, no. 23, p. 2565, 2006.

[241] A. Dev, S. K. Panda, S. Kar, S. Chakrabarti and S. Chaudhuri, *J. Phys. Chem. B,* vol. 110, p. 14266, 2006.

[242] A. Sekar, S. H. Kim, A. Umar and Y. B. Hahn, *J. Cryst. Growth,* vol. 277, p. 471, 2005.

[243] A. Umar, S. H. Kim, Y. S. Lee, K. S. Nahm and Y. B. Hahn, *J. Cryst. Growth,* vol. 282, p. 131, 2005.

[244] B. Cao, Y. Li, G. Duan and W. Cai, *Cryst. Growth Design,* vol. 6, p. 1091, 2006.

[245] X. Wu, G. Lu, C. Li and G. Shi, *Nanotechnology,* vol. 17, p. 4936, 2006.

[246] W. Lee, H. G. Sohn and M. Myoung, *Mater. Sci. Forum,* vol. 449, p. 1245, 2004.

[247] B. Liu and H. C. Zeng, *J. Am. Chem. Soc.,* vol. 125, p. 4430, 2003.

[248] J. M. Wang and L. Gao, *J. Mater. Chem.,* vol. 13, p. 2551, 2003.

[249] S. Kar, A. Dev and S. Chaudhuri, *J. Phys. Chem. B,* vol. 110, p. 17848, 2006.

[250] C. K. Xu, G. D. Xu, Y. K. Liu and G. H. Wang, *Solid Sate Commun.,* vol. 122, p. 175, 2002.

[251] A. A. Balandin and K. L. Wang, Handbook of Semiconductor Nanostructures and Nanodevices, American Scientific Publishers, 2005.

[252] H. S. Nalwa, Encyclopedia of Nanoscience and Nanotechnology, American Scientific Publishers, 2011.

[253] R. R. Reeber, *J. Appl. Phys.,* vol. 41, p. 5063, 1970.

[254] O. Dulub, L. A. Boatner and U. Diebold, *Surf. Sci. ,* vol. 519, p. 210, 2002.

[255] W. J. Li, E. W. Shi, W. Z. Zhong and Z. W. Yin, *J. Cryst. Growth ,* vol. 203, p. 186,

1999.

[256] J. C. Phillips, Bonds and Bands in Semiconductors, New York: Academic Press, 1973.

[257] S. M. Soosen, B. Lekshmi and K. C. George , *SB Acad. Rev.,* vol. XVI, p. 57, 2009.

[258] R. K. Hailstone, A. G. DiFrancesco, J. G. Leong, T. D. Allston and K. J. Reed, *J. Phys. Chem. C,* vol. 113, p. 15155, 2009.

[259] R. Yousefi, A. K. Zak and F. Jamali-Sheini, *Ceramics International ,* vol. 39, p. 1371, 2013.

[260] D. B. Hall, P. Underhill and J. M. Torkelson, *Poly. Eng. Sci.,* vol. 38, no. 12, p. 2039, 1998.

[261] L. V. Azaroff, Introduction to Solids, New York: McGraw-Hill, 1960.

[262] X. Zhang, Y. H. Cheng, L. Y. Li, H. Liu, X. Zuo, G. H. Wen, L. Li, R. K. Zheng and S. P. Ringer, *Phys. Rev. B,* vol. 80, p. 174427, 2009.

[263] H. S. Kang, J. S. Kang, J. W. Kim and S. Y. Lee, *J. Appl. Phys.,* vol. 95, no. 3, p. 1246, 2004.

[264] S. Nakamura, The Blue LaserDiode, New York: Springer, 1997.

[265] M. Ramani, S. Ponnusamy and C. Muthamizhchelvan, *Optical Mater.,* vol. 34, p. 817, 2012.

[266] O. D. Jayakumar, V. Sudarsan, C. Sudakar, R. Naik, R. K. Vatsa and A. K. Tyagi, *Scripta Materialia,* vol. 62, p. 662, 2010.

[267] H. K. Yadav, K. Sreenivas and V. Gupta, *J. Mater. Res.,* vol. 22, no. 9, p. 2404, 2007.

[268] W. Li, D. S. Mao, F. M. Zhang, X. Wang, X. H. Liu, S. C. Zou, Y. K. Zhu, Q. Li and J. F. Xu, *Nuclear Instruments and Methods in Physics Research B,* vol. 169, p. 59, 2000.

[269] P. T. Hsieh, Y. C. Chen, K. S. Kao and C. M. Wang, *Physics B,* vol. 178, p. 403, 2008.

[270] X. L. Wu, G. Siu, C. L. Fu and H. C. Ong, *Appl. Phys. Lett.,* vol. 78, p. 2285, 2001.

[271] K. Vanheusden, W. L. Warren, C. H. Seager, D. R. Tallant, J. A. Voigt and B. E. Gnade, *J. Appl. Phys.,* vol. 79, p. 7983, 1996.

[272] K. Vanheusden, C. H. Seager, W. L. Warren, D. R. Tallant and J. A. Voigt, *Appl.*

Phys. Lett. , vol. 68, p. 403, 1995.

[273] S. A. Studenikin, N. Golego and M. Cocivera, *J. Appl. Phys. ,* vol. 84, p. 2287, 1998.

[274] H. S. Kang, J. S. Kang, J. W. Kim and S. Y. Lee, *J. Appl. Phys,* vol. 95, p. 1246, 2003.

[275] B. Lin, Z. Fu and Y. Jia, *Appl. Phys. Lett.,* vol. 79, p. 943, 2001.

[276] U. Ozgur, Y. I. Alivov, C. Liu, A. Teke, M. A. Reshchikov, S. Dogan, V. Avrutin, S. J. Cho and H. Morkoc, *J. Appl. Phys.,* vol. 98, p. 041301, 2005.

[277] Q. X. Zhao, P. Klason, M. Willander, H. M. Zhong, W. Lu and J. H. Yang, *Appl. Phys. Lett.,* vol. 87, p. 211912, 2005.

[278] A. F. Kohan, G. Ceder, D. Morgan and C. G. Van de Walle, *Phys. Rev. B,* vol. 61, p. 15019, 2000.

[279] M. Liu, A. H. Kitai and P. Mascher, *J. Lumin.,* vol. 54, p. 35, 1992.

[280] E. G. Bylander, *J. Appl. Phys.,* vol. 49, p. 1148, 1978.

[281] C. D. Li, J. P. Lv and Z. Q. Liang, *J. Mater. Sci.: Mater. Electron,* vol. 23, p. 1673, 2012.

[282] N. Y. Garces, L. Wang, L. Bai, N. C. Giles, L. E. Halliburton and G. Cantwell, *Appl. Phys. Lett.,* vol. 81, p. 622, 2002.

[283] V. Rakhesh, M. Junaid Bushiri and V. K. Vaidyan, *J. Optoelectron. Adv. Mater.,* vol. 9, no. 12, p. 3740, 2007.

[284] F. Oba, S. R. Nishitani, S. Isotani, H. Adachi and I. Tanaka, *J. Appl. Phys.,* vol. 90, p. 824, 2001.

[285] J. Silver and R. Withnall, “Protection of Plastics”. US Patent 2010307055, 9 12 2010.

[286] M. S. Gaur, P. K. Singh and R. S. Chauhan, *J. Appl. Polym. Sci.,* vol. 118, p. 2833, 2010.

[287] Q. H. Chen, S. Y. Shi and W. G. Zhang, *Colloid. Polym. Sci.,* vol. 287, p. 533, 2009.

[288] R. Yang, P. A. Christensen, T. A. Egerton and J. R. White, *Polym. Degrad. Stab.,* vol. 95, p. 1533, 2010.

[289] C. H. Xue, W. Yin, P. Zhang, J. Zhang, P. T. Ji and S. T. Jia, *Colloids Surf. A: Physicochem. Eng. Aspects,* vol. 427, no. 20, p. 7, 2013.

[290] R. Li, G. R. Fern, R. Withnall, J. Silver, P. Bishop and B. Thiebaut, *MRS Procedings,* vol. 1509, 2013.

[291] S. D. Kshirsagar, U. P. Shaik, M. G. Krishna and S. P. Tewari, *J. Lumin.,* vol. 136, p. 26, 2013.

[292] A. P. Alivisatos, *MRS Bull.,* vol. 20, p. 23, 1995.

[293] A. P. Alivisatos, *Science,* vol. 271, p. 933, 1996.

[294] A. P. Alivisatos, *Endeavour,* vol. 21, p. 56, 1997.

[295] A. P. Alivisatos, *NATO Sci. Ser. C,* vol. 519, p. 405, 1999.

[296] P. Gijsman, J. Hennekens and D. Tummers, *Polym. Degrad. Stab.,* vol. 39, p. 225, 1993.

[297] R. Withnall, J. Silver, R. Stone, R. Li, A. Lipman, P. J. Marsh, G. R. Fern, K. Tarverdi, P. Bishop and B. Thiebaut, *Proceedings of the 3rd International Conference on Nanopolymers,* p. 1, 2011.

[298] J. Silver, R. Withnall, G. R. Fern, R. Li, A. Lipman, C. Catherall, A. Salimian, P. G. Harris, K. Tarverdi, P. Bishop, B. Thiebaut, P. W. Reip and S. Subbiah, *Proceedings of the 5th International Conference on Optical, Optoelectronic and Photonic Materials and Applications,* p. 44, 2012.

[299] Z. Chi, Z. Zhang, F. Wang and G. Wang, *Colloid. Surf. A: Physichem. Eng. Aspects,* vol. 340, p. 161, 2009.

[300] Z. Y. Huang, T. Barber, G. Mills and M. B. Morris, *J. Phys. Chem.,* vol. 98, p. 12746, 1994.

[301] Y. Yamamoto, N. Imai, R. Mashima, R. Konaka, M. Inoue and W. C. Dunlap, *Methods Enzymol.,* vol. 319, p. 29, 2000.

[302] S. Ghose, *Acta Crystallographica,* vol. 1, p. 1948, 1967.

[303] S. Hartner, M. Ali, C. Schulz, M. Winterer and H. Wiggers, *Nanoteconology,* vol. 20, no. 445701, p. 1, 2009.

[304] J. Zhou, S. Zhou, J. Xu and L. Zhang, *J. Appl. Phys.,* vol. 98, p. 084909, 2005.